**TECHNISCHE
UNIVERSITÄT
WIEN**

**VIENNA
UNIVERSITY OF
TECHNOLOGY**

DISSERTATION

Transonic Viscous Inviscid Interactions in Narrow Channels

ausgeführt zum Zwecke der Erlangung des akademischen Grades eines
Doktors der technischen Wissenschaften unter der Leitung von

o.Univ.-Prof. Dipl.-Ing. Dr.techn. Alfred Kluwick
E322
Institut für Strömungsmechanik und Wärmeübertragung

eingereicht an der Technischen Universität Wien
Fakultät für Maschinenwesen und Betriebswissenschaften

von

Dipl.-Ing. Georg Meyer
Matrikelnummer: 9625671
Lacknergasse 106/5, A-1180 Wien

Wien, im März 2009

Zusammenfassung

Es werden sowohl instationäre als auch stationäre transsonische Strömungsvorgänge bei großen Reynolds Zahlen in Kanälen betrachtet, die derart schlank sind, dass es zu einem Versagen der klassischen hierarchischen Grenzschicht-Theorie kommt. Folglich lassen sich die Eigenschaften der reibungsfreien Kernregion und der viskositätsbestimmten Grenzschichtsregionen an den Kanalwänden nicht mehr in aufeinander folgenden Schritten berechnen, sondern müssen vielmehr gleichzeitig bestimmt werden. Das resultierende lokale Wechselwirkungsproblem für laminare Strömungen idealer und realer Gase (BZT Fluide) wird mithilfe der Methode der angepassten asymptotischen Entwicklungen formuliert unter der Voraussetzung, dass der Kanal zudem noch so schlank ist, dass die Strömung in der Kernregion als eindimensional betrachtet werden kann. Dies führt auf ein *triple deck* Problem, bei dem die wechselwirkende Kernregion durch ein einziges *upper deck* repräsentiert wird, welches von den beiden wechselwirkenden Grenzschichten ober- und unterhalb geteilt wird. Im ersten Anwendungsfall wird der Wechselwirkungsvorgang durch einen stationären schwachen geraden Stoß in einem schlanken Kanal konstantem Querschnitts hervorgerufen. Der regularisierende Einfluss wechselwirkender Grenzschichten wird diskutiert und anhand ausgewählter Lösungen für die innere Struktur von Verdünnungsstößen, sonischen und dopplet-sonischen Stößen, welche von der rein reibungsfreien Theorie für BZT Fluide vorhergesagt werden, demonstriert. Im zweiten Anwendungsfall wird der Wechselwirkungsvorgang durch eine kleine Laval Düse hervorgerufen, die sich in einem schlanken Kanal von ansonstem konstanten Querschnitts befinden soll. Das stationäre Strömungsbild in solchen Düsen unterschiedlicher minimaler Querschnitte aber von ansonsten gleicher Gestalt wird in Hinblick auf die eindimensionale reibungsfreie Theorie von Laval Düsen diskutiert. Eine zeitabhängige numerische Simulation und eine lineare Stabilitätsuntersuchung wenden sich dem Phänomen der selbst-erhaltenden Oszillationen eines Stoßes in Gegenwart von Grenzschichtablösung zu, welche in einer nahezu "gechokten" Strömung im divergierenden Teil solcher Düsen auftreten kann. Asymptotische Methoden erweisen sich dabei als geeignete Mittel, um die wesentlichen Effekte (hier die Wechselwirkung zwischen Stoß und Grenzschicht) ausgehend von *first principles* in ein mathematisches Modell zu isolieren.

ii

Abstract

Unsteady and steady internal transonic flows at high Reynolds numbers through channels so narrow that the classical boundary layer approach fails are considered. As a consequence, the properties of the inviscid core and the viscosity dominated boundary layer regions adjacent to the channel walls can no longer be determined in subsequent steps but have to be calculated simultaneously in the framework of a local viscous inviscid interaction strategy. Under the requirement that the channel is sufficiently narrow so that the flow outside the viscous wall layers becomes one-dimensional to the leading order the resulting interaction problem for laminar flows is formulated for both perfect gases and dense gases with mixed nonlinearity (BZT fluids) by means of matched asymptotic expansions. As an outcome of the asymptotic analysis the interaction problem is consistently described by a triple deck problem. The interacting core region hereby is represented by a single upper deck which is shared by the two interacting boundary layers at the lower and upper channel walls.

In the first application to be considered the interaction process is triggered by the formation of a stationary weak normal shock in a slender channel of constant cross section. The regularizing properties of the mechanism of viscous inviscid interactions are discussed and representative solutions for the internal structure of weak rarefaction shocks, sonic and double sonic shocks and split shocks which are predicted by inviscid theory in case of BZT fluids are presented.

In the second application the interaction process is triggered by a small Laval nozzle located in a channel of otherwise constant cross section. The steady flow field through nozzles of different minimum cross sections but of otherwise similar shape is discussed highlighting the differences and similarities to classical one-dimensional Laval nozzle theory. Unsteady calculations and a linear stability analysis address the problem of self-sustained shock wave oscillations in the presence of flow separation taking place in a nearly choked flow regime in the diverging duct of a nozzle of the mentioned kind. Asymptotic methods hereby proof to be a means to isolate the essential physical effects, here the shock/boundary layer interaction, and to derive simplified model equations in a consistent manner based on first principles.

Expression of Thanks

I'd like to thank Prof. A. Kluwick, first of all, for giving me the opportunity to work with him. During my regular studies I have already attended most of his lectures and have learned to know him as an excellent teacher with a highly creative scientific mind. During many interesting talks, some of them on conferences in far away parts of the world, I also have learned to appreciate his generous and kind ways.

Then I'd like to thank Prof. Ch. Schmeiser for the opportunity to take part in the *WK Differential Equations*. I really enjoyed catching a glimpse on real mathematics and I think that I have profited very much by it.

I'm also very much indebted to Prof. Ph. Gittler who kindly has taken over the *Co-Referat* of my thesis.

Many thanks also to my colleagues at the *WK*, Franz, Sabine, Gonca and the others, and to my colleagues at the institute of *Fluid Mechanics and Heat Transfer*, Guido, Richard, Uli, Roland, Thomas (both), Markus, Christoph, Stefan (both), Bernhard (both), Matthias, Rene, Edwin, Christian, Daniel, Tanja, Kathi, Harald, Herbert Steinrück. It has been a great time and who would have guessed that philosophy would be such a great issue during lunch at the local canteen. Maybe it is in times of great physical suffering when the need of the human mind for the spiritual is at the greatest.

Also many thanks to my friends, Bernhard, Florian, Matthias, Denise, Lambert, Günther, York, Dani, Gerold. It has been important for me to get away from science from time to time, to get a new lease on life.

I have been lucky in many ways to be able to work on my PhD-thesis, but the greatest contribution hereby rests with my parents, Henni and Franz, and my sister, Vera, who not only financed and/or supported my regular studies, but who also let me approach things in a round-about way, sometimes with many detours, now cumulating in this thesis.

OK, I'd better stop here, before I start to thank the world at large ... enough, or too much! In fact, it's a good time to stop writing, outside, spring is about to come ...

Contents

Chapter 1

Introduction

Steady as well as unsteady viscous inviscid interactions taking place in internal, transonic, single phase and two-dimensional flows at high Reynolds numbers through narrow channels shall be considered. Near the channel inlet viscous effects at high Reynolds numbers are limited to thin laminar boundary layers which develop in the vicinity of the channel walls and Prandtl's classical boundary layer theory can be applied with good accuracy, in general, [32]. However, rapid changes in the streamwise flow field, such as the formation of a weak normal shock or the presence of a weak local reduction of the cross section of the channel or both eventually in connection with boundary-layer separation, cf. figure 1.1, are found to lead to a local breakdown of the classical boundary layer approach, cf. [80] or [37] amongst others. As a direct consequence, the properties of the inviscid core and the viscosity dominated boundary layer regions can no longer be determined in subsequent steps but have to be calculated simultaneously in the small interaction regions depicted by the green regions in figure 1.1. To be specific, the channel shall be sufficiently slender so that the originally two interaction regions for the boundary layer in the upper and lower half of the channel condense to one single interaction region as is sketched in figure 1.1. Under the additional requirement that the channel is sufficiently narrow so that the flow outside the viscous wall layers becomes one-dimensional to the leading order the resulting interaction problem shall be formulated by means of matched
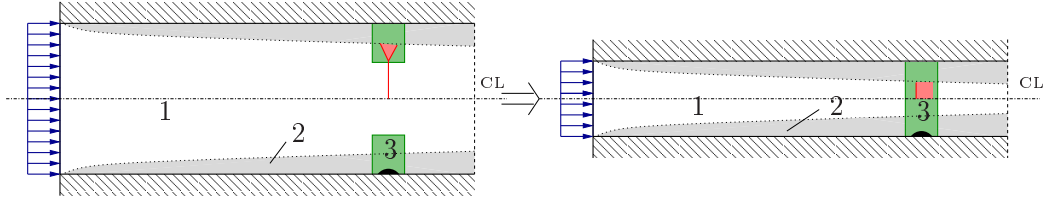
Figure 1.1: Sketch of the flow configuration under consideration. The viscous inviscid interaction is triggered by a shock (red line, upper part) or by a reduction of the flow cross section (lower part). The channel is so slender that the two interaction regions for the boundary layer in the upper and lower half of the channel (left hand side) collapse to one single interaction region (right hand side). Region (1): inviscid core region flow; region (2): viscosity dominated boundary layers; region (3): viscous inviscid interaction region.

asymptotic expansions exploiting the largeness of the Reynolds number. The requirement of one-dimensionality of the flow through the interacting channel core region simplifies the numerical treatment of the transonic flow regime in the interaction region significantly while preserving the characteristics associated with transonic flow at the same time, cf. [41].

The current work, which has been funded by the *Austrian Science Fund* in the framework of the *WK Differential Equations*, originates from previous work done in this context by Kluwick, [39], Kluwick & Gittler, [43], and Kluwick & Braun & Gittler, [41], who studied the steady transonic interacting flow of a perfect gas in a slender channel. The extension to their work covers, in particular, unsteady effects which are to be included properly in the formulation of the interaction problem. In addition, real gas effects are introduced with the focus on dense gases, i.e. BZT fluids. The derivation of the appropriate distinguished limit capable to describe the interaction problem is generalized thereby loosening some restrictions on the geometry scalings of the flow configuration.

The treatise pursues the following aims.

- The formulation of the problem is presented in chapter 2.

- The regularizing effect of viscous inviscid interaction on the various shock-forms which are possible, at least theoretically, in dense gases,

i.e. BZT fluids, cf. [35], such as rarefaction shocks, sonic and double sonic shocks and split shocks, shall be investigated in chapter 3. The mechanism of viscous inviscid shock regularization to be discussed is fundamentally different to the well known shock regularization by thermo-viscous effects, cf. eg. [18], [35]. BZT fluids and their properties are shortly characterized in section 1.1.

- A theoretical approach to study the transonic flow through small nozzles at high Reynolds numbers in the framework of interacting boundary layer theory shall be presented in section 4.2 highlighting the differences and similarities to classical one-dimensional Laval nozzle theory. The nozzle of small length scale shall be located in a slender channel of constant cross section, cf. lower part of figure 1.1. A literature survey reveals that no such theory exists at present which addresses the flow in general and the conversion of subsonic flow to supersonic flow in particular in flow devices of small scale for the high Reynolds number regime. Small scale, here, means channel cross sections and streamwise extend of the nozzle of about 10mm, say, so well above micro-scale.

- First steps towards a rational approach to study the phenomenon of self-sustained shock wave oscillations in the presence of flow separation taking place in the diverging duct of a nozzle of the mentioned kind shall be given in section 4.3. Such unsteady flow behavior in transonic diffusers is a feature frequently encountered in engineering practice, cf. e.g. [54]. However, the theoretical or numerical approaches to deal with the problem of self-sustained shock oscillations so far center either on models for inviscid flow and considering the shock boundary layer interaction in an ad-hoc manner at most, [7], [27], or rely on numerical simulations of the full problem introducing models, e.g., for turbulence and wall functions amongst others, [54], [93]. Asymptotic methods hereby proof to be a means to isolate the essential physical effects, here the shock/boundary layer interaction, and to derive simplified model equations in a consistent manner based on first principles.

Related works on viscous inviscid interactions in internal purely super-

sonic flows can be found in [73] and [40], works on viscous inviscid interactions
in internal purely subsonic flows in e.g. [77] amongst others. Investigations on
viscous compressible flow in slender channels at moderate Reynolds numbers
or in micro channels are to be found, e.g., in [32], [65], [28], [94], experimental
and/or numerical studies on shock boundary layer interaction in transonic
diffusers, e.g., [7], [27], [54], [55], [66], [60], [93].

1.1   Dense Gases - The Fundamental Derivative

The discussion throughout the thesis will be restricted to the single phase
gaseous thermodynamic region, so the thermodynamic state of the fluid is
not supposed to enter the thermodynamic region of liquid-vapor coexistence,
see figure 1.1. p, ρ and s denote the pressure, the density and the entropy,
respectively. Quantities evaluated at the critical point of thermodynamics
are denoted by the subscript c, tilde indicates dimensional quantities.

For most gaseous fluids the speed of sound, c, varies monotonously under
isentropic expansion, i.e. $\frac{\partial \tilde{c}}{\partial \tilde{\rho}}|_{\tilde{s}} > 0$. Still, there seems to exist -at least
theoretically- a limited class of fluids, known as dense gases or BZT (*Bethe-
Zel'dovich-Thompson*) fluids, for which the variation of the speed of sound
is non monotonous leading to various interesting consequences for the flow
behavior amongst others the possibility of rarefaction shocks, cf. e.g. [85].

An useful quantity characterizing the mentioned behavior of a fluid is the
so-called fundamental derivative

$$\Gamma := \frac{1}{\tilde{c}} \frac{\partial(\tilde{\rho}\tilde{c})}{\partial \tilde{\rho}}\bigg|_{\tilde{s}}. \tag{1.1}$$

In the following we will refer to fluids for which $\Gamma > 1$ in the flow region of
interest as regular fluids, fluids for which $\Gamma < 1$ as dense gases and fluids
for which $\Gamma < 0$ as BZT fluids, cf. also figure 1.1. Rarefaction shocks,
sonic or double sonic shocks and split shocks are only possible in the BZT
region $\Gamma < 0$, e.g. [34]. The thermodynamic region of non monotonous flow
behavior is restricted to a small region in the dense vapor phase near the
thermodynamical critical point as shown in figure 1.1.

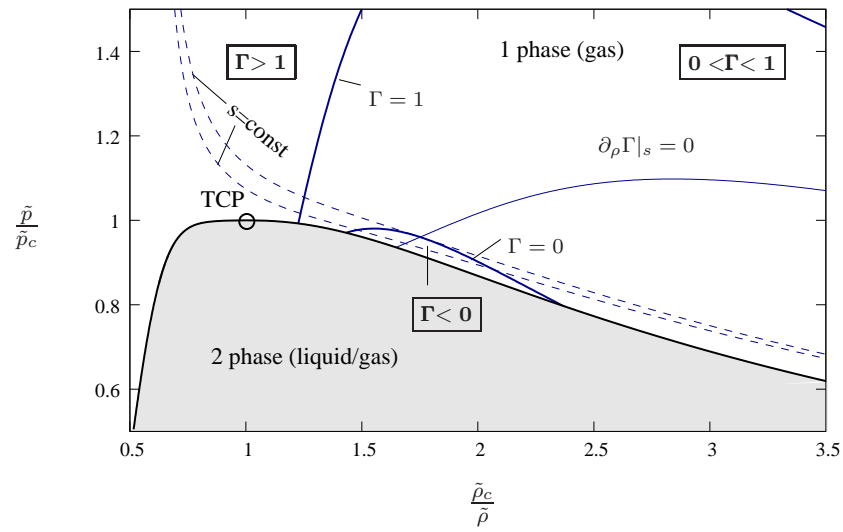Figure 1.2: Pressure vs. density diagram for a BZT fluid. Region of $\Gamma > 1$: regular, classical behavior. Region of $0 < \Gamma < 1$: dense gases region with regular behavior. Region of $\Gamma < 0$: dense gas region with non regular behavior, BZT region. The subscript c indicates thermodynamic quantities evaluated at the critical point of thermodynamics, TCP denotes the thermodynamical critical point.

Chapter 2

Model

The transonic flow of perfect/dense gases through a slender channel of height $\tilde{H}_0$ is considered, see figure 2.1. The fluid is moving from left to right and the Reynolds number is supposed to be large leading to the formation of a noninteracting viscous boundary layer at the channel walls, region 2 in figure 2.1. At the position $\tilde{L}_0$ rapid changes in the flow field shall trigger a process of viscous inviscid interaction in a region of small lateral extent, region 3. These rapid changes can be caused by the formation of a weak shock in the inviscid core region flow eventually leading to flow separation in the boundary layer, as is shown in the upper half of figure 2.1, or by a surface mounted obstacle of short length scale, potentially in combination with a shock shown in the lower half of figure 2.1. The channel shall be sufficiently slender so that the originally two interaction regions for the boundary layer in the upper and lower half of the channel condense to one single interaction region as is shown in figure 2.1. Therefore, a special distinguished limit is sought after, where the actual channel height is not known a priori but is part of the interaction problem itself.

The interaction process in region 3 shall be described by means of matched asymptotic expansions. To this end the basic set of equations in non-dimensional form is provided first, then, subsequent to the introduction of the equations, the magnitude of the various dimensional groups entering the formulation of the problem will be discussed.
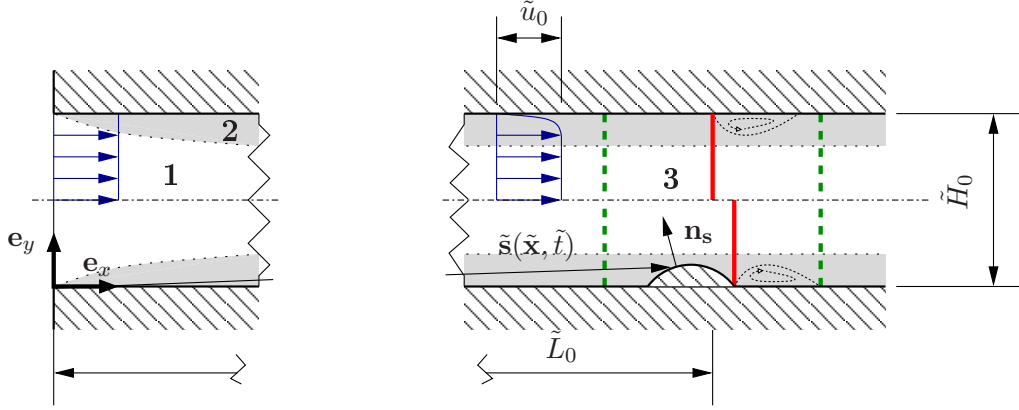
Figure 2.1: Schematic sketch of the problem setup. Region 1: inviscid core, region 2: viscous noninteracting boundary layers (L. Prandtl), region 3: viscous inviscid interaction. The red line symbolizes a shock.

Introduce the non-dimensional quantities, tilde denotes dimensional quantities,

$$
\begin{aligned}
\tilde{\mathbf{x}} &= (\tilde{x}, \tilde{y}) = \tilde{L}_0\ \mathbf{x}, & \tilde{H}_0 &= \tilde{L}_0 H_0, & \tilde{\nabla} &= \tfrac{1}{\tilde{L}_0}\ \nabla, & \tilde{\mathbf{s}} &= (\tilde{x}, \tilde{s}_2) = \tilde{L}_0\ \mathbf{s}, \\
\tilde{\mathbf{u}} &= (\tilde{u}, \tilde{v}) = \tilde{u}_0\ \mathbf{u}, & \tilde{t} &= \tfrac{\tilde{L}_0}{\tilde{u}_0}\ t, & \tilde{\rho} &= \tilde{\rho}_0\ \rho, & \tilde{p} &= \tilde{\rho}_0 \tilde{u}_0^2\ p, \\
\tilde{\theta} &= \tilde{\theta}_0\ \theta, & \tilde{h} &= \tilde{u}_0^2\ h, & \tilde{s} &= \tilde{c}_{p,0} s, & \tilde{\mu} &= \tilde{\mu}_0\ \mu, \\
\tilde{\mu}_b &= \tilde{\mu}_0\ \mu_b, & \tilde{k} &= \tilde{k}_0\ k, & \tilde{c} &= \tilde{c}_0\ c.
\end{aligned}
$$

Here $\tilde{\mathbf{x}}$ denotes the position vector with the horizontal and vertical components $(\tilde{x}, \tilde{y})$, $\tilde{\nabla}$ the nabla operator acting on the spacial coordinates only, $\tilde{\mathbf{s}}$ the position vector describing the contour of a surface mounted hump with the horizontal and vertical coordinates $(\tilde{x}, \tilde{s}_2)$, $\tilde{\mathbf{u}}$ the velocity vector with the horizontal and vertical components $(\tilde{u}, \tilde{v})$, $\tilde{t}$ the time, $\tilde{\rho}$ the density, $\tilde{p}$ the pressure, $\tilde{\theta}$ the temperature, $\tilde{h}$ the specific enthalpy, $\tilde{s}$ the specific entropy, $\tilde{c}_p$ the specific heat capacity at constant pressure, $\tilde{\mu}$ the dynamic viscosity, $\tilde{\mu}_b$ the bulk viscosity, $\tilde{k}$ the thermal conductivity and $\tilde{c}$ the speed of sound. The subscript 0 indicates a reference state. As an adequate reference state for the problem the flow quantities evaluated in the undisturbed core region flow immediately upstreams of the interaction region at position $\tilde{L}_0$ have been chosen. Then the Navier Stokes equations for 2D compressible flows

neglecting gravitational forces can be written in the following form

$$\frac{\partial \rho}{\partial t} + \nabla \cdot (\rho\, \mathbf{u}) = 0, \tag{2.1a}$$

$$\rho \left(\frac{\partial \mathbf{u}}{\partial t} + (\mathbf{u} \cdot \nabla)\, \mathbf{u} \right) = -\nabla p + \frac{1}{Re}\, \nabla \cdot \boldsymbol{\tau}, \tag{2.1b}$$

$$\rho \frac{Dh}{Dt} - \frac{Dp}{Dt} = \frac{1}{Re}\, \boldsymbol{\tau} : \nabla \mathbf{u} - \frac{1}{PrReEc}\, \nabla \cdot \mathbf{q}, \tag{2.1c}$$

with $\rho(\mathbf{x},t)$, $p(\mathbf{x},t)$, $h(\mathbf{x},t) \in \mathbb{R}$, $\mathbf{u}(\mathbf{x},t), \mathbf{q}(\mathbf{x},t) \in \mathbb{R}^2$ and $\boldsymbol{\tau} = (\tau_{ij}) \in \mathcal{M}(2,\mathbb{R})$. $\mathbf{q}$ denotes the vector of the heat flux and $\boldsymbol{\tau}$ the viscous stress tensor. The non-dimensional parameters are the Reynolds number, $Re := \frac{\tilde{\rho}_0 \tilde{u}_0 \tilde{L}_0}{\tilde{\mu}_0}$, the Eckert number, $Ec := \frac{\tilde{u}_0^2}{\tilde{c}_{p,0} \theta_0}$, and the Prandtl number, $Pr := \frac{\tilde{k}_0}{\tilde{\mu}_0 \tilde{c}_{p,0}}$.

The centerline of the nozzle $y = \frac{H_0}{2}$ is a line of symmetry; consequently in the following the boundary conditions are specified for one wall only. The boundary conditions at the (adiabatic) wall are

$$\mathbf{u} = \frac{\partial \mathbf{s}(x,t)}{\partial t}, \quad \mathbf{q} \cdot \mathbf{n_s} = 0 \qquad @\mathbf{x} = \mathbf{s}(x,t) = (x, s_2(x,t))^T,\ x > 0, \tag{2.2}$$

with $\mathbf{n_s}(\mathbf{x},t)$ the surface normal to the walls, and at the inflow $x = 0$

$$\mathbf{u} = (1,0)^T,\ \rho = 1,\ p = p_0,\ \theta = 1,\ h = h_0 \quad @\mathbf{x} = (0, 0 < y < H_0)^T, \tag{2.3}$$

with the constraint on the geometry of the nozzle entry ensuring compatibility with the inflow conditions

$$\frac{\partial s_2}{\partial x}(x = 0, t) = 0 \qquad \forall t > 0. \tag{2.4}$$

This constraint is trivially satisfied in the channel part in figure 2.1 outside the interaction region, where $s_2 \equiv 0$. In case of unsteady flow suitable initial conditions for $t = 0$ have to be provided.

Finally equations (2.1a) to (2.1c) have to be closed by the following constitutive relations:

- Newtonian fluid

$$\boldsymbol{\tau} = \mu_b (\nabla \cdot \mathbf{u}) \, \mathbf{I} + \mu \left(\nabla \mathbf{u} + \nabla \mathbf{u}^T - \tfrac{2}{3} (\nabla \cdot \mathbf{u}) \, \mathbf{I} \right), \qquad (2.5)$$

- Fourier's law

$$\mathbf{q} = -k \, \nabla \theta, \qquad (2.6)$$

- and a caloric and a thermal EOS for single component gases

$$h = h(p, s), \quad p = p(\rho, \theta). \qquad (2.7)$$

In general the material parameters μ, μ_b and k themselves are dependent on the thermodynamic state, i.e. given by the pair (p, θ).

Alternatively, equation (2.1c) can be written in the following form

$$\rho \theta \frac{Ds}{Dt} = \frac{Ec}{Re} \, \boldsymbol{\tau} : \nabla \mathbf{u} - \frac{1}{PrRe} \, \nabla \cdot \mathbf{q} \qquad (2.8)$$

making use of Gibbs' fundamental equation, [47], [75],

$$\theta \frac{Ds}{Dt} = Ec \, \left(\frac{Dh}{Dt} - \frac{1}{\rho} \frac{Dp}{Dt} \right) \qquad (2.9)$$

relating the change of the specific thermodynamic entropy s to the dissipative agencies acting in the flow, i.e. the dissipation due to viscosity and the dissipation due to thermal conductivity in the fluid. Furthermore, it will proof useful to introduce changes of the temperature θ and pressure p in the flow field into the energy equation (2.1c) by means of the expression $\frac{Dh}{Dt} = \frac{1}{Ec} \, c_p \frac{D\theta}{Dt} + \frac{1 - \tilde{\beta}_0 \tilde{\theta}_0 \beta \theta}{\rho} \, \frac{Dp}{Dt}$, see (B.19). The energy equation in new form then reads

$$\rho c_p \frac{D\theta}{Dt} = Ec \tilde{\beta}_0 \tilde{\theta}_0 \beta \theta \frac{Dp}{Dt} + \frac{Ec}{Re} \, \boldsymbol{\tau} : \nabla \mathbf{u} + \frac{1}{PrRe} \nabla \cdot \mathbf{q}, \qquad (2.10)$$

where $\beta = \frac{\tilde{\beta}}{\beta_0}$ is the coefficient of thermal expansion, see (B.3).

To sum up, the non-dimensional groups entering the governing equations are

$$Re := \frac{\tilde{\rho}_0 \tilde{u}_0 \tilde{L}_0}{\tilde{\mu}_0}, \tag{2.11a}$$

$$M_0 := \frac{\tilde{u}_0}{\tilde{c}_0}, \tag{2.11b}$$

$$Ec := \frac{\tilde{u}_0^2}{\tilde{c}_{p,0} \tilde{\theta}_0}, \tag{2.11c}$$

$$Pr := \frac{\tilde{k}_0}{\tilde{\mu}_0 \tilde{c}_{p,0}}, \tag{2.11d}$$

$$\tilde{\beta}_0 \tilde{\theta}_0 := -\tilde{\theta}_0 \frac{1}{\tilde{\rho}_0} \frac{\partial \tilde{\rho}}{\partial \tilde{\theta}}\bigg|_{\tilde{p},0}, \tag{2.11e}$$

the Reynolds number, the Mach number, the Eckert number, the Prandtl number, and the coefficient of thermal expansion at reference state times the reference temperature, respectively.

In the following, it will be assumed that $Re \gg 1$ and $M_0 \approx 1$. The first condition contributes to the formation of at least two mathematically different regions, regions 1 & 2 in figure 2.1, a region of inviscid flow and a viscous boundary layer at the walls. The equations for this case of noninteracting flow are collected in the section 2.1 as it presents the starting point for the analysis of the viscous inviscid interaction process taking place in region 3 in figure 2.1. The mathematical description of the interacting flow regime is presented in section 2.2. Special emphasis will be given to the flow properties of perfect and dense gases and their implications on the boundary layer flow.

The second condition, assumption of transonic flow $M_0 \approx 1$, allows to study weak shocks leading to a transition from supersonic to subsonic flow conditions in the core region of the channel in the framework of an asymptotic theory and to study their interaction with the boundary layer flow at the walls. Chapter 3 will discuss the regularizing properties of the shock/boundary layer interaction.

The magnitude of the Ec number depends on the fluid under consideration. For a perfect gas with constant specific heats the relation $Ec = (\gamma - 1)M_0^2$ holds. Since the ratio of the specific heats γ is of order one

	regular fluid	dense gas
Re	$\gg 1$	$\gg 1$
M_0	≈ 1	≈ 1
Ec	$\mathcal{O}(1)$	$\ll 1$
Pr	$\mathcal{O}(1)$	$\mathcal{O}(1)$
$\tilde{\beta}_0\tilde{\theta}_0$	$\mathcal{O}(1)$	$\mathcal{O}(1)$

Table 2.1: Assumptions on the order of magnitude for various dimensionless groups.

$Ec = \mathcal{O}(M_0^2)$, see [36]. Conversely the situation of dense gases for which the following estimate $Ec = \mathcal{O}(M_0^2\delta)$ has been given by Kluwick in [36]. Since in case of dense gases the ratio δ of the specific gas constant $\tilde{R}_g$ and the specific heat at constant volume $\tilde{c}_v$ is small due to the relative large values of the specific heats in compounds of higher complexity, cf. [36] or [11] for instance, $0 < \delta = \frac{\tilde{R}_g}{\tilde{c}_v} \ll 1$, this suggests $Ec \to 0$ in the limit of $\delta \to 0$.

Interestingly enough, in both cases the Prandtl number is of order one, $Pr = \mathcal{O}(1)$. Whereas this is a well-known and validated fact for a perfect gas it is, in the case of dense gases, only founded on empirical correlations since measurements in the dense gas regime are extremely difficult, [36]. These have been supported by numerical calculations performed by Zieher in [97] who used used the method of Chung, Ajlan, Lee and Starling, [9], to calculate the corresponding transport quantities for PP11, $C_{14}F_{24}$. However, the approximations implicitly used in the method, as has been noted in [36], have to be taken with caution when it comes to the application to dense gases.

Furthermore, it will be required that $\tilde{\beta}_0\tilde{\theta}_0 = \mathcal{O}(1)$ for both cases in the thermodynamic region of interest. Consequently, the very close vicinity of the thermodynamical critical point, where β exhibits unbounded growth, has to be excluded from the discussion, see [39].

Table 2.1 summarizes the assumptions on the orders of magnitude of the various dimensionless numbers for both regular, that is perfect gas like, fluids and dense gases.

2.1 Noninteracting Flow Regime

2.1.1 Inviscid Flow in the Core Region of a Channel

It has already been pointed out that the order of magnitude of the actual channel height is not known a priori but is an outcome of the formulation of the interaction problem to be discussed in section 2.2. Therefore, nothing more can be said at present about the magnitude of the vertical coordinate y in the core region of the channel, i.e. region 1 in figure 2.1, than that it will be small, i.e. $y = \mathcal{O}(Re^{-q})$ with some $q > 0$, whereas the horizontal coordinate x in the noninteracting part of the channel flow, region 1 & 2, clearly is $\mathcal{O}(1)$. It will be assumed throughout this section that the flow in the core region is inviscid in the limit $Re \to \infty$ even for $y = \mathcal{O}(Re^{-q})$. However, this so far is only an assumption which has to be verified in the end when the value of q in the scaling of y has been established. This verification will be done in 2.2.3 where the consistency of the proposed distinguished limit for the interaction region with the assumed noninteracting oncoming core region flow will be shown.

In the limit $Re \to \infty$ with $Ec = \mathcal{O}(1)$ and $Pr = \mathcal{O}(1)$ in case of a perfect gas or $Ec \to 0$ and $Pr = \mathcal{O}(1)$ in case of dense gases, see discussion of equations (2.11) or table 2.1, the **steady** versions of the governing equations (2.1a), (2.1b), (2.8) read

$$\nabla \cdot (\rho \mathbf{u}) = 0, \ \rho \left(\mathbf{u} \cdot \nabla \right) \mathbf{u} = -\nabla p, \ \frac{Ds}{Dt} = 0. \tag{2.12}$$

Equations (2.12) are the steady Euler equations which no longer satisfy all of the boundary conditions (2.2) since the terms with the highest derivatives, that is the viscous terms and the terms of thermal conductivity, have been lost in the non dissipative limit (singularly perturbed problem). How the full set of boundary conditions can be satisfied is part of the boundary layer theory, summarized in 2.1.2, at this point - inviscid flow in the core region of the channel/nozzle - only the condition

$$\mathbf{u} \cdot \mathbf{n_s} = 0 \quad @\mathbf{x} = \mathbf{s}(x) = (x, s_2(x))^T, \ x > 0 \tag{2.13}$$

is needed, again $s_2 \equiv 0$ for the channel part under consideration. As a consequence of Croccos' theorem, [86], [90], stating that an isentropic, steady, isoenergetic and two-dimensional flow field is irrotational and vice versa,

$$\nabla \times \mathbf{u} = \mathbf{0}. \tag{2.14}$$

Finally, equation (2.10) suggests that changes in the temperature are of $\mathcal{O}(Ec)$ in the limit $Re \to \infty$

$$\Delta\theta = \theta - 1 = \mathcal{O}(Ec), \qquad Re \to \infty, \tag{2.15}$$

and consequently are small for dense gases, $Ec \to 0$, representing the fact that for fluids with large specific heats, $\delta \to 0$, isentropic changes of the thermodynamic state only lead to small changes of the temperature, [39]. Then equation (2.1c) can be written in the inviscid limit for both perfect and dense gases as

$$\frac{Dh}{Dt} = \frac{1}{\rho}\frac{Dp}{Dt} \tag{2.16}$$

taking into account $\nabla \cdot \mathbf{q} = \mathcal{O}(Ec)$ as suggested by using the relation (2.15) in equation (2.6).

The solution of the problem of inviscid flow through a channel of constant height is the trivial solution of plain parallel constant flow given in definition 2.1.1.

Definition 2.1.1. *The noninteracting flow in in the core region of the channel in figure 2.1 is a plane parallel constant flow.*

$$u \equiv 1, \ v \equiv 0, \ c \equiv 1, \ \rho \equiv 1, \ p \equiv p_0, \ \theta \equiv 1. \tag{2.17}$$

The solution for the unperturbed flow in the core region of a channel, region 1 in figure 2.1, upstream of the interaction region, region 3, is completely known at this point and one could immediately proceed to the formulation of the noninteracting boundary layers at the channel walls, region 2 in figure 2.1. Never the less, in the following part of this section the equations for a

slowly varying nozzle, $s_2' \ll 1$, shall be derived. By a slowly varying nozzle it is meant that the flow shall be considered as one-dimensional to the leading order, i.e. variations from plain parallel constant channel flow shall be small. The resulting set of equations will come in useful later on when the interaction problem in region 3 will be formulated, since the proposed distinguished limit for the representation of the former inviscid core region flow in the interaction region, i.e. the upper deck, cf. section 2.2.2, is guided by the idea of one-dimensional inviscid transonic nozzle flow, with the difference that in case of an interacting flow the effect of a varying throat area will generically be generated by a displacement effect induced by the interacting boundary layers at the walls. Therefore, most of the equations obtained will be used in slightly modified form in the course of the formulation of the interaction problem in section 2.2.2 highlighting the differences between noninteracting and interacting flow.

Moreover, in section 2.2.3 the compatibility of the proposed distinguished limits for the interaction problem with region 1 flow types other than plane channel flow will be addressed. There the flow through a slowly varying nozzle will be analyzed as it is the next obvious generalization of simple flow through a channel of constant height.

Finally, the equations for one-dimensional transonic nozzle flow will be used as an inviscid counterpart throughout the discussion of the results of shock/boundary layer interaction presented in chapter 3.

Remark 2.1.1. An alternative derivation of the equations can be found in [35] using a slightly different definition of the reference state.

One-Dimensional Inviscid Transonic Flow through a Nozzle

The configuration of a nozzle with slowly varying throat area per unit depth, $\tilde{A} = \tilde{L}_0 A$, sketched in figure 2.2, is considered. Deviations from plane parallel constant flow in a channel of height H_0, definition 2.1.1, are supposed to be small

$$u = 1 + \Delta u, \ v = \Delta v, \ c = 1 + \Delta c, \ \rho = 1 + \Delta\rho, \ p = p_0 + \Delta p \qquad (2.18)$$
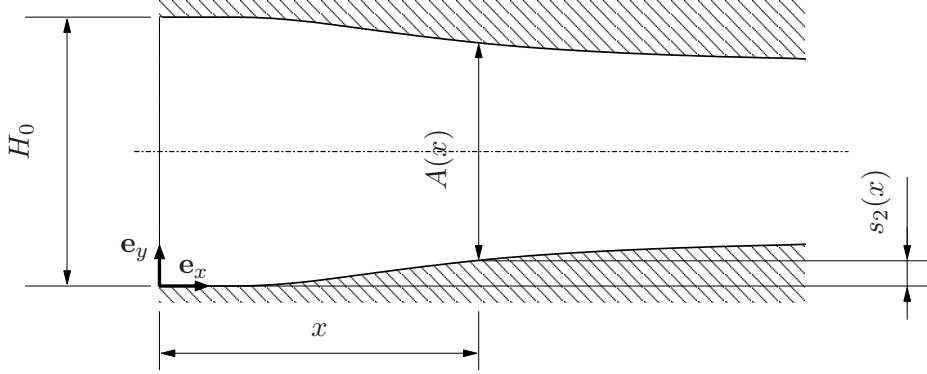
Figure 2.2: Sketch of geometry of a slowly varying nozzle.

with $|\Delta u|$, $|\Delta v|$, $|\Delta c|$, $|\Delta\rho|$, $|\Delta p| \ll 1$, and the flow shall be transonic justifying the following ansatz for the Mach number at reference state

$$M_0^2 = 1 - K\Delta K_0 \tag{2.19}$$

with $\Delta K_0 \ll 1$.

Remark 2.1.2. K is a transonic similarity parameter, [62], in anticipation of the results of the following analysis.

Inserting into the first two equations of (2.12) and equation (2.16) suggests

$$\frac{\partial}{\partial x}\left(\Delta u + \Delta\rho + \Delta\rho\Delta u\right) = \mathcal{O}(\Delta v), \tag{2.20}$$

$$\frac{\partial}{\partial x}\left(\Delta u + \Delta p\right) = \mathcal{O}(\Delta u\Delta v + \Delta u^2 + \Delta p\Delta\rho), \tag{2.21}$$

$$\frac{\partial}{\partial y}\Delta p = \mathcal{O}(\Delta v), \tag{2.22}$$

$$\frac{\partial}{\partial x}\left(\Delta h - \Delta p\right) = \mathcal{O}(\Delta u(\Delta h + \Delta p) + \Delta v(\Delta h + \Delta p)), \tag{2.23}$$

and thus, requiring the flow to become one-dimensional to the leading order, implying $\Delta v \ll \Delta u$, and additionally considering the inflow condition (2.3), leads to the following assumptions on the order of magnitudes of the flow

quantities

$$\Delta\rho \sim -\Delta u - \Delta\rho\Delta u, \qquad (2.24)$$

$$\Delta u \sim -\Delta p, \qquad (2.25)$$

$$\Delta h \sim \Delta p. \qquad (2.26)$$

Remark 2.1.3. In equations (2.20) and (2.24) the higher order term $\Delta\rho\Delta u$ has been kept for later use.

At this point the question how small Δv has to be cannot be answered. To this end equations (2.12) are rewritten as

$$\nabla \cdot \mathbf{u} + \mathbf{u} \cdot \frac{1}{\rho}\nabla\rho = 0, \qquad (2.27a)$$

$$(\mathbf{u} \cdot \nabla)\,\mathbf{u} = -\frac{c^2}{M_0^2}\frac{1}{\rho}\nabla\rho \qquad (2.27b)$$

using the relation $\nabla p = \frac{\partial p}{\partial \rho}\big|_s \nabla\rho$ with $\frac{\partial p}{\partial \rho}\big|_s = \frac{c^2}{M_0^2}$, see (B.2). Projecting (2.27b) onto streamlines leads to

$$\mathbf{u} \cdot \left((\mathbf{u} \cdot \nabla)\,\mathbf{u}\right) = (\mathbf{u} \otimes \mathbf{u}) : \nabla\mathbf{u} = -\frac{c^2}{M_0^2}\,\mathbf{u} \cdot \frac{1}{\rho}\nabla\rho, \qquad (2.28)$$

and inserting (2.27a) finally leads to the fundamental equation of gas dynamics, [62],

$$\left(\mathbf{u} \otimes \mathbf{u} - \frac{c^2}{M_0^2}\,\mathbf{I}\right) : \nabla\mathbf{u} = 0, \qquad (2.29)$$

where $\mathbf{u} \cdot (\mathbf{u} \cdot \nabla)\,\mathbf{u} = u_i u_j \partial_j u_i = (\mathbf{u} \otimes \mathbf{u}) : \nabla\mathbf{u}$ has been used. Again, inserting the ansatz for the flow quantities (2.18) into (2.29) suggests

$$\left(u^2 - \frac{1}{M_0^2}c^2\right)\frac{\partial}{\partial x}\Delta u = \frac{\partial}{\partial y}\Delta v + \mathcal{O}(\Delta v\Delta u + \Delta v\Delta K + \Delta v^2). \qquad (2.30)$$

Provided ansatz (2.18) leads to a significant degeneration indeed the term on the left hand side of (2.30) which is of $\mathcal{O}\left((u^2 - \frac{1}{M_0^2}c^2)\,\Delta u\right)$ has to balance

with the right hand side which is of $\mathcal{O}\left(\Delta v\right)$, thus providing the estimate

$$\left(u^2 - \tfrac{1}{M_0^2}c^2\right)\Delta u \sim \Delta v \tag{2.31}$$

on Δv. However, the magnitude of Δv also depends on the variation of the throat area of the nozzle $A(x)$ imposed by the boundary condition (2.13), so (2.31) is in fact a condition how weakly the throat area of the nozzle is allowed to be varied along the center line of the nozzle to justify the assumption of an one-dimensional flow in the core region of the nozzle. The magnitude of $\left(u^2 - \tfrac{1}{M_0^2}c^2\right)$, on the other hand, depends on how close the inflow conditions are to sonic flow conditions and on the thermodynamic properties of the fluid. Finally, this will lead to an estimate for ΔK_0 in equation (2.19) which has not been addressed so far in the discussion.

Magnitude of variation of throat area ΔA. As the deviations of the flow quantities are supposed to be small the variation of the throat area shall be small as well, i.e.

$$A(x) = \tfrac{\tilde{A}}{\tilde{L}_0} = H_0 + \Delta A(x) \tag{2.32}$$

with $|\Delta A| \ll 1$. Inserting (2.18) and (2.32) into the boundary conditions (2.13) gives

$$\Delta v = -(1 + \Delta u)\frac{\mathrm{d}}{\mathrm{d}x}\frac{\Delta A}{2} = -\frac{\mathrm{d}}{\mathrm{d}x}\frac{\Delta A}{2} + \mathcal{O}(\Delta A \Delta u) \quad @\mathbf{x} = \mathbf{s}(x) = (x, s_2(x))^T \tag{2.33}$$

using the relation for the non-normalized surface normal $\mathbf{n_s} = \left(\frac{d}{dx}\frac{\Delta A}{2},\ 1\right)^T$ [1].

Magnitude of $u^2 - \tfrac{1}{M_0^2}c^2$ - Condition for transonic flow of perfect and dense gases. In order to give an order of magnitude estimate for the expression $u^2 - \tfrac{1}{M_0^2}c^2$ it is necessary to consider the isentropic variation of the speed of sound c under the variation of the thermodynamic state, i.e. under

---

[1]$\mathbf{s}(x) = (x, s_2(x))^T = (x, \frac{H_0 - A(x)}{2})^T \rightsquigarrow \mathbf{t_s}(x) = (1, -\frac{A'(x)}{2})^T,\ \mathbf{n_s}(x) = (\frac{A'(x)}{2}, 1)^T$

the variation of the density ρ. To this end the following expression for c^2 is used as a starting point

$$c^2 = M_0^2 \frac{\partial p}{\partial \rho}\Big|_s = M_0^2 \rho \frac{\partial h}{\partial \rho}\Big|_s. \tag{2.34}$$

The last step in equation (2.34) is a direct consequence of Gibbs' fundamental equation (2.9). Now the expression $\frac{\partial h}{\partial \rho}\Big|_s$ is Taylor expanded in terms of $\Delta\rho$

$$\begin{aligned}
\frac{\partial h}{\partial \rho}(1 + \Delta\rho, s)\Big|_s =& \frac{\partial h}{\partial \rho}\Big|_{s,0} + \frac{\partial^2 h}{\partial \rho^2}\Big|_{s,0} \Delta\rho + \frac{1}{2}\frac{\partial^3 h}{\partial \rho^3}\Big|_{s,0} \Delta\rho^2 + \\
&+ \frac{1}{6}\frac{\partial^4 h}{\partial \rho^4}\Big|_{s,0} \Delta\rho^3 + \mathcal{O}\left(\Delta\rho^4\right),
\end{aligned} \tag{2.35}$$

where the subscript 0 has the meaning as before, i.e. evaluated at reference state.

The partial derivatives of the enthalpy h have to satisfy the following relations

$$\frac{\partial h}{\partial \rho}\Big|_{s,0} = \frac{1}{M_0^2}, \tag{2.36a}$$

$$\frac{\partial^2 h}{\partial \rho^2}\Big|_{s,0} = \frac{1}{M_0^2}\left(2\Gamma_0 - 3\right), \tag{2.36b}$$

$$\frac{\partial^3 h}{\partial \rho^3}\Big|_{s,0} = \frac{1}{M_0^2}\left(4\Gamma_0^2 - 14\Gamma_0 + 2\Lambda_0 + 12\right), \tag{2.36c}$$

$$\frac{\partial^4 h}{\partial \rho^4}\Big|_{s,0} = \frac{1}{M_0^2}\left(8\Gamma_0^3 - 48\Gamma_0^2 + 12\Gamma_0\Lambda_0 + 94\Gamma_0 - 24\Lambda_0 + 2N_0 - 60\right), \tag{2.36d}$$

with Λ and N being defined as

$$\Lambda := \frac{\partial \Gamma}{\partial \rho}\Big|_s, \tag{2.37a}$$

$$N := \frac{\partial^2 \Gamma}{\partial \rho^2}\Big|_s. \tag{2.37b}$$

A detailed derivation of the expressions (2.36) can be found in B.2.

With the relations (2.35) and (2.36) the expression (2.34) for the speed of

sound can be written as

$$
\begin{aligned}
c(1 + \Delta\rho, s_0)^2 = M_0^2 \left. (1 + \Delta\rho) \frac{\partial h}{\partial \rho}(1 + \Delta\rho, s) \right|_{s,0} = \\
= 1 + 2 \left(\Gamma_0 - 1\right) \Delta\rho + \left(2\Gamma_0^2 - 5\Gamma_0 + \Lambda_0 + 3\right) \Delta\rho^2 + \\
+ \frac{1}{3} \left(4\Gamma_0^3 - 18\Gamma_0^2 + 6\Gamma_0\Lambda_0 + 26\Gamma_0 - 6\Lambda_0 + N_0 - 4\right) \Delta\rho^3 + \mathcal{O}(\Delta\rho^4).
\end{aligned}
\tag{2.38}
$$

Collecting the previous results, the following expansion for $u^2 - \frac{1}{M_0^2}c^2$ is obtained

$$
\begin{aligned}
u^2 - \frac{1}{M_0^2}c^2 = -K\Delta K_0 - 2\Gamma_0\Delta\rho - \left(2\Gamma_0^2 - 5\Gamma_0 + \Lambda_0\right) \Delta\rho^2 - \\
- \frac{1}{3} \left(4\Gamma_0^3 - 18\Gamma_0^2 + 6\Gamma_0\Lambda_0 + 26\Gamma_0 - 6\Lambda_0 + N_0\right) \Delta\rho^3 + \\
+ 2 \left(\Delta u + \Delta\rho\right) + \Delta u^2 - 3\Delta\rho^2 + 4\Delta\rho^3 + \\
+ \mathcal{O}(\Delta\rho^4 + \Delta\rho\Delta K_0),
\end{aligned}
\tag{2.39}
$$

where

$$
u^2 = (1 + \Delta u)^2 = 1 + 2\Delta u + \Delta u^2,
\tag{2.40}
$$

$$
\frac{1}{M_0^2} = \frac{1}{1 - K\Delta K_0} = 1 + K\Delta K_0 + \mathcal{O}(\Delta K_0^2)
\tag{2.41}
$$

has been used. Equation (2.39) can be reduced even further using the subsequent relations

$$
\Delta\rho = -\Delta u - \Delta\rho\Delta u + \mathcal{O}(\Delta v),
\tag{2.42}
$$

$$
\Delta u^2 = \Delta\rho^2 + 2\Delta\rho\Delta u + \mathcal{O}(\Delta\rho\Delta v),
\tag{2.43}
$$

$$
\Delta\rho^2 = \Delta\rho \left(-\Delta u - \Delta\rho\Delta u\right) + \mathcal{O}(\Delta\rho\Delta u)
\tag{2.44}
$$

which are a direct consequence of equation (2.24). With that in mind one infers that the expression $2 \left(\Delta\rho + \Delta u\right) + \Delta u^2 - 3\Delta\rho^2 + 4\Delta\rho^3$ in (2.39) results

in terms of higher order as shown by the subsequent calculations

$$2\left(\Delta\rho + \Delta u\right) + \Delta u^2 - 3\Delta\rho^2 + 4\Delta\rho^3 = |\text{eq. } (2.43)| =$$
$$2\left(\Delta\rho + \Delta u\right) - 2\Delta\rho^2 + 2\Delta\rho^2\Delta u + 4\Delta\rho^3 + \mathcal{O}(\Delta\rho\Delta v) = |\text{eq. } (2.44)| =$$
$$2\left(\Delta\rho + \Delta u + \Delta\rho\Delta u\right) + 4\left(\Delta\rho^2\Delta u + \Delta\rho^3\right) + \mathcal{O}(\Delta\rho\Delta v) = |\text{eq. } (2.42)| =$$
$$4\Delta\rho\left(\Delta\rho\Delta u + \Delta\rho^2\right) + \mathcal{O}(\Delta v) = |\text{eq. } (2.44)| =$$
$$- 4\Delta u\Delta\rho^3 + \mathcal{O}(\Delta v) = \mathcal{O}(\Delta u\Delta\rho^3 + \Delta v),$$

so that equation (2.39) finally can be simplified to

$$u^2 - \frac{1}{M_0^2}c^2 = -K\Delta K_0 - 2\Gamma_0\Delta\rho - \left(2\Gamma_0^2 - 5\Gamma_0 + \Lambda_0\right)\Delta\rho^2 -$$
$$- \frac{1}{3}\left(4\Gamma_0^3 - 18\Gamma_0^2 + 6\Gamma_0\Lambda_0 + 26\Gamma_0 - 6\Lambda_0 + N_0\right)\Delta\rho^3 + \qquad (2.45)$$
$$+ \mathcal{O}(\Delta\rho^4 + \Delta\rho^3\Delta u + \Delta v + \Delta\rho\Delta K_0).$$

The first conclusion that can be drawn out of (2.45) is

$$\Delta K_0 = \mathcal{O}(\Gamma_0\Delta\rho). \qquad (2.46)$$

Referring to figure 2.1.1 three different cases concerning the orders of magnitude for the variation of Γ_0, Λ_0 and N_0 under the variation of the reference state in the limit $M_0 \rightarrow 1$ have to be distinguished.

$$\text{case 1 (n=2):} \quad \Gamma_0 = \mathcal{O}(1), \qquad \Lambda_0 = \mathcal{O}(1), \qquad N_0 = \mathcal{O}(1), \quad (2.47\text{a})$$
$$\text{case 2 (n=3):} \quad \Gamma_0 = \mathcal{O}(\Delta\rho), \qquad \Lambda_0 = \mathcal{O}(1), \qquad N_0 = \mathcal{O}(1), \quad (2.47\text{b})$$
$$\text{case 3 (n=4):} \quad \Gamma_0 = \mathcal{O}(\Delta\rho^2), \quad \Lambda_0 = \mathcal{O}(\Delta\rho), \quad N_0 = \mathcal{O}(1), \quad (2.47\text{c})$$

which finally gives

$$\text{case 1 (n=2):} \quad \Delta K_0 = \mathcal{O}(\Delta\rho), \qquad\qquad (2.48\text{a})$$
$$\text{case 2 (n=3):} \quad \Delta K_0 = \mathcal{O}(\Delta\rho^2), \qquad\qquad (2.48\text{b})$$
$$\text{case 3 (n=4):} \quad \Delta K_0 = \mathcal{O}(\Delta\rho^3), \qquad\qquad (2.48\text{c})$$
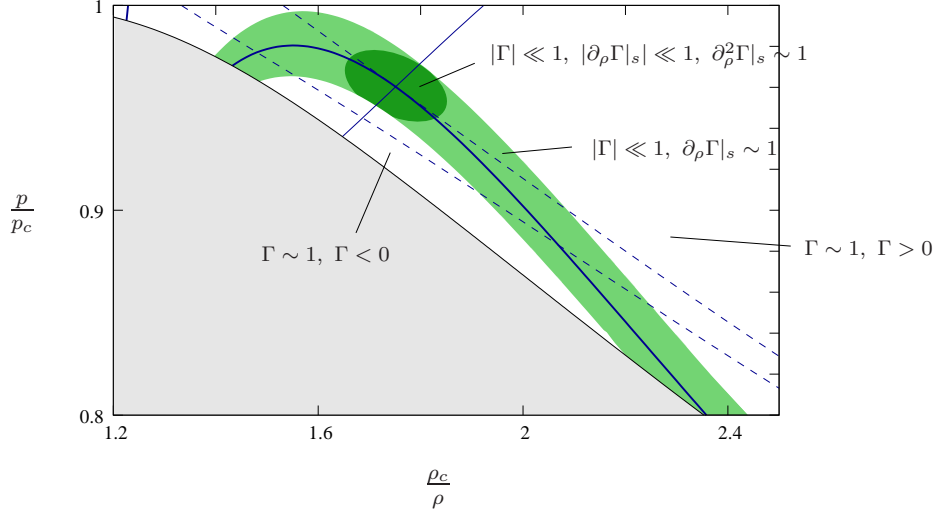
Figure 2.3: Asymptotic regions in the pressure vs. density diagram based on the magnitude of the fundamental derivative Γ and its derivatives for a BZT fluid. The subscript c indicates thermodynamic quantities evaluated at the critical point of thermodynamics, TCP denotes the thermodynamical critical point. See also figure 1.1 for a larger part of the p vs. ρ diagram.

or in short form

$$\Delta K_0 = \mathcal{O}(\Delta \rho^{n-1}). \tag{2.49}$$

Magnitude of Δv. The magnitude of Δv, as mentioned before, has to be such that the left-hand side and the right-hand side in equation (2.30) balance. Using equations (2.24) and (2.49) this implies

$$\Delta v = \mathcal{O}(\Delta \rho^n) = \mathcal{O}(\Delta u^n). \tag{2.50}$$

Formal asymptotic expansions. The order of magnitude relations derived so far suggest the following ansatz for formal asymptotic representations of the various quantities

$$u = 1 \quad +\epsilon_1 u_i^{(1)}(x) + \cdots + \epsilon_1^{n-1} u_i^{(n-1)}(x) + \epsilon_1^n u_i^{(n)}(x,y) \quad +\mathcal{O}(\epsilon_1^{n+1}), \tag{2.51}$$

$$v = \qquad\qquad\qquad\qquad\qquad\qquad\qquad\quad \epsilon_1^n v_i^{(1)}(x,y) \quad +\mathcal{O}(\epsilon_1^{n+1}), \tag{2.52}$$

$$c = 1 \quad +\epsilon_1 c_i^{(1)}(x) + \cdots + \epsilon_1^{n-1} c_i^{(n-1)}(x) + \epsilon_1^n c_i^{(n)}(x,y) \quad +\mathcal{O}(\epsilon_1^{n+1}), \tag{2.53}$$

$$\rho = 1 \quad +\epsilon_1 \rho_i^{(1)}(x) + \cdots + \epsilon_1^{n-1}\rho_i^{(n-1)}(x) + \epsilon_1^n \rho_i^{(n)}(x,y) \quad +\mathcal{O}(\epsilon_1^{n+1}), \quad (2.54)$$

$$p = p_0 \quad +\epsilon_1 p_i^{(1)}(x) + \cdots + \epsilon_1^{n-1}p_i^{(n-1)}(x) + \epsilon_1^n p_i^{(n)}(x,y) \quad +\mathcal{O}(\epsilon_1^{n+1}), \quad (2.55)$$

$$h = h_0 \quad +\epsilon_1 h_i^{(1)}(x) + \cdots + \epsilon_1^{n-1}h_i^{(n-1)}(x) + \epsilon_1^n h_i^{(n)}(x,y) \quad +\mathcal{O}(\epsilon_1^{n+1}), \quad (2.56)$$

$$A = H_0 \quad\qquad\qquad\qquad\qquad\qquad\qquad +\epsilon_1^n A_i^{(1)}(x) \quad +\mathcal{O}(\epsilon_1^{n+1}), \quad (2.57)$$

and for the condition of transonic flow, see (2.19),

$$M_0^2 = 1 + \epsilon_1^{n-1}K, \qquad (2.58)$$

introducing a small perturbation parameter $0 < \epsilon_1 \ll 1$ as a measure for the expected density changes in the flow. The index i in the expansions shall emphasize that these are expansions for the solution of the (i)nviscid Euler equations.

As has been defined by (2.47) $n \in 2, 3, 4$ depending on the chosen fluid and the chosen reference state

$$\text{case 1 (n=2):} \quad \Gamma_0 = \bar{\Gamma}, \qquad \Lambda_0 = \bar{\Lambda}, \qquad N_0 = \bar{N}, \qquad (2.59a)$$

$$\text{case 2 (n=3):} \quad \Gamma_0 = \epsilon_1\bar{\Gamma}, \qquad \Lambda_0 = \bar{\Lambda}, \qquad N_0 = \bar{N}, \qquad (2.59b)$$

$$\text{case 3 (n=4):} \quad \Gamma_0 = \epsilon_1^2\bar{\Gamma}, \qquad \Lambda_0 = \epsilon_1\bar{\Lambda}, \qquad N_0 = \bar{N}. \qquad (2.59c)$$

Remark 2.1.4. The dependence of the individual coefficients in the asymptotic expansions on the arguments (x, y) is a result of the following analysis.

Inserting the expansions (2.57) to (2.57) into the continuity equation and the momentum equation in x-direction of the Euler equations (2.12) and into (2.16) gives to the leading order

$$\frac{\partial}{\partial x}\left(u_i^{(1)}(x) + \rho_i^{(1)}(x)\right) = 0, \qquad (2.60)$$

$$\frac{\partial}{\partial x}\left(u_i^{(1)}(x) + p_i^{(1)}(x)\right) = 0, \qquad (2.61)$$

$$\frac{\partial}{\partial x}\left(h_i^{(1)}(x) - p_i^{(1)}(x)\right) = 0, \qquad (2.62)$$

whereas the momentum equation in y-direction results in

$$\frac{\partial}{\partial y} p_i^{(k)} = 0 \qquad k = 1, \ldots, n-1, \tag{2.63}$$

showing that the flow field is one-dimensional for the first $n-1$ orders. Taking into account the inflow conditions (2.3), these equations can be integrated with respect to x leading to

$$u_i^{(1)}(x) = -\rho_i^{(1)}(x) = -p_i^{(1)}(x) = -h_i^{(1)}(x). \tag{2.64}$$

The condition of an irrotational flow field (2.14) gives

$$\frac{\partial}{\partial y} u_i^{(k)} = 0 \qquad\qquad\qquad k = 1, \ldots, n-1, \tag{2.65}$$

$$\frac{\partial}{\partial y} u_i^{(k)} - \frac{\partial}{\partial x} v_i^{(k-n+1)} = 0 \qquad k \geq n. \tag{2.66}$$

And, finally inserting into the fundamental equation of gas dynamics (2.30) taking into account (2.45) and (2.64) yields

$$-J'_{[n]} \left(p_i^{(1)}(x); K, \bar{\Gamma}, \bar{\Lambda}, \bar{N} \right) \frac{\partial p_i^{(1)}(x)}{\partial x} = \frac{\partial v_i^{(1)}(x,y)}{\partial y}. \tag{2.67}$$

with $J'_{[n]}(p) = \frac{\mathrm{d}J_{[n]}(p)}{\mathrm{d}p}$. $J_{[n]}$ is a polynomial of order n in $p_i^{(1)}$, see the following definition 2.1.2, and has the physical meaning of a mass flux density for which a heuristic argument will be given at the end of this section, see remark 2.1.6.

Definition 2.1.2. $J_{[n]}(p\ ;K, \Gamma, \Lambda, N)$ *is the leading order term of the pertur-bation of the mass flux density for an one-dimensional, isentropic, inviscid and transonic flow through a nozzle.*

$$J_{[n]}(p\ ;K, \bar{\Gamma}, \bar{\Lambda}, \bar{N}) = \begin{cases} -Kp - \bar{\Gamma}p^2 & n = 2 \\ -Kp - \bar{\Gamma}p^2 - \frac{1}{3}\bar{\Lambda}p^3 & n = 3 \\ -Kp - \bar{\Gamma}p^2 - \frac{1}{3}\bar{\Lambda}p^3 - \frac{1}{12}\bar{N}p^4 & n = 4. \end{cases} \tag{2.68}$$

$J_{[n]}\left(p; K, \bar{\Gamma}, \bar{\Lambda}, \bar{N}\right)$ *has the following properties.*

- *The local Mach number $M = \frac{\tilde{u}}{\tilde{c}}$ follows from*

$$M - 1 = \epsilon_1^{n-1} \frac{1}{2} \frac{\mathrm{d}J_{[n]}}{\mathrm{d}p}. \tag{2.69}$$

- *The local value of the fundamental derivative and its first derivative is given by*

$$\Gamma = -\epsilon_1^{n-2} \frac{1}{2} \frac{\mathrm{d}^2 J_{[n]}}{\mathrm{d}p^2}, \quad \Lambda = -\epsilon_1^{n-3} \frac{1}{2} \frac{\mathrm{d}^3 J_{[n]}}{\mathrm{d}p^3}. \tag{2.70}$$

In order to obtain equation (2.69) the expression $u^2 - \frac{1}{M_0^2} c^2$ is manipulated in the following way

$$\begin{aligned}
\left(u^2 - \frac{1}{M_0^2} c^2 \right) &= \left(u - \frac{1}{M_0} c \right) \left(u + \frac{1}{M_0} c \right) = \\
&= \frac{c}{M_0} (M - 1) \left(u + \frac{1}{M_0} c \right)
\end{aligned} \tag{2.71}$$

and consequently

$$M - 1 = \frac{M_0}{c} \frac{1}{u + \frac{1}{M_0} c} \left(u^2 - \frac{1}{M_0^2} c^2 \right). \tag{2.72}$$

Taking into account (2.45) for the treatment of expression $u^2 - \frac{1}{M_0^2} c^2$, insertion of the asymptotic expansion (2.51) and collecting the terms of highest order yields the sought after relation for the local Mach number M.

The importance of equation (2.67) stems from the fact that it connects the variation of the leading order terms of p, ρ, u and h along the centerline of the nozzle with the small vertical velocity component v which itself is generated by a small variation of the throat area of the nozzle $A(x)$. To this end, (2.67) is integrated with respect to y considering the fact that the term $\frac{\partial}{\partial y} v_i^{(1)}(x, y) = \frac{\partial v_i^{(1)}}{\partial y}(x)$ is a function of x only, as can be seen by the inspection

of the left-hand side of (2.67),

$$
v_i^{(1)}(x,y) = \int_0^{v_i^{(1)}} \mathrm{d}v_i^{(1)} = \int_{\frac{H_0}{2}}^y \frac{\partial v_i^{(1)}}{\partial y}(x)\mathrm{d}y = \frac{\partial v_i^{(1)}}{\partial y}(x) \int_{\frac{H_0}{2}}^y \mathrm{d}y =
$$
$$
= -\left(y - \frac{H_0}{2}\right) \frac{\mathrm{d}}{\mathrm{d}x} J_{[n]}\left(p_i^{(1)}(x); K, \bar{\Gamma}, \bar{\Lambda}, \bar{N}\right).
\tag{2.73}
$$

Here the symmetry condition $v_i^{(1)}\left(x, y = \frac{H_0}{2}\right) = 0$ has been exploited in the integration limit. Evaluating (2.73) at the wall, $y_s = \epsilon_1^n A_i^{(1)}(x) + \mathcal{O}(\epsilon_1^{n+1})$, and comparing with the boundary condition (2.33), $v_i^{(1)}(x, y_s) = -\frac{1}{2}\frac{\mathrm{d}A_i^{(1)}}{\mathrm{d}x}$, leads after some straightforward manipulations to

$$
\frac{\mathrm{d}}{\mathrm{d}x}\left(J_{[n]}\left(p_i^{(1)}(x); K, \bar{\Gamma}, \bar{\Lambda}, \bar{N}\right) + \frac{A_i^{(1)}(x)}{H_0}\right) = 0,
\tag{2.74}
$$

which can be integrated to

$$
J_{[n]}\left(p_i^{(1)}(x); K, \bar{\Gamma}, \bar{\Lambda}, \bar{N}\right) + \frac{A_i^{(1)}(x)}{H_0} = const.
\tag{2.75}
$$

Remark 2.1.5. The fundamental equation of gas dynamics (2.67) can be interpreted as a solvability condition which has to be imposed in order to avoid secular terms entering the problem at higher order in the asymptotic expansions of equations (2.12) and (2.16). This will be shown in more detail in section 2.2.2.

Remark 2.1.6. In definition 2.1.2 $J_{[n]}$ has been described as the leading order term of the perturbation of a mass flux density. First of all it reflects the interpretation of the fundamental equation of gas dynamics (2.29) as a version of the continuity equation, [62]. A heuristic explanation is given below. Consider the behavior of the mass flux density ρu close to sonic flow conditions, $u = c^*$ with c^* as the critical speed of sound, sketched in figure 2.4. Writing the first terms of a Taylor expansion for the mass flux density,

$$
\rho u = 1 + \left.\frac{\mathrm{d}\rho u}{\mathrm{d}u}\right|_0 (\Delta u) + \frac{1}{2}\left.\frac{\mathrm{d}^2\rho u}{\mathrm{d}u^2}\right|_0 (\Delta u)^2 + \mathcal{O}((\Delta u)^3),
\tag{2.76}
$$

and inserting the expressions for the slope and the curvature of the function of the mass flux close to $u = c^*$, see figure 2.4,

$$\frac{1}{\rho}\frac{\mathrm{d}\rho u}{\mathrm{d}u}\bigg|_0 = 1 - M_0^2, \quad \frac{u}{\rho}\frac{\mathrm{d}^2\rho u}{\mathrm{d}u^2}\bigg|_0 = -2\Gamma_0 + \mathcal{O}(\Gamma_0 \Delta u), \qquad (2.77)$$

leads to

$$\rho u = 1 + (1 - M_0^2)\Delta u - \Gamma_0 \Delta u^2 + \mathcal{O}(\Delta u^3). \qquad (2.78)$$

On the other hand the continuity equation for one-dimensional flow has to hold,

$$\rho u - 1 = \frac{H_0}{A} - 1 = -\frac{\Delta A}{H_0} + \mathcal{O}(\Delta A^2). \qquad (2.79)$$

Comparing the two expressions for ρu with $\Delta u \sim -\Delta p$ suggests

$$\rho u - 1 \sim -\frac{\Delta A}{H_0} \sim (M_0^2 - 1)\Delta p - \Gamma_0 \Delta p^2, \qquad (2.80)$$

which yields the first two terms of $J_{[n]}$ after having inserted the asymptotic expansions (2.51) and (2.58). To be more general, this results in the formal asymptotic representation

$$\rho u \sim 1 + \epsilon_1^n J_{[n]}\left(p_i^{(1)}(x); K, \bar{\Gamma}, \bar{\Lambda}, \bar{N}\right) \qquad (2.81)$$

of the mass flux density. From the continuity equation for one-dimensional flow then follows

$$\rho u A = const \sim \left\{1 + \epsilon_1^n J_{[n]}\left(p_i^{(1)}(x); K, \bar{\Gamma}, \bar{\Lambda}, \bar{N}\right)\right\}\left(H_0 + \epsilon_1^n A_i^{(1)}\right) =$$
$$= H_0\left\{1 + \epsilon_1^n \left(J_{[n]}\left(p_i^{(1)}(x); K, \bar{\Gamma}, \bar{\Lambda}, \bar{N}\right) + \frac{A_i^{(1)}}{H_0}\right)\right\}. \qquad (2.82)$$

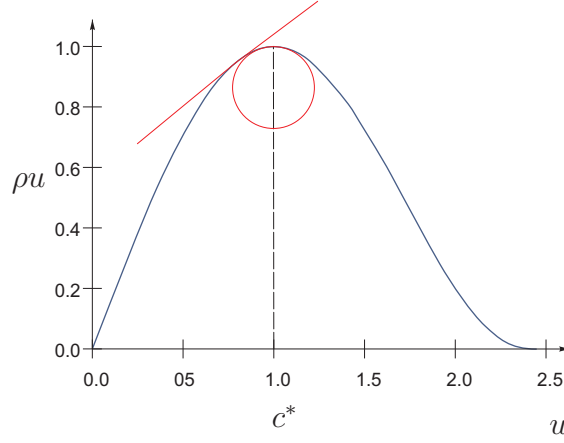Hence equation (2.75) expresses the continuity of the mass flux.

Figure 2.4: One-dimensional mass flux density vs. velocity (qualitatively).

2.1.2   Boundary Layer

The Euler equations (2.12) obtained in the inviscid limit $Re \rightarrow \infty$ cannot satisfy the no-slip condition (2.2) prescribed at the channel walls as the limiting procedure mathematically results in a degeneration of the original problem described by the Navier Stokes equations (2.1). The occurrence of this singular perturbed problem is indicated by loosing the terms of highest order derivatives, that is the dissipative terms, in the reduced problem (2.12), cf. [22], [30], [74], [91].

This shortage is overcome by introducing a second asymptotically thin region close to the walls - a boundary layer -, indicated by region 2 in figure 2.1, where the equations have to be rescaled keeping some of the dissipative terms in the resulting distinguished limit. The method of matched asymptotic expansions finally leads to an uniformly valid asymptotic representation of the solution for the two different regions for $Re \rightarrow \infty$, cf. [22], [30], [74], [91].

The classical concept of noninteracting boundary layer theory initiated by L. Prandtl in 1904 can be found in many textbooks, see e.g. [26], [33] [72], [74], [78], [91], and therefore the results of the asymptotic analysis are introduced whilst skipping most of their derivations. A few short comments on the special features resulting from the usage of fluids with equation of states of higher complexity, i.e. dense gases, and their impact on the solution of the compressible boundary layer equations will be given. Only laminar,

steady boundary layers shall be considered.

Introduce a small perturbation parameter ϵ_2 defined as

$$\epsilon_2 = Re^{-\frac{1}{2}}. \tag{2.83}$$

The asymptotic expansions of the various flow quantities in the outer, core region of a channel of constant height, region 1 in figure 2.1, to which the following length scale applies

$$x = x_1 = \mathcal{O}(1), \tag{2.84}$$

are given by

$$\begin{aligned}
u &= 1 + \mathcal{O}(\epsilon_2), & v &= \mathcal{O}(\epsilon_2), \\
p &= p_0 + \mathcal{O}(\epsilon_2), & \rho &= 1 + \mathcal{O}(\epsilon_2), \\
\theta &= 1 + \mathcal{O}(\epsilon_2), & h &= h_0 + \mathcal{O}(\epsilon_2),
\end{aligned} \tag{2.85}$$

cf. (2.17).

For the description of the boundary layer flow the length scales

$$x = X_2 = \mathcal{O}(1), \quad y = \epsilon_2 Y_2 = \mathcal{O}(\epsilon_2 = Re^{-\frac{1}{2}}). \tag{2.86}$$

are introduced. The leading order terms of the expansions for the various quantities then are given by

$$\begin{aligned}
u &= U_2^{(0)}(X_2, Y_2) + \mathcal{O}(\epsilon_2), & v &= \epsilon_2 V_2^{(0)}(X_2, Y_2) + \mathcal{O}(\epsilon_2^2), \\
p &= P_2^{(0)}(X_2) + \mathcal{O}(\epsilon_2), & \rho &= R_2^{(0)}(X_2, Y_2) + \mathcal{O}(\epsilon_2), \\
\theta &= \Theta_2^{(0)}(X_2, Y_2) + \mathcal{O}(\epsilon_2).
\end{aligned} \tag{2.87}$$

For the enthalpy h, using some appropriate equation of state $h = h(\theta, p)$, it is found that

$$h = H_2^{(0)}(\Theta_2^{(0)}, P_2^{(0)}) + \mathcal{O}(\epsilon_2). \tag{2.88}$$

Furthermore, it will be assumed that the expressions for the material parameters satisfy

$$\mu = \mu_2^{(0)}(\Theta_2^{(0)}, P_2^{(0)}) + \mathcal{O}(\epsilon_2), \qquad \mu_b = \mu_{b,2}^{(0)}(\Theta_2^{(0)}, P_2^{(0)}) + \mathcal{O}(\epsilon_2), \qquad (2.89)$$

$$k = k_2^{(0)}(\Theta_2^{(0)}, P_2^{(0)}) + \mathcal{O}(\epsilon_2), \qquad \beta = \beta_2^{(0)}(\Theta_2^{(0)}, P_2^{(0)}) + \mathcal{O}(\epsilon_2), \qquad (2.90)$$

$$c_p = c_{p,2}^{(0)}(\Theta_2^{(0)}, P_2^{(0)}) + \mathcal{O}(\epsilon_2). \qquad (2.91)$$

Then the compressible, steady, laminar boundary layer equations are given by

$$\frac{\partial R_2^{(0)} U_2^{(0)}}{\partial X_2} + \frac{\partial R_2^{(0)} V_2^{(0)}}{\partial Y_2} = 0, \qquad (2.92)$$

$$R_2^{(0)} \left(U_2^{(0)} \frac{\partial U_2^{(0)}}{\partial X_2} + V_2^{(0)} \frac{\partial U_2^{(0)}}{\partial Y_2} \right) = -\frac{\mathrm{d}P_2^{(0)}}{\mathrm{d}X_2} + \frac{\partial}{\partial Y_2} \left(\mu_2^{(0)} \frac{\partial U_2^{(0)}}{\partial Y_2} \right), \quad (2.93)$$

$$\frac{1}{PrEc} \frac{\partial}{\partial Y_2} \left(k_2^{(0)} \frac{\partial \Theta_2^{(0)}}{\partial Y_2} \right) =$$
$$= R_2^{(0)} \left(U_2^{(0)} \frac{\partial H_2^{(0)}}{\partial X_2} + V_2^{(0)} \frac{\partial H_2^{(0)}}{\partial Y_2} \right) - U_2^{(0)} \frac{\mathrm{d}P_2^{(0)}}{\mathrm{d}X_2} - \mu_2^{(0)} \left(\frac{\partial U_2^{(0)}}{\partial Y_2} \right)^2, \qquad (2.94)$$

or instead of (2.94)

$$R_2^{(0)} c_{p,2}^{(0)} \left(U_2^{(0)} \frac{\partial \Theta_2^{(0)}}{\partial X_2} + V_2^{(0)} \frac{\partial \Theta_2^{(0)}}{\partial Y_2} \right) = \frac{1}{Pr} \frac{\partial}{\partial Y_2} \left(k_2^{(0)} \frac{\partial \Theta_2^{(0)}}{\partial Y_2} \right) +$$
$$+ Ec \left\{ \tilde{\beta}_0 \tilde{\theta}_0 \beta^{(0)} \theta_2^{(0)} U_2^{(0)} \frac{\mathrm{d}P_2^{(0)}}{\mathrm{d}X_2} + \mu_2^{(0)} \left(\frac{\partial U_2^{(0)}}{\partial Y_2} \right)^2 \right\}. \qquad (2.95)$$

The boundary conditions for an adiabatic wall of the channel are

$$U_2^{(0)} = V_2^{(0)} = 0, \; \frac{\partial \Theta_2^{(0)}}{\partial Y_2} = 0 \qquad @\mathbf{X_2} = (X_2, Y_2 = 0)^T. \qquad (2.96)$$

Matching with the outer flow leads to

$$\lim_{Y_2 \to \infty} U_2^{(0)}(x, Y_2) = 1, \; \lim_{Y_2 \to \infty} \Theta_2^{(0)}(x, Y_2) = 1, \qquad (2.97)$$

where $x_1 = X_2 = x$, and

$$P_2^{(0)}(x) = p_0. \tag{2.98}$$

The boundary layer equations in compressible form, equations (2.92) to (2.98), are coupled. In order to complete the description relations governing the dependence of the material parameters μ, μ_b, k, β and c_p on the thermodynamic state have to be provided, see [72] and [78] for the case of perfect gases, where $Ec = \mathcal{O}(M_0^2)$. In case of dense gases, where $Ec = \mathcal{O}(M_0^2 \delta)$ and $0 < \delta \ll 1$, see discussion of equation (2.11), the compressible boundary layer equations can be simplified for plane parallel outer flow, definition 2.1.1, as has been noted by Kluwick in [36], [39].

Compressible Boundary Layer Flow of Dense Gases

As has been mentioned in the discussion of equation (2.11) the estimate $Ec = \mathcal{O}(M_0^2 \delta)$ for the Eckert number holds in case of dense gases with relatively large heat capacities, $0 < \delta \ll 1$. As a result, changes of the temperature across the boundary layer are small as suggested by equation (2.94),

$$\frac{\partial}{\partial Y_2} \left(k_2^{(0)} \frac{\partial \Theta_2^{(0)}}{\partial Y_2} \right) = \mathcal{O}(Ec). \tag{2.99}$$

Consequently, the temperature field in the boundary layer at an adiabatic wall can be approximated as

$$\Theta_2^{(0)}(x, Y_2) = 1 + \mathcal{O}(Ec), \tag{2.100}$$

considering the matching condition (2.97). Since the outer flow is a plane parallel constant channel flow (see definition 2.1.1) implying $\frac{dp_1^{(0)}}{dx} = 0$, the density in the whole boundary layer is constant to leading order as well. With that in mind the equations for compressible boundary layer flow simplify to

the boundary layer equations in incompressible form

$$\frac{\partial U_2^{(0)}}{\partial X_2} + \frac{\partial V_2^{(0)}}{\partial Y_2} = 0, \tag{2.101}$$

$$U_2^{(0)} \frac{\partial U_2^{(0)}}{\partial X_2} + V_2^{(0)} \frac{\partial U_2^{(0)}}{\partial Y_2} = \frac{\partial^2 U_2^{(0)}}{\partial Y_2^2}, \tag{2.102}$$

for which a solution in classical self-similar form

$$U_2^{(0)} = f'(\eta), \ V_2^{(0)} = \frac{1}{2\sqrt{x}} \left(\eta f'(\eta) - f(\eta) \right), \qquad \eta = \frac{Y_2}{\sqrt{x}} \tag{2.103}$$

exists. The function $f(\eta)$ has to satisfy the well-known Blasius' equation

$$f''' + \frac{1}{2} f f' = 0, \tag{2.104}$$

with the boundary conditions

$$f(0) = f'(0) = 0, \ \lim_{\eta \to \infty} f(\eta) = 1. \tag{2.105}$$

Remark 2.1.7. Numerical results for boundary layers in a dense gas regime forming on a flat plate with zero pressure gradient performed by Zieher in [97] showed a good agreement between the velocity profile predicted by the Blasius solution and the profiles calculated using the full incompressible formulation of the boundary layer equations, [97], [39].

2.2   Interacting Flow Regime

The flow in the interaction region, i.e. region 3 of the channel, cf. figure 2.1, can be consistently described by means of the *triple deck* theory formulated first by Stewartson, Messiter and Neiland, cf. [79], [57], [59]. The triple deck structure of the interaction region is sketched in figure 2.5. The oncoming boundary layer subdivides into a thin viscous *lower deck* where viscosity plays a significant role and a passive *main deck*. The role of the main deck is to transfer the displacement effect of the lower deck to the *upper deck* and to

transfer the resulting pressure response of the upper deck back to the lower deck.

According to the premises made for the sought after distinguished limit for the description of the interacting flow regime in the introductory remarks to chapter 2 the channel shall be sufficiently slender, so that the upper deck is represented by one single region interacting with the lower/main decks at the upper and lower channel walls, as is shown in figure 2.5. Furthermore, it will be imposed that the flow in the upper deck region shall be one-dimensional to the leading order at least. For a discussion of the significance of the desired limit in a broader physical context refer to the introduction.

The desired properties of the distinguished limit can only be obtained by a suitable choice of the order of magnitude of the channel height, which has been left undefined up to now. In the formulation of the oncoming noninteracting flow in the core region it therefore had to be assumed that the flow can be described by the inviscid Euler equations to the leading orders even when a properly scaled vertical coordinate has been introduced, cf. section 2.1.1. This assumption will be verified in section 2.2.3 after the properties of the interaction region have been established. It will be shown that the noninteracting flow through a channel of constant height is -not very surprisingly- a meaningful noninteracting oncoming flow regime indeed for the found distinguished limit. Furthermore, the question, whether more general flow types, i.e. one-dimensional nozzle flow, are compatible with the established distinguished limit, will be addressed there too.

2.2.1 Orders of Magnitude - Inspection Analysis

Under the assumption that the region of viscous inviscid interaction, region 3 in figure 2.1 or in figure 2.5, exhibits a triple deck structure relations for the relative orders of magnitude for the various flow quantities in the individual decks shall be derived mainly by inspecting the governing equations and balancing the terms which from a physical point of view have to be kept in the distinguished limits for $Re \to \infty$.
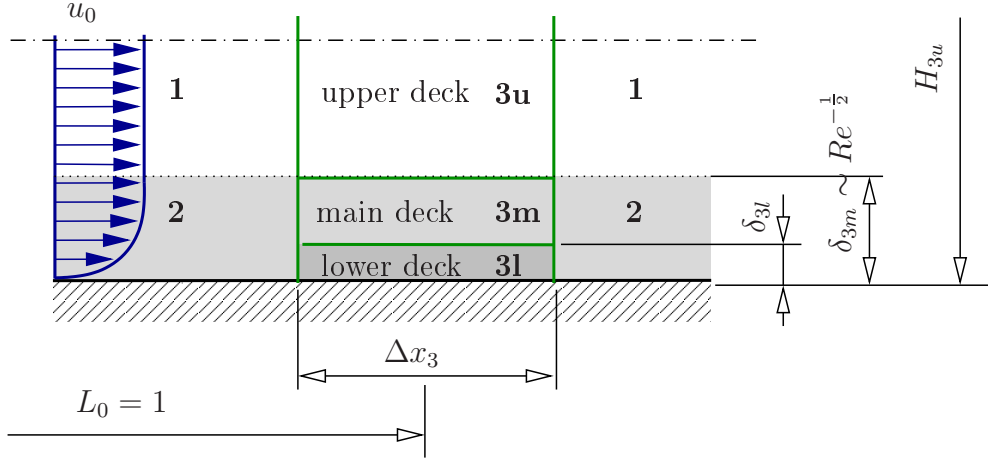
Figure 2.5: Triple deck structure of interaction region. (**3u**) *upper deck*, (**3m**) *main deck*, (**3l**) *lower deck*.

Lower Deck

- Thin lower deck

$$(u)_{3l} \sim \frac{\partial U_2^{(0)}(1,0)}{\partial Y_2} Re^{\frac{1}{2}} \delta_{3l} \sim \Delta(u)_{3l}. \qquad (2.106)$$

Here the no-slip condition $U_2^{(0)}(X_2,0) = 0$ and the boundary layer scaling $(y)_2 = Re^{-\frac{1}{2}} Y_2$ have been used.

- Balance of inertia and pressure term in x-momentum equation (2.1b)

$$\Delta(u)_{3l}^2 \sim \Delta(p)_{3l}. \qquad (2.107)$$

- Balance of inertia and viscous term in x-momentum equation (2.1b)

$$\Delta(u)_{3l} \frac{\Delta(u)_{3l}}{\Delta x_3} \sim \frac{1}{Re} \frac{\Delta(u)_{3l}}{\delta_{3l}^2}. \qquad (2.108)$$

- Pressure disturbance in thin lower deck imposed by outer flow

$$\Delta(p)_{3l} \sim \Delta(p)_{3u}. \qquad (2.109)$$

- Non-degenerate continuity equation

$$\frac{\Delta(u)_{3l}}{\Delta x_3} \sim \frac{\Delta(v)_{3l}}{\delta_{3l}}. \tag{2.110}$$

Main Deck

- Balance with the lower deck shift of the velocity profile

$$\Delta(u)_{3m} \sim \Delta(u)_{3l}. \tag{2.111}$$

- Exerted displacement on the upper deck

$$\Delta(v)_{3m} \sim \Delta(v)_{3u}. \tag{2.112}$$

- Non-degenerate continuity equation

$$\frac{\Delta(u)_{3m}}{\Delta x_3} \sim \frac{\Delta(v)_{3u}}{\delta_{3m}}. \tag{2.113}$$

- Pressure disturbance in thin main deck imposed by outer flow similar to lower deck flow

$$\Delta(p)_{3m} \sim \Delta(p)_{3u}. \tag{2.114}$$

Upper Deck

The upper deck distinguished limit is guided by the idea of one-dimensional inviscid nozzle flow presented in section 2.1.1.

- One-dimensional weakly disturbed plane parallel flow

$$\Delta(\rho)_{3u} \sim \Delta(p)_{3u} \sim \Delta(u)_{3u}. \tag{2.115}$$

- Displacement effect exerted by main deck shall lead to a flow response

at leading order, see (2.30),

$$\left((u)_{3u}^2 - \frac{1}{M_0^2}(c)_{3u}^2 \right) \frac{\Delta(u)_{3u}}{\Delta x_3} \sim \frac{\Delta(v)_{3u}}{H_{3u}} \qquad (2.116)$$

with

$$\left((u)_{3u}^2 - \frac{1}{M_0^2}(c)_{3u}^2 \right) \sim \Delta(\rho)_{3u}^{n-1}, \qquad (2.117)$$

analogous to (2.45). The parameter n governing the nonlinearity has been already defined in (2.47) for the case of inviscid nozzle flow.

- Transonic flow, see (2.46),

$$1 - M_0^2 = K\Delta K_0 \sim \Delta(\rho)_{3u}^{n-1}. \qquad (2.118)$$

- Irrotational flow

$$\left(\frac{\partial u}{\partial y} \right)_{3u} \sim \frac{\Delta(v)_{3u}}{\Delta x_3}. \qquad (2.119)$$

Remark 2.2.1. The main difference in the formulation of the small disturbance equation (2.67) in section 2.1.1 and the procedure presented here is the freedom of choice of a suitable scaling for the normal direction H_{3u} which can be used to control the degree of degeneration of equation $\nabla \times \mathbf{u} = \mathbf{0}$. By a proper choice of the order of magnitude of the channel height the flow field becomes one-dimensional to the leading order only and two-dimensionality enters at the next lower order in equation $\nabla \times \mathbf{u} = \mathbf{0}$.

- Time scaling shall preserve the slowest timescales governing the longterm behavior of the system

$$\Delta t_3 \sim \frac{\Delta x_3}{\Delta \rho^{n-1}}. \qquad (2.120)$$

Remark 2.2.2. Classical theory of compressible one-dimensional inviscid unsteady flow through a channel predicts that disturbances are

propagating along left- and right running characteristic curves, $\eta = const$ and $\zeta = const$, in the (x,t)-space with the two characteristic speeds $\lambda_\eta = \frac{\tilde{\lambda}_\eta}{\tilde{c}_0} = M_0(u)_{3u} - (c)_{3u}$ and $\lambda_\zeta = M_0(u)_{3u} + (c)_{3u}$, see [56], [49]. Obviously the faster time scale $\lambda_\zeta = \mathcal{O}(1)$, whereas the slower timescale

$$\lambda_\eta = M_0(u)_{3u} - (c)_{3u} \sim \Big(M_0(u)_{3u} - (c)_{3u} \Big)\Big(M_0(u)_{3u} + (c)_{3u} \Big) =$$
$$= M_0^2 \left((u)_{3u}^2 - \frac{1}{M_0^2}(c)_{3u}^2 \right) \sim \Delta(\rho)_{3u}^{n-1}.$$

In the last step expression (2.117) has been used. So finally the estimate (2.120) can be motivated by $\lambda_\eta \sim \frac{\Delta x_3}{\Delta t_3} \sim \Delta\rho^{n-1}$.

Calculation of the Orders of Magnitude of the Flow Quantities

Introduce a small expansion parameter $0 < \epsilon_3 \ll 0$ as a measure for the variation of the main velocity in the lower deck $\Delta(u)_{3l}$ and make the following ansatz for the orders of magnitude of the changes of the relevant flow quantities

$$\Delta(u)_{3l} \sim \epsilon_3, \Delta(v)_{3l} \sim \epsilon_3^{l_v},$$
$$\Delta(u)_{3u} \sim \epsilon_3^{n_u}, \Delta(v)_{3u} \sim \epsilon_3^{n_v}, \ \Delta(\rho)_{3u} \sim \epsilon_3^{n_\rho},$$
$$\Delta(u)_{3m} \sim \epsilon_3^{m_u}, \Delta(v)_{3m} \sim \epsilon_3^{m_v},$$
$$\Delta(p)_3 \sim \Delta(p)_{3u} \sim \Delta(p)_{3m} \sim \Delta(p)_{3l} \sim \epsilon_3^{n_p},$$
$$\Delta x_3 \sim \epsilon_3^{k_x}, \ \delta_{3m} \sim Re^{-\frac{1}{2}} \sim \epsilon_3^{k_{\delta,m}}, \ \delta_{3l} \sim \epsilon_3^{k_{\delta,l}}, H_{3u} \sim \epsilon_3^{k_H}$$

introducing the 11 unknowns k_i, l_i, m_i, $n_i \in \mathbb{Q}$. Insertion into the equations (2.106) to (2.115) yields the following 10 relations

$$\epsilon_3^{k_{\delta,l}-k_{\delta,m}} \sim \epsilon_3, \qquad \epsilon_3^2 \sim \epsilon_3^{n_p}, \qquad \epsilon_3^{2-k_x} \sim \epsilon_3^{1-2k_{\delta,l}},$$
$$\epsilon_3^{1-k_x} \sim \epsilon_3^{l_v-k_{\delta,l}}, \qquad \epsilon_3 \sim \epsilon_3^{m_u}, \qquad \epsilon_3^{m_v} \sim \epsilon_3^{n_v},$$
$$\epsilon_3^{m_u-k_x} \sim \epsilon_3^{m_v-k_{\delta,m}}, \qquad \epsilon_3^{(n-1)n_\rho+n_u-k_x} \sim \epsilon_3^{n_v-k_H}, \qquad \epsilon_3^{n_\rho} \sim \epsilon_3^{n_u},$$
$$\epsilon_3^{n_u} \sim \epsilon_3^{n_p}.$$

As has been pointed out in remark 2.2.1 the flow in the upper deck shall
be one-dimensional to the leading order and two-dimensionality shall enter
at the next higher order. However, this is not a natural condition, which
the upper deck flow has to satisfy, but one that is enforced by the a suf-
ficiently small channel height of length scale H_{3u}, as has been pointed out
in the introduction to this chapter 2.2 or also in remark 2.2.1. Therefore,
as generalization one equally well can ask for a condition that the flow field
in the upper deck is one-dimensional to the first $\mathfrak{N}_{1D}$ orders. This suggests
the following ansatz for the horizontal velocity component u, suppressing the
time dependency of the quantities in the following relations,

$$(u)_{3u} = 1 + \sum_{i=1}^{\mathfrak{N}_{1D}} \epsilon_3^{n_u+i-1} u_{3u}^{(i)}\Big((x)_3\Big) + \epsilon_3^{n_u+\mathfrak{N}_{1D}} u_{3u}^{(\mathfrak{N}_{1D}+1)}\Big((x)_3, (y)_{3u}\Big) + \cdots$$

and consequently

$$\left(\frac{\partial u}{\partial y}\right)_{3u} \sim \epsilon_3^{n_u+\mathfrak{N}_{1D}} \frac{\partial}{\partial(y)_{3u}}\, u_{3u}^{(\mathfrak{N}_{1D}+1)}\Big((x)_3, (y)_{3u}\Big) \frac{\mathrm{d}(y)_{3u}}{\mathrm{d}y}.$$

Keeping that in mind the expression for irrotational flow in the upper deck
(2.119) can be used to make the following estimate

$$\epsilon_3^{n_u+\mathfrak{N}_{1D}-k_H} \sim \epsilon_3^{n_v-k_x}.$$

Comparison of the exponents of ϵ_3 in the expressions yields the following 11
linear equations for 11 unknowns

$$
\begin{aligned}
&k_{\delta,l} - k_{\delta,m} = 1, && n_p = 2, \\
&2k_{\delta,l} - k_x = 1, && k_{\delta,l} - k_x - l_v = -1, \\
&m_u = 1, && m_v - n_v = 0, \\
&k_{\delta,m} - k_x + m_u - m_v = 0, && k_H - k_x + n_u - n_v + (n-1)n_\rho = 0, \\
&-n_u + n_\rho = 0, && n_u - n_p = 0, \\
&-k_H + k_x + n_u - n_v = -\mathfrak{N}_{1D},
\end{aligned}
$$

which have the solutions

$$k_{\delta,l} = 4 + n + \frac{\mathfrak{N}_{1D}}{2}, \quad k_{\delta,m} = 3 + n + \frac{\mathfrak{N}_{1D}}{2}, \quad k_H = 4 - n + \frac{\mathfrak{N}_{1D}}{2}, \quad k_x = 3,$$

$$l_v = 2 + n + \frac{\mathfrak{N}_{1D}}{2}, \quad m_u = 1, \quad\quad\quad\quad m_v = 1 + n + \frac{\mathfrak{N}_{1D}}{2}, \quad n_u = 2,$$

$$n_v = 1 + n + \frac{\mathfrak{N}_{1D}}{2}, \quad n_p = 2, \quad\quad\quad\quad n_\rho = 2.$$

From $\delta_{3m} \sim Re^{-\frac{1}{2}}$ it then follows for the small perturbation parameter

$$\epsilon_3 = Re^{-\frac{1}{6+2n+\mathfrak{N}_{1D}}}. \tag{2.121}$$

And finally exploiting equation (2.120) yields for the time scaling

$$\Delta t_3 \sim \epsilon_3^{5-2n}. \tag{2.122}$$

For the choice of $\mathfrak{N}_{1D}$ there are two meaningful options.

1. $\mathfrak{N}_{1D}$ is kept fixed. Then the ratio

$$\frac{(x)_3}{(y)_{3u}} = \mathcal{O}\left(\epsilon_3^{n-1-\frac{\mathfrak{N}_{1D}}{2}}\right),$$

which is a measure for the slope of streamlines in the upper deck, is dependent on the chosen nonlinearity n.

2. The ratio

$$\frac{(x)_3}{(y)_{3u}} = const$$

is kept fixed. Then the first $\mathfrak{N}_{1D} = 2(n-1)$ orders of the flow field are one-dimensional, dependent on the chosen nonlinearity n.

2.2.2 Formal Asymptotic Expansions

With the inspection analysis performed in the previous section it is possible to write down formal asymptotic expansions for the various flow quantities

Figure 2.6: Triple deck structure of interaction region. (**3u**) *upper deck*, (**3m**) *main deck*, (**3l**) *lower deck*.

in the different subregions of the interaction region characterized by different length scales in vertical direction, see figure 2.6. Inserting into the governing equations and collecting the terms of highest order yields the distinguished limits for each deck, an uniformly valid solution can be found via the matching of the different solutions of the neighboring asymptotic regions. Since for the lower deck and for the main deck this does not result in many deviations from the standard triple deck theory, see i.e. [37], [80], these equations will be introduced without much further explanations, however more details will be given for the derivation of the equations of the upper deck problem.

Inspection analysis in section 2.2.1 suggests for the spacial scaling of the x-coordinate

$$(x)_3 = 1 + \epsilon_3^3 X_3, \tag{2.123}$$

which is the same in all decks, and for the time scaling

$$t = \epsilon_3^{5-2n} T_3. \tag{2.124}$$

Lower Deck

Inspection analysis in section 2.2.1 suggests for the spacial scalings in y-direction

$$(y)_{3l} = \epsilon_3^{4+n+\frac{\mathfrak{N}_{1D}}{2}} Y_{3l}, \tag{2.125}$$

and the subsequent formal asymptotic expansions for the relevant quantities

$$(u)_{3l} = \epsilon_3 U_{3l}^{(1)}(X_3, Y_{3l}, T_3) + \mathcal{O}(\epsilon_3^2), \tag{2.126}$$

$$(v)_{3l} = \epsilon_3^{2+n+\frac{\mathfrak{N}_{1D}}{2}} V_{3l}^{(1)}(X_3, Y_{3l}, T_3) + \mathcal{O}(\epsilon_3^{3+n+\frac{\mathfrak{N}_{1D}}{2}}), \tag{2.127}$$

$$(\rho)_{3l} = R_w + \epsilon_3 R_{3l}^{(2)}(X_3, Y_{3l}, T_3) + \mathcal{O}(\epsilon_3^2), \tag{2.128}$$

$$(p)_{3l} = p_0 + \epsilon_3^2 P_{3l}^{(1)}(X_3, T_3) + \mathcal{O}(\epsilon_3^3) \tag{2.129}$$

and

$$(\mu)_{3l} = \mu_w + \mathcal{O}(\epsilon_3), \qquad (\mu_b)_{3l} = \mu_{b,w} + \mathcal{O}(\epsilon_3). \tag{2.130}$$

The subscript w has the meaning "evaluated at the wall". In case of an adiabatic wall R_w can be considered constant over the horizontal length scale of the interaction region of $\mathcal{O}(\epsilon_3^3)$.

Inserting the asymptotic expansions (2.126) to (2.129) into the governing equations yields to the leading order the following set of equations, the continuity equation

$$\frac{\partial U_{3l}^{(1)}}{\partial X_3} + \frac{\partial V_{3l}^{(1)}}{\partial Y_{3l}} = 0, \tag{2.131}$$

and the x-momentum equation

$$R_w \left(U_{3l}^{(1)} \frac{\partial U_{3l}^{(1)}}{\partial X_3} + V_{3l}^{(1)} \frac{\partial U_{3l}^{(1)}}{\partial Y_{3l}} \right) = -\frac{\partial P_{3l}^{(1)}}{\partial X_3} + \mu_w \frac{\partial^2 U_{3l}^{(1)}}{\partial Y_{3l}^2}. \tag{2.132}$$

Evaluating the no-slip condition at the wall (2.2) leads to the following boundary conditions

$$U_{3l}^{(1)} = V_{3l}^{(1)} = 0 \qquad @\mathbf{X_{3l}} = (X_3, Y_{3l} = S_{3l}(X_3, T_3))^T \qquad (2.133)$$

with the scaled hight $(s_2)_{3l} = \epsilon_3^{\frac{9+2n}{2}} S_{3l}(X_3, T_3)$ of a surface mounted obstacle, see figure 2.1. Equations (2.131) to (2.133) so far are identical to Prandtl's boundary layer equations in incompressible form derived for the noninteracting case, refer to section 2.1.2. However, new conditions arise out of the matching of the asymptotic expressions for the various flow quantities in the lower deck with those in the undisturbed boundary layer upstream of the interaction region and with those in the main deck. The matching procedure with the undisturbed boundary layer results in

$$\lim_{X_3 \to -\infty} P_{3l}^{(1)}(X_3, T_3) = 0, \qquad (2.134)$$

$$\lim_{X_3 \to -\infty} U_{3l}^{(1)}(X_3, Y_{3l}, T_3) = \frac{\partial U_2^{(0)}(1,0)}{\partial Y_2} Y_{3l}, \qquad (2.135)$$

$$\lim_{X_3 \to -\infty} V_{3l}^{(1)}(X_3, Y_{3l}, T_3) = 0. \qquad (2.136)$$

And the matching procedure with the main deck -using the results for the governing equations of the main deck obtained in the following section- results in

$$P_{3l}^{(1)}(X_3, T_3) = P_{3m}^{(1)}(X_3, T_3), \qquad (2.137)$$

$$\lim_{Y_{3l} \to \infty} \left\{ U_{3l}^{(1)}(X_3, Y_{3l}, T_3) - \frac{\partial U_2^{(0)}(1,0)}{\partial Y_2} \Big(Y_{3l} + A_{3m}(X_3, T_3) \Big) \right\} = 0. \quad (2.138)$$

A_{3m} is part of the solution of the main deck and represents the negative disturbance of the displacement thickness.

Remark 2.2.3. Subjected to the proposed time-scaling the whole lower deck problem -and in fact the whole main deck problem too- behaves quasi-steady to the leading order meaning that the flow field in the boundary layers of the

interaction region immediately adapts to transient changes in the outer flow field or to changes of the contour of the surface mounted hump.

Main Deck

Inspection analysis in section 2.2.1 suggests for the spacial scalings in y-direction

$$(y)_{3m} = \epsilon_3^{3+n+\frac{\mathfrak{N}_{1D}}{2}} Y_{3m} = Re^{-\frac{1}{2}} Y_{3m}. \tag{2.139}$$

The scaling of the vertical coordinate in the main deck is the same as for the noninteracting boundary layer upstream of the interaction region (2.86) indicating that the main deck comprises the main part of the oncoming boundary layer. The subsequent formal asymptotic expansions for the flow quantities are superimposed onto the undisturbed boundary layer profile, $U_2^{(0)}(x, Y_{3m})$, $R_2^{(0)}(x, Y_{3m})$ and $\Theta_2^{(0)}(x, Y_{3m})$, evaluated at the beginning of the interaction region $x_0 = 1$. Introducing the definitions

$$\begin{aligned} U_{20}^{(0)}(Y_{3m}) &:= U_2^{(0)}(1, Y_{3m}), \quad R_{20}^{(0)}(Y_{3m}) := R_2^{(0)}(1, Y_{3m}), \\ \theta_{20}^{(0)}(Y_{3m}) &:= \theta_2^{(0)}(1, Y_{3m}) \end{aligned} \tag{2.140}$$

the asymptotic expansions can be written as

$$(u)_{3m} = U_{20}^{(0)}(Y_{3m}) + \epsilon_3 U_{3m}^{(1)}(X_3, Y_{3m}, T_3) + \mathcal{O}(\epsilon_3^2), \tag{2.141}$$

$$(v)_{3m} = \epsilon_3^{1+n+\frac{\mathfrak{N}_{1D}}{2}} V_{3m}^{(1)}(X_3, Y_{3m}, T_3) + \mathcal{O}(\epsilon_3^{2+n+\frac{\mathfrak{N}_{1D}}{2}}), \tag{2.142}$$

$$(\rho)_{3m} = R_{20}^{(0)}(Y_{3m}) + \epsilon_3 R_{3m}^{(1)}(X_3, Y_{3m}, T_3) + \mathcal{O}(\epsilon_3^2), \tag{2.143}$$

$$(p)_{3m} = p_0 + \epsilon_3^2 P_{3m}^{(2)}(X_3, T_3) + \mathcal{O}(\epsilon_3^3), \tag{2.144}$$

$$(\theta)_{3m} = \Theta_{20}^{(0)}(Y_{3m}) + \epsilon_3 \Theta_{3m}^{(1)}(X_3, Y_3m, T_3) + \mathcal{O}(\epsilon_3^2), \tag{2.145}$$

and

$$(\mu)_{3m} = \mathcal{O}(1), \ (\mu_b)_{3m} = \mathcal{O}(1), \ (k)_{3m} = \mathcal{O}(1). \tag{2.146}$$

Before the leading order approximation for the main deck equations is written down, a closer look has to be taken at the energy equation (2.8) considering a general relation for the specific enthalpy h. The aim is to study dense gas effects where the thermodynamic relations for ideal gas are inadmissibly. $\frac{Dh}{Dt}$ in the energy equation (2.1c) can be expressed in terms of variations of the density and the entropy in the following way

$$\frac{Dh}{Dt} = \frac{\partial h}{\partial \rho}\bigg|_s \frac{D\rho}{Dt} + \frac{\partial h}{\partial s}\bigg|_\rho \frac{Ds}{Dt} = \frac{c^2}{M_0^2 \rho} \frac{D\rho}{Dt} + (1+G)\frac{\theta}{Ec} \frac{Ds}{Dt}$$

using the relation (2.34) and relation (B.20) in appendix B and introducing the Grüneisen coefficient, see i.e. [56], [47],

$$G := G_0 \bar{G} = \frac{\rho}{\theta} \frac{\partial \theta}{\partial \rho}\bigg|_s. \qquad (2.147)$$

Making use of equation (2.8) for the term $\frac{Ds}{Dt}$, the energy equation can be written after some rearranging of terms as

$$\underbrace{\frac{c^2}{M_0^2} \frac{D\rho}{Dt}}_{\mathcal{O}(\epsilon_3^{-2})} - \underbrace{\frac{Dp}{Dt}}_{\mathcal{O}(\epsilon_3^{-1})} = -G_0 \bar{G} \left(\underbrace{\frac{1}{Re} \, \boldsymbol{\tau} : \nabla \mathbf{u} - \frac{1}{PrEcRe} \, \nabla \cdot \mathbf{q}}_{\mathcal{O}(\epsilon_3)} \right) \qquad (2.148)$$

where the order of the asymptotically largest contribution of each term in the equation is indicated by the values below the brackets . Here again the argument has been used that changes of the temperature are of $\mathcal{O}(Ec)$. Therefore the term $\frac{1}{PrEcRe}\nabla \cdot \mathbf{q} = \mathcal{O}(\epsilon_3)$, even in case of dense gases, where $Ec \to 0$ for $\delta \to 0$, see table 2.1. Formally this can be deduced by inserting the asymptotic expansions for the main deck quantities into the energy equation in the form (2.8) and collecting the highest order terms resulting in

$$\left(\frac{D\theta}{Dt}\right)_{3m}^{(1)} := U_2^{(0)} \frac{\partial \Theta_{3m}^{(1)}}{\partial X_3} + V_{3m}^{(1)} \frac{d\Theta_{20}^{(0)}}{dY_{3m}} = \mathcal{O}(\epsilon_3^3 Ec), \qquad (2.149)$$

indicating that the leading order approximation of the substantial derivative of the temperature in the main deck is small for perfect gas and for dense

gas as well. The important point now is that the relative order of each term in (2.148) is depending on the magnitude of the Grüneisen coefficient G_0. Whereas G_0 clearly is an order one quantity for a perfect gas this is not so easy to see for dense gases. In short the Grüneisen coefficient can be written as

$$G_0 = \frac{\tilde{\beta}_0 \tilde{c}_0^2}{\tilde{c}_{v,0}} \frac{\tilde{K}_{s,0}}{\tilde{K}_{\theta,0}} = \tilde{\beta}_0 \tilde{\theta}_0 \frac{\tilde{c}_0^2}{\tilde{R}_g \tilde{\theta}_0} \frac{\tilde{K}_{s,0}}{\tilde{K}_{\theta,0}} \frac{\tilde{R}_g}{\tilde{c}_{v,0}}. \qquad (2.150)$$

K_θ and K_S are the isothermal and the isentropic compressibility, see appendix B.1.1. The actual calculations justifying the following reasoning can be found there as well. So taking a closer look at the quantities entering equation (2.150) reveals that $\frac{\tilde{c}_0^2}{\tilde{R}_g \tilde{\theta}_0}$, $\frac{\tilde{K}_{s,0}}{\tilde{K}_{\theta,0}}$ are order one and $\frac{\tilde{R}_g}{\tilde{c}_{v,0}} = \mathcal{O}(\delta)$ even, however $\tilde{\beta}_0 \tilde{\theta}_0$ exhibits unbounded growth in the very close vicinity of the thermodynamical critical point, which is the working regime for dense gases. The discussion in B.1.1 shows that the region of interest here, the region of negative nonlinearity, even though in the dense gas regime, still is far enough from the thermodynamical critical point, so that the argument of unbounded growth does not apply to the situation considered here and therefore $\tilde{\beta}_0 \tilde{\theta}_0 = \mathcal{O}(1)$ for dense gases also. So in conclusion, the Grüneisen coefficient $G_0 = \mathcal{O}(1)$ or even $G_0 = \mathcal{O}(\delta)$ for the cases considered in this treatise and the leading order term of the energy equation

$$\left(\frac{D\rho}{Dt}\right)_{3m}^{(1)} := U_2^{(0)} \frac{\partial R_{3m}^{(1)}}{\partial X_3} + V_{3m}^{(1)} \frac{\mathrm{d}R_2^{(0)}}{\mathrm{d}Y_{3m}} = 0,$$

takes on the usual form found in the literature for perfect gases, [37], [80], but, as has been argued, applies to the case of dense gases also, if the very vicinity of the thermodynamical critical point is excluded form the discussion.

The leading order approximation for the continuity equation and the momentum equations for dense gases can be obtained without any new arguments by straightforward insertion of the asymptotic expansions for the flow quantities. Finally collecting the results, the main deck equations are given

by

$$\left(\frac{D\rho}{Dt}\right)_{3m}^{(1)} := U_{20}^{(0)}\frac{\partial R_{3m}^{(1)}}{\partial X_3} + V_{3m}^{(1)}\frac{\mathrm{d}R_{20}^{(0)}}{\mathrm{d}Y_{3m}} = -R_{20}^{(0)}\left(\frac{\partial U_{3m}^{(1)}}{\partial X_3} + \frac{\partial V_{3m}^{(1)}}{\partial Y_{3m}}\right),\quad (2.151)$$

$$\left(\frac{Du}{Dt}\right)_{3m}^{(1)} := U_2^{(0)}\frac{\partial U_{3m}^{(1)}}{\partial X_3} + V_{3m}^{(1)}\frac{\mathrm{d}U_{20}^{(0)}}{\mathrm{d}Y_{3m}} = 0, \qquad\qquad\qquad (2.152)$$

$$\left(\frac{D\rho}{Dt}\right)_{3m}^{(1)} := U_{20}^{(0)}\frac{\partial R_{3m}^{(1)}}{\partial X_3} + V_{3m}^{(1)}\frac{\mathrm{d}R_{20}^{(0)}}{\mathrm{d}Y_{3m}} = 0, \qquad\qquad\qquad (2.153)$$

the leading order representation of the continuity equation, the x-momentum equation and the energy equation, respectively. The fact that no dissipative terms and no pressure gradient enters the governing main deck equations highlights the passive nature of the main deck, which likewise can be observed from the general solution

$$U_{3m}^{(1)} = A_{3m}(X_3, T_3)\frac{\mathrm{d}U_{20}^{(1)}(Y_{3m})}{\mathrm{d}Y_{3m}}, \qquad\qquad\qquad (2.154)$$

$$V_{3m}^{(1)} = -\frac{\partial A_{3m}(X_3, T_3)}{\partial X_3}\, U_{20}^{(0)}(Y_{3m}), \qquad\qquad\qquad (2.155)$$

$$R_{3m}^{(1)} = A_{3m}(X_3, T_3)\frac{\mathrm{d}U_{20}^{(0)}(Y_{3m})}{\mathrm{d}Y_{3m}} \qquad\qquad\qquad (2.156)$$

introducing the function $A_{3m}(X_3, T_3)$ which can be interpreted as the negative disturbance of the displacement thickness of the undisturbed boundary layer.

Matching of the main deck solutions with the lower deck solutions results in equations 2.137 and 2.138 introduced earlier. And the matching of the main deck solutions with the upper deck solutions yields

$$P_{3m}^{(1)}(X_3, T_3) = p_{3u}^{(1)}(X_3, T_3), \qquad\qquad\qquad (2.157)$$

$$\lim_{Y_{3m}\to\infty} U_{3m}^{(1)}(X_3, Y_{3m}, T_3) = \lim_{Y_{3m}\to\infty} R_{3m}^{(1)}(X_3, Y_{3m}, T_3) = 0, \qquad (2.158)$$

$$\lim_{Y_{3m}\to\infty} V_{3m}^{(1)}(X_3, Y_{3m}, T_3) = -\frac{\partial A_{3m}(X_3, T_3)}{\partial X_3} = v_{3u}^{(1)}(X_3, 0, T_3) \qquad (2.159)$$

using $\lim_{Y_{3m}\to\infty} U_{20}^{(0)}(Y_{3m}) = 1$ and $\lim_{Y_{3m}\to\infty}\frac{\mathrm{d}U_{20}^{(0)}(Y_{3m})}{\mathrm{d}Y_{3m}} = 0$. Matching with

the undisturbed boundary layer in region 2 results in

$$\lim_{X_3 \to -\infty} P_{3m}^{(1)} = 0, \quad \lim_{X_3 \to -\infty} U_{3m}^{(1)} = 0, \quad \lim_{X_3 \to -\infty} V_{3m}^{(1)} = 0. \tag{2.160}$$

Upper Deck

Inspection analysis carried out in section 2.2.1 suggests for the spacial scalings in y-direction and the scaled height of the channel H_{03}

$$(y)_{3u} = \epsilon_3^{4-n+\frac{\mathfrak{N}_{1D}}{2}} \, y_{3u}, \qquad (H_0)_{3u} = \epsilon_3^{4-n+\frac{\mathfrak{N}_{1D}}{2}} \, H_{03}, \tag{2.161}$$

and the subsequent formal asymptotic expansions for the flow quantities

$$(u)_{3u} = 1 + \epsilon_3^2 u_{3u}^{(1)}(X_3, T_3) + \mathcal{O}(\epsilon_3^3), \tag{2.162}$$

$$(v)_{3u} = \epsilon_3^{1+n+\frac{\mathfrak{N}_{1D}}{2}} \, v_{3u}^{(1)}(X_3, y_{3u}, T_3) + \mathcal{O}(\epsilon_3^{2+n+\frac{\mathfrak{N}_{1D}}{2}}), \tag{2.163}$$

$$(\rho)_{3u} = 1 + \epsilon_3^2 \rho_{3u}^{(1)}(X_3, T_3) + \mathcal{O}(\epsilon_3^3), \tag{2.164}$$

$$(p)_{3u} = p_0 + \epsilon_3^2 p_{3u}^{(1)}(X_3, T_3) + \mathcal{O}(\epsilon_3^3), \tag{2.165}$$

$$(c)_{3u} = 1 + \epsilon_3^2 c_{3u}^{(1)}(X_3, T_3) + \mathcal{O}(\epsilon_3^3), \tag{2.166}$$

$$(h)_{3u} = h_0 + \epsilon_3^2 h_{3u}^{(1)}(X_3, T_3) + \mathcal{O}(\epsilon_3^3), \tag{2.167}$$

$$(\theta)_{3u} = 1 + \epsilon_3^2 \theta_{3u}^{(1)}(X_3, T_3) + \mathcal{O}(\epsilon_3^3), \tag{2.168}$$

for the condition of transonic flow, introducing the transonic similarity parameter K,

$$\left(1 - M_0^2\right)_{3u} = K \epsilon_3^{2n-2} \tag{2.169}$$

and

$$\text{case n=2:} \qquad \Gamma_0 = \bar{\Gamma}, \qquad \Lambda_0 = \bar{\Lambda}, \qquad N_0 = \bar{N}, \qquad \text{(2.170a)}$$

$$\text{case n=3:} \qquad \Gamma_0 = \epsilon_3^2 \bar{\Gamma}, \qquad \Lambda_0 = \bar{\Lambda}, \qquad N_0 = \bar{N}, \qquad \text{(2.170b)}$$

$$\text{case n=4:} \qquad \Gamma_0 = \epsilon_3^4 \bar{\Gamma}, \qquad \Lambda_0 = \epsilon_3^2 \bar{\Lambda}, \qquad N_0 = \bar{N}. \qquad \text{(2.170c)}$$

Furthermore,

$$(\mu)_{3u} = \mathcal{O}(1), \ (\mu_b)_{3u} = \mathcal{O}(1), \ (k)_{3u} = \mathcal{O}(1). \tag{2.171}$$

In the following more time will be spent on the motivation of the governing equations for the upper deck problem than in the previous sections for the lower and main deck problem.

Continuity equation. The starting point for the formulation of the upper deck problem is the continuity equation

$$\frac{\partial \rho}{\partial t} + \nabla \cdot (\rho \mathbf{u}) = 0.$$

Insertion of the asymptotic expansions yields, using the upper deck scaling and the appropriate time scaling,

$$\epsilon_3^{-3} \frac{\partial}{\partial X_3} \left(\Delta(\rho)_{3u} + \Delta(u)_{3u} + \Delta(\rho)_{3u} \Delta(u)_{3u} \right) =$$
$$= \mathcal{O} \left(\epsilon_3^{2n-3} \frac{\partial \Delta(v)_{3u}}{\partial y_{3u}}, \epsilon_3^{2n-5} \frac{\partial \Delta(\rho)_{3u}}{\partial T_3} \right) \tag{2.172}$$

with the notation

$$\Delta(\rho)_{3u} := \sum_{k=2}^{2n-1} \epsilon_3^k \rho_{3u}^{(k-1)} + \mathcal{O}(\epsilon_3^{2n}), \tag{2.173}$$

$$\Delta(u)_{3u} := \sum_{k=2}^{2n-1} \epsilon_3^k u_{3u}^{(k-1)} + \mathcal{O}(\epsilon_3^{2n}), \tag{2.174}$$

$$\Delta(v)_{3u} := \epsilon_3^{1+n+\frac{\mathfrak{N}_{1D}}{2}} v_{3u}^{(1)} + \mathcal{O}(\epsilon_3^{2+n+\frac{\mathfrak{N}_{1D}}{2}}), \tag{2.175}$$

$$\Delta(\rho)_{3u} \Delta(u)_{3u} = \sum_{k=4}^{2n-1} \epsilon_3^k \sum_{\substack{i+j=k \\ i,j \geq 2}} \rho_{3u}^{(i-1)} u_{3u}^{(j-1)} + \mathcal{O}(\epsilon_3^{2n}). \tag{2.176}$$

Equation (2.172) then leads to

$$\Delta(\rho)_{3u} + \Delta(u)_{3u} + \Delta(\rho)_{3u} \Delta(u)_{3u} = \mathcal{O} \left(\epsilon_3^{2n} \right), \tag{2.177}$$

similar to the derivation of the essential equations for one-dimensional invis-
cid transonic flow through a nozzle presented in chapter 2.1.1, see equation
(2.20) and (2.42). Collecting the terms of same order in equation (2.177)
results in

$$\rho_{3u}^{(k-1)} + u_{3u}^{(k-1)} + \sum_{\substack{i+j=k \\ i,j \geq 2}} \rho_{3u}^{(i-1)} u_{3u}^{(j-1)} = 0 \qquad k = 2, \cdots, 2n - 1. \qquad (2.178)$$

For the integration of (2.172) with respect to X_3 the condition of matching
with plane parallel constant nozzle flow upstream, (2.17),

$$\lim_{X_3 \to -\infty} \rho_{3u}^{(k-1)} = 0, \quad \lim_{X_3 \to -\infty} u_{3u}^{(k-1)} = 0 \qquad k = 2, \cdots, 2n - 1, \qquad (2.179)$$

has been used. The integration constant entering (2.177) or (2.178) then is
found to be zero.

Momentum equation. In the following only the leading order represen-
tation of the momentum equation in x-direction

$$\frac{\partial u_{3u}^{(1)}}{\partial X_3} = -\frac{\partial p_{3u}^{(1)}}{\partial X_3} \qquad (2.180)$$

is needed, which can be integrated with respect to X_3

$$u_{3u}^{(1)} = -p_{3u}^{(1)}. \qquad (2.181)$$

The integration constant again is found to be zero by making use of the
matching conditions (2.179) and

$$\lim_{X_3 \to -\infty} p_{3u}^{(1)} = 0. \qquad (2.182)$$

The leading order term of the momentum equation in y-direction reduces to

$$\frac{\partial p_{3u}^{(1)}}{\partial y_{3u}} = 0 \qquad (2.183)$$

for all cases of $n = 2, 3, 4$ and $\mathfrak{N}_{1D} \in \mathbb{N}^+$ considered here.

Energy equation.   For the further discussion it is convenient to rewrite the energy equation in the form

$$\rho \frac{Dh}{Dt} - \frac{Dp}{Dt} = \frac{1}{Re} \, \boldsymbol{\tau} : \nabla \mathbf{u} - \frac{1}{PrReEc} \, \nabla \cdot \mathbf{q}$$

in the way already introduced for the treatment of the energy equation in the main deck, (2.148),

$$\frac{c^2}{M_0^2} \frac{D\rho}{Dt} - \frac{Dp}{Dt} = -G_0 \bar{G} \left(\frac{1}{Re} \, \boldsymbol{\tau} : \nabla \mathbf{u} - \frac{1}{PrEcRe} \, \nabla \cdot \mathbf{q} \right).$$

Making use of the momentum equation (2.1b) the substantial derivative of the pressure can be written as

$$\begin{aligned}
\frac{Dp}{Dt} &= \frac{\partial p}{\partial t} + \mathbf{u} \cdot \nabla p = \\
&= \frac{\partial p}{\partial t} + \mathbf{u} \cdot \left(-\rho \frac{\partial \mathbf{u}}{\partial t} - \rho \left(\mathbf{u} \cdot \nabla \right) \mathbf{u} - \frac{1}{Re} \nabla \cdot \boldsymbol{\tau} \right) = \\
&= \frac{\partial p}{\partial t} - \rho \mathbf{u} \cdot \frac{\partial \mathbf{u}}{\partial t} - \rho \left(\mathbf{u} \otimes \mathbf{u} \right) : \nabla \mathbf{u} - \frac{1}{Re} \mathbf{u} \cdot \left(\nabla \cdot \boldsymbol{\tau} \right),
\end{aligned}$$

where $\mathbf{u} \cdot \left(\mathbf{u} \cdot \nabla \right) \mathbf{u} = u_i u_j \partial_j u_i = \left(\mathbf{u} \otimes \mathbf{u} \right) : \nabla \mathbf{u}$ has been used in the last step. On the other hand, the substantial derivative of the density is written as

$$\frac{D\rho}{Dt} = \frac{\partial \rho}{\partial t} + \mathbf{u} \cdot \nabla \rho = \frac{\partial \rho}{\partial t} + \nabla \cdot \left(\rho \mathbf{u} \right) - \rho \nabla \cdot \mathbf{u} = \frac{\partial \rho}{\partial t} + \nabla \cdot \left(\rho \mathbf{u} \right) - \rho \mathbf{I} : \nabla \mathbf{u}.$$

Insertion into the energy equation yields the final result

$$\begin{aligned}
-\frac{c^2}{M_0^2} & \left(\frac{\partial \rho}{\partial t} + \nabla \cdot \left(\rho \mathbf{u} \right) \right) = \\
&= -\frac{\partial p}{\partial t} + \rho \mathbf{u} \cdot \frac{\partial \mathbf{u}}{\partial t} + \rho \left(\mathbf{u} \otimes \mathbf{u} - \frac{c^2}{M_0^2} \, \mathbf{I} \right) : \nabla \mathbf{u} + \\
&\quad + \frac{1}{Re} \left\{ \mathbf{u} \cdot \left(\nabla \cdot \boldsymbol{\tau} \right) + G_0 \bar{G} \left(\boldsymbol{\tau} : \nabla \mathbf{u} - \frac{1}{PrEc} \, \nabla \cdot \mathbf{q} \right) \right\}.
\end{aligned} \tag{2.184}$$

Several important conclusions can be drawn form equation (2.184).

- The expression with the factor $\frac{1}{Re}$ in front can be estimated as being of $\mathcal{O}(\epsilon_3^{4n} + \epsilon_3^{2n+2+\mathfrak{N}_{1D}})$ by inserting the asymptotic expansions for the various field quantities in the upper deck scaling. As has been pointed out in the discussion of equation (2.150) in the previous section, the Grüneisen coefficient $G_0 = \mathcal{O}(1)$ for perfect gas and $G_0 = \mathcal{O}(\delta)$ for dense gases. And once again the argument is used that in case of dense gases, where $Ec \to 0$ for $\delta \to 0$, also the changes of the temperature are of $\mathcal{O}(Ec)$ at most.

- If the expression $\left(\mathbf{u} \otimes \mathbf{u} - \frac{c^2}{M_0^2} \mathbf{I} \right) : \nabla \mathbf{u}$ would be equal to zero, then one would have obtained the fundamental equation of gas dynamics (2.29) encountered in the section dealing with the inviscid, steady flow in the core region, see 2.1.1.

- The derivation of equation (2.184) has spawned the continuity equation. This is interesting in so far, as for a consistent asymptotic formulation of the upper deck the right hand side being equal to zero has to be imposed as a solvability condition. This refers to the corresponding remark 2.1.5 made about the fundamental equation of gas dynamics. If it would be not the case, then insertion of the asymptotic representations into the energy equation finally would result in a contradiction leading to $\partial_t \rho + \nabla \cdot (\rho \mathbf{u}) \neq 0$.

By exploitation of relation (2.181) the leading order approximation of equation (2.184), i.e. the leading order approximation of the solvability condition,

$$-2\frac{\partial p_{3u}^{(1)}}{\partial T_3} - \frac{\partial}{\partial X_3} \ J_{[n]}\left(p_{3u}^{(1)}; K, \bar{\Gamma}, \bar{\Lambda}, \bar{N} \right) = \frac{\partial v_{3u}^{(1)}}{\partial y_{3u}} \qquad (2.185)$$

is obtained. The relevant steps of the analysis already have been performed in section 2.1.1 and they immediately carry over to the derivation of (2.185). Here the "delta notation", (2.173), of the continuity equation (2.177) introduced above proofs very beneficial once again. The perturbation of the mass flux density $J_{[n]}$ has been defined in definition 2.1.2.

Remark 2.2.4. As a consequence of the suitable time scaling the time dependence of the problem enters the equations here for the first time. The other equations so far have not exhibited an explicit dependency on the time.

The left hand side of equation (2.184) does not depend on y_{3u}, so it can be explicitly integrated in the same way as in (2.73) resulting in the expression (2.73) for $v_{3u}^{(1)}$. The main difference is that the velocity has to be matched to the main deck solution instead to be fitted to the gradient of the throat area of the nozzle expressed by the boundary condition of tangential flow at the wall. So applying the matching condition (2.159) gives the final result

$$-2\frac{\partial p_{3u}^{(1)}}{\partial T_3} - \frac{\partial}{\partial X_3}\; J_{[n]}\left(p_{3u}^{(1)}; K, \bar{\Gamma}, \bar{\Lambda}, \bar{N}\right) = \frac{2}{H_{03}}\frac{\partial A_{3m}}{\partial X_3}. \qquad (2.186)$$

Equation (2.186) is the final piece that closes the formulation of the whole triple deck problem, since it relates the displacement effect exerted by the main deck to an immediate response of the pressure in the upper deck at leading order. The displacement of the interacting boundary layer in itself is a result of the de- or acceleration of the lower deck flow due to changes of pressure imposed by the upper deck flow. Equation (2.186) therefore governs the viscous inviscid interaction and is consequently referred to as *interaction law*.

2.2.3   Admissible Region 1 Flow Types

As an outcome of the inspection analysis in section 2.2.1 the vertical length scale in the upper deck is of $\mathcal{O}(\epsilon_3^{4-n+\frac{\mathfrak{N}_{1D}}{2}})$. Since the upper deck region comprises the whole former core region in the interaction region, the vertical coordinate in the core region, region 1, has to be of the same order, suggesting

$$x = x_1, \qquad y = \epsilon_3^{4-n+\frac{\mathfrak{N}_{1D}}{2}} y_1. \qquad (2.187)$$

A look at the continuity equation shows that the vertical velocity v also has to scale as

$$(v)_1 = \epsilon_3^{4-n+\frac{\mathfrak{N}_{1D}}{2}} v_1, \tag{2.188}$$

whereas the other flow quantities stay order one quantities.

Insertion into the governing equations introduced at the beginning of section 2, and shown here for the basic Navier Stokes equations (2.1a) to (2.1c) equation only, leads to

$$\frac{\partial \rho_1}{\partial t} + \nabla \cdot (\rho_1 \, \mathbf{u}_1) = 0, \tag{2.189a}$$

$$\rho_1 \left(\frac{\partial \mathbf{u}_1}{\partial t} + (\mathbf{u}_1 \cdot \nabla_1) \, \mathbf{u}_1 \right) = -\nabla_1 p_1 + \mathcal{O}(\epsilon_3^{4n-2}), \tag{2.189b}$$

$$\rho \frac{D_1 h_1}{D_1 t} - \frac{D_1 p_1}{D_1 t} = \mathcal{O}(\epsilon_3^{4n-2}). \tag{2.189c}$$

Here $Re^{-1} = \epsilon_3^{6+2n+\mathfrak{N}_{1D}}$, a consequence of the definition of ϵ_3 (2.121), and the fact, that the contributions of highest order in the dissipative terms of the momentum and energy equation are resulting from $\frac{\partial^2}{\partial y^2} \sim \epsilon_3^{-8+2n-\mathfrak{N}_{1D}}$, has been used. Now, taking the limit $Re \to \infty$, implying $\epsilon_3 \to 0$, indeed gives the Euler equations, which justifies the previous assumption made for the formulation of the noninteracting core region flow in section 2.1.1. Noninteracting channel flow truly is an admissible leading order representation of the flow regime upstream of the interacting region. Therefore, the distinguished limit for the interacting flow regime proves to be consistent with all the premises made during its derivation.

In the following the question wether more general noninteracting flow types are admissible for this special interaction problem shall be addressed shortly . To this end consider the results of one-dimensional inviscid nozzle flow presented in section 2.1.1. The asymptotic representations of the flow quantities (2.51) have to be modified as follows

$$(u)_1 = 1 + \epsilon_1 u_{1i}^{(1)}(x_1) + \ldots, \tag{2.190a}$$

$$(v)_1 = \epsilon_3^{4-n+\frac{\mathfrak{N}_{1D}}{2}} \epsilon_1^n v_{1i}^{(1)}(x_1, y_1) + \ldots, \tag{2.190b}$$

$$(c)_1 = 1 + \epsilon_1 c_{1i}^{(1)}(x_1) + \ldots, \tag{2.190c}$$

$$(\rho)_1 = 1 + \epsilon_1 \rho_{1i}^{(1)}(x_1) + \ldots, \tag{2.190d}$$

$$(p)_1 = p_0 + \epsilon_1 p_{1i}^{(1)}(x_1) + \ldots, \tag{2.190e}$$

$$(h)_1 = h_0 + \epsilon_1 h_{1i}^{(1)}(x_1) + \ldots, \tag{2.190f}$$

$$(A)_1 = H_{10} + \epsilon_3^{4-n+\frac{\mathfrak{N}_{1D}}{2}} \epsilon_1^n A_{1i}^{(1)}(x_1) + \ldots, \tag{2.190g}$$

which leaves the outcome of the derivations performed in section 2.1.1 unchanged, see equation (2.74), if the symbols for the quantities used in 2.51 are substituted by the ones used in 2.190a, u_i by u_{1i}, say.

Remark 2.2.5. The nozzle geometry $(A)_1$ obviously is dependent on ϵ_3 and therefore dependent on Re.

The important point now is that $(v)_1$ has to be matched with $(v)_{3u}$. If such a matching is possible, then one-dimensional inviscid nozzle flow will be an admissible leading order representation of the flow regime upstream of the interacting region too. Matching, taking into account $y_1 = y_{3u}$ and equations (2.160) and (2.159), formally results to the leading order in

$$\epsilon_3^{4-n+\frac{\mathfrak{N}_{1D}}{2}} \epsilon_1^n v_{1i}^{(1)}(1, y_1) = \epsilon_3^{2+n+\frac{\mathfrak{N}_{1D}}{2}} \lim_{X_3 \to -\infty} v_{3u}^{(2)}(X_3, y_1, T_3). \tag{2.191}$$

Therefore the perturbation parameter ϵ_1, formerly introduced as a measure for the variation of the density in section 2.1.1, has to be dependent on Re too, which suggests

$$\epsilon_1 = \epsilon_3^{2\left(1-\frac{1}{n}\right)}. \tag{2.192}$$

Considering the relations (2.32) and (2.33) implies that not only the order of magnitude of the throat area A in the noninteracting flow regime, but also the order of magnitude of the variation of the nozzle ΔA has to depend on Re.

2.2.4 Fundamental Canonical Problem

Collecting the results derived in the previous section, the problem of viscous inviscid interaction can be fully described by the equations of the lower deck supplemented by the interaction law (2.186). Due to the passive nature of the main deck it is not explicitly needed in the formulation of the fundamental problem.

The fundamental lower deck problem in non canonical form writes

$$\frac{\partial}{\partial X_3} U_{3l}^{(1)}(X_3, Y_{3l}, T_3) + \frac{\partial}{\partial Y_{3l}} V_{3l}^{(1)}(X_3, Y_{3l}, T_3) = 0, \tag{2.193}$$

$$R_w \left(U_{3l}^{(1)} \frac{\partial U_{3l}^{(1)}}{\partial X_3} + V_{3l}^{(1)} \frac{\partial U_{3l}^{(1)}}{\partial Y_{3l}} \right) = -\frac{\partial}{\partial X_3} P_3^{(1)}(X_3, T_3) + \mu_w \frac{\partial^2 U_{3l}^{(1)}}{\partial Y_{3l}^2} \tag{2.194}$$

supplemented by the no slip condition at the wall

$$U_{3l}^{(1)} = V_{3l}^{(1)} = 0 \qquad @\mathbf{X_{3l}} = (X_3, Y_{3l} = S_{3l}(X_3, T_3))^T, \tag{2.195}$$

the conditions of matching with the undisturbed noninteracting boundary layer upstream

$$\lim_{X_3 \to -\infty} P_3^{(1)} = 0, \tag{2.196}$$

$$\lim_{X_3 \to -\infty} U_{3l}^{(1)} = \frac{\partial U_2^{(0)}(1, 0)}{\partial Y_2} Y_{3l}, \tag{2.197}$$

$$\lim_{X_3 \to -\infty} V_{3l}^{(1)} = 0 \tag{2.198}$$

and the conditions of matching with the main deck flow

$$\lim_{Y_{3l} \to \infty} \left(U_{3l}^{(1)} - \frac{\partial U_2^{(0)}(1, 0)}{\partial Y_2} Y_{3l} \right) = \frac{\partial U_2^{(0)}(1, 0)}{\partial Y_2} A_{3m}(X_3, T_3). \tag{2.199}$$

The quasi steady lower deck problem is closed by the unsteady interaction law governing the mutual reaction of lower and upper deck flow

$$-2\frac{\partial P_3^{(1)}}{\partial T_3} - \frac{\partial}{\partial X_3} J_{[n]} \left(P_3^{(1)}; K, \bar{\Gamma}, \bar{\Lambda}, \bar{N} \right) = \frac{2}{H_{03}} \frac{\partial A_{3m}}{\partial X_3}. \tag{2.200}$$

Interestingly enough, the perturbations of the pressure in each deck affected by the interaction process, which are depending only on X_3 and T_3, are the same in all three regions as suggested by the matching conditions (2.137) and (2.157). Thus $P_3^{(1)}(X_3, T_3) := P_{3l}^{(1)} = P_{3m}^{(1)} = P_{3u}^{(1)}$ has been used in the final fundamental formulation of the interaction problem. $J_{[n]}$ is the perturbation of the mass flux density in the upper deck region and defined in an analogous manner to the definition 2.1.2.

The fundamental lower deck problem depends on several parameters, as there are e.g. R_w, μ_w, $\frac{\partial U_2^{(0)}(1,0)}{\partial Y_2}$ or H_{03}. These can be conveniently eliminated by introducing the affine transformation given below

$$X^\star = \mu_w R_w^{\frac{1}{2}} U_{20}'(0)^2 C^{\frac{3}{2}} X_3, \tag{2.201a}$$

$$Y^\star = R_w^{\frac{1}{2}} U_{20}'(0) C^{\frac{1}{2}} Y_{3l}, \tag{2.201b}$$

$$T^\star = \mu_w R_w^{\frac{1}{2}} U_{20}'(0)^2 |\bar{\Gamma}| C^{\frac{1}{2}} T_3, \tag{2.201c}$$

$$U^\star = R_w^{\frac{1}{2}} C^{\frac{1}{2}} U_{3l}, \tag{2.201d}$$

$$V^\star = \mu_w^{-1} R_w^{\frac{1}{2}} U_{20}'(0)^{-1} C^{-\frac{1}{2}} V_{3l}, \tag{2.201e}$$

$$P^\star = C\, P_3, \tag{2.201f}$$

$$A^\star = R_w^{\frac{1}{2}} U_{20}'(0) C^{\frac{1}{2}} A_{3m}, \tag{2.201g}$$

$$S^\star = R_w^{\frac{1}{2}} U_{20}'(0) C^{\frac{1}{2}} S_{3l} \tag{2.201h}$$

with $C := \left| \frac{2\bar{\Gamma}}{K} \right|$ and $U_{20}'(0) := \frac{\partial U_2^{(0)}(1,0)}{\partial Y_2}$.

Remark 2.2.6. Obviously C has to be defined meaning such that $K \neq 0$ and $\bar{\Gamma} \neq 0$. If one of these two conditions is not satisfied, then the above affine transformation has to be modified appropriately. E.g. consider $K \neq 0$ and $\bar{\Gamma} = 0$, but $\bar{\Lambda} \neq 0$, say, then $\bar{\Lambda}$ instead of $\bar{\Gamma}$ can be used in the definition of C.

Insertion into the interaction law (2.186) shows that the material parameters entering the flux function $J_{[n]}$ cannot be eliminated as these are essential parameters of the problem resulting in

$$\Gamma_{-\infty} = \bar{\Gamma} \left| \bar{\Gamma} \right|^{-1}, \tag{2.202}$$

$$\Lambda_{-\infty} = \bar{\Lambda} C^{-1} \left| \bar{\Gamma} \right|^{-1}, \tag{2.203}$$

$$N_{-\infty} = \bar{N} C^{-2} \left| \bar{\Gamma} \right|^{-1}, \tag{2.204}$$

$$Q = 2^{-1} R_w^{-\frac{1}{2}} U'_{20}(0)^{-1} \left| \bar{\Gamma} \right|^{-1} H_{03}^{-1} C^{\frac{3}{2}}. \tag{2.205}$$

Parameter $Q > 0$ measures the intensity of the coupling between lower and upper deck, as follows immediately from the definition of the fundamental canonical problem summarized below.

Definition 2.2.1 (Fundamental canonical problem). *After application of Prandtl's transposition theorem, [64],*

$$T = T^{\star}, \ X = X^{\star}, \ S(X,T) = S^{\star}(X^{\star}, T^{\star}), \ Y = Y^{\star} - S(X,T), \tag{2.206a}$$

$$U(X,Y,T) = U^{\star}(X^{\star}, Y^{\star}, T^{\star}), \tag{2.206b}$$

$$V(X,Y,T) = V^{\star}(X^{\star}, Y^{\star}, T^{\star}) - U \frac{\partial}{\partial X} S, \tag{2.206c}$$

$$P(X,T) = P^{\star}(X^{\star}, T^{\star}), \ A(X,T) = A^{\star}(X^{\star}, Y^{\star}, T^{\star}) + S(X,T) \tag{2.206d}$$

the fundamental lower deck problem for plane parallel oncoming channel flow, see definition 2.1.2, in canonical form is given by

$$\frac{\partial}{\partial X} U(X,Y,T) + \frac{\partial}{\partial Y} V(X,Y,T) = 0, \tag{2.207}$$

$$U \frac{\partial U}{\partial X} + V \frac{\partial U}{\partial Y} = -\frac{\partial}{\partial X} P(X,T) + \frac{\partial^2 U}{\partial Y^2} \tag{2.208}$$

supplemented by the no slip condition at the wall

$$U = V = 0 \qquad @\mathbf{X} = (X, Y = 0)^T, \tag{2.209}$$

the conditions of matching with the undisturbed noninteracting boundary layer upstream

$$\lim_{X \to -\infty} P = 0, \tag{2.210}$$

$$\lim_{X \to -\infty} U = Y, \tag{2.211}$$

$$\lim_{X \to -\infty} V = 0 \tag{2.212}$$

and the conditions of matching with the main deck flow

$$\lim_{Y \to \infty} (U - Y) = A(X, T).$$
(2.213)

The quasi steady lower deck problem is closed by the unsteady interaction law governing the mutual reaction of lower and upper deck flow

$$-\frac{\partial P}{\partial T} + \frac{\partial}{\partial X} \, G_{[n]} \left(P; K, \Gamma_{-\infty}, \Lambda_{-\infty}, N_{-\infty} \right) = Q \frac{\partial}{\partial X} \left(A - S \right).$$
(2.214)

The parameter $Q > 0$, defined in equation (2.205), measures the intensity of the coupling between lower and upper deck. The material parameters $\Gamma_{-\infty}$, $\Lambda_{-\infty}$, $N_{-\infty}$ are defined in equations (2.202) to (2.204). $G_{[n]}$ is the leading order negative disturbance of the mass flux density of the upper deck flow in canonical form given by

$$G_{[n]}(P; K, \Gamma, \Lambda, N) = \begin{cases} \text{sign}(K)P + \frac{1}{2}\text{sign}(\Gamma)P^2 & n = 2 \\ \text{sign}(K)P + \frac{1}{2}\text{sign}(\Gamma)P^2 + \frac{1}{6}\Lambda P^3 & n = 3 \\ \text{sign}(K)P + \frac{1}{2}\text{sign}(\Gamma)P^2 + \frac{1}{6}\Lambda P^3 + \frac{1}{24}NP^4 & n = 4. \end{cases}$$
(2.215)

$G_{[n]}$ has the following properties.

- *The local Mach number $M = \frac{\tilde{u}}{\tilde{c}}$ follows from*

$$M - 1 = -\epsilon_3^{2(n-1)} C^{-1} |\bar{\Gamma}| \frac{\mathrm{d}G_{[n]}}{\mathrm{d}P}.$$
(2.216)

- *The local value of the fundamental derivative and its first derivative is given by*

$$\Gamma = \epsilon_3^{2(n-2)} |\bar{\Gamma}| \frac{\mathrm{d}^2 G_{[n]}}{\mathrm{d}P^2}, \quad \Lambda = \epsilon_3^{2(n-3)} C |\bar{\Gamma}| \frac{\mathrm{d}^3 G_{[n]}}{\mathrm{d}P^3}.$$
(2.217)

Chapter 3

Shock Regularization by Viscous Inviscid Interactions

3.1 Shock Formation and the Fundamental Derivative

After an area of vivid interest in BZT fluids starting with the works of Bethe, [4], Zel'dovich, [96], and Thompson, [85], and lasting to the middle of the 90s, [88], [5], [15], [87], [16], [34], [18], [17], [8], [35], [36], [44], [58], there exists a renewed interest in fluids exhibiting negative or mixed nonlinearity as can be observed by the number of more recent publications dealing with the experimental prediction and detection of anomalous shocks inherent to these kind of fluids, [38], [19], [13], [39], [25], [11], [12], [95]. Given the possible technical applications in turbomachinery, see e.g. [10], [12], these fluids also are of theoretical value on their own. The feature of Gamma changing sign in the flow field has severe consequences for the theory of compressible inviscid flows giving rise to a richer variety of anomalous shock forms not known in the common case of Gamma being strictly positive, i.e. rarefaction shocks, sonic shocks, double sonic shocks and split shocks, see e.g. [56] for a discussion of Riemann problems in general or [14], [8], [35] for a discussion of steady and unsteady weak shocks.

Most important of all, the classical criteria, as the requirement $[s] \geq 0$

following from second law of thermodynamics or the more mathematical
condition for the stability of the resulting wave pattern expressed by Lax's
characteristic criterion, [56], or by the more general Oleinik condition, [61],
[45], are too weak to rule out inadmissible shocks in case of fluids exhibiting
mixed nonlinearity. A shock is considered inadmissible in this context if
there exists no internal shock profile connecting the flow conditions before
and after the shock when physical effects that have been neglected so far but
which become significant in the vicinity of the shock front are considered and
thus regularize the problem. It is commonly known that the consideration
of small effects of viscosity and heat conduction in a small region around the
shock front leads to the formation of such smooth internal shock profiles. A
thoroughly discussion of these profiles for fluids exhibiting mixed nonlinearity
resulting from a regularization by thermo-viscous effects can be found in [14],
[35] or [18]. In the following a quite different mechanism for the regularization
of weak shocks is proposed by making use of the theory of transonic viscous
inviscid interactions in narrow channels introduced in chapter 2. Consider
the situation of a stationary weak normal shock in a channel. The flow
field in the boundary layers at the walls is subjected to a discontinuous
pressure distribution, i.e. a rapid change of the flow field, and a region of
shock boundary layer interaction emerges around the position of the former
shock. It can be expected that the shock/boundary layer interaction leads
to a smoothed transition from super- to subsonic core region flow similar to
the phenomenon of a pseudo-shock encountered in internal gas flows, [54].
Furthermore, if the internal flow can be described by the distinguished limit
for the interaction problem presented in chapter 2, then the inviscid flow in
the core region of the channel conveniently can be described by the equations
for one-dimensional inviscid transonic flow of dense gases, see section 2.1.1
or [35]. This chapter will address the following issues.

- First of all, a definition of what has to be understood by an inter-
  nal shock profile generated by viscous inviscid interactions is given in
  section 3.3.

- Furthermore, it is mandatory to show that such an internal shock profile

truly connects the undisturbed flow state in the core region of the channel before and after the interaction region. To this end, the asymptotic behavior of the solution of the interaction problem far up- and downstream, $X \to \pm\infty$, will be investigated . The undisturbed flow states have to be in accordance with the theory for inviscid flow, a summary of which is given in the following section together with the formulation of appropriate shock admissibility criteria.

- And finally, selected numerical results for various forms of shocks presented in section 3.3 will be discussed. Above all, these allow to identify the physical mechanism being at the basis of the regularizing properties of the interaction problem.

Besides the theoretical value of the discussion to be presented in this chapter, a direct application of the scaling laws proposed in the derivation of the distinguished limit shall be given for the example fluid PP10 which is expected to exhibit a region of negative Γ. A calculation of the characteristic length scale imminent to the problem shows that the phenomena described in this chapter are expected to be encountered for flows of dense gases in technical applications under realistic conditions.

3.1.1 Inviscid Theory of Weak Normal Shocks

A shock forming in a flow regime described by the Euler equations for inviscid flow has to satisfy certain jump conditions, i.e. the Rankine Hugoniot conditions, governing the overall jump of the flow quantities. In the following a bracket $[a] := a^a - a^b$ denotes a jump of some quantity a. The superscripts a and b refer to conditions before and after the shock.

Most important of all, the values of the pressure before and after a shock have to be points on the so called Rayleigh line which can be defined as follows

$$\mathcal{C}_R := \{(p_i^{(1)}, J) : J = J_{[n]}(p_i^{(1)b}; K, \bar{\Gamma}, \bar{\Lambda}, \bar{N})\} \tag{3.1}$$

for the case of stationary weak normal shocks in steady transonic nozzle flow, see section 2.1.1 or [35]. The Rayleigh line in the form of (3.1) expresses the continuity of the mass flux density across a shock front for a given pressure jump $p_i^{(1)} - p_i^{(1)b}$. Graphically, the actual pressure jump $[p_i^{(1)}]$ has to result from an intersection of the Rayleigh line and the graph $\mathcal{C}_J = \{(p_i^{(1)}, J) : J = J_{[n]}(p_i^{(1)}), \ p_i^{(1)} \in [p_i^{(1)b}, p_i^{(1)a}]\}$ in the pressure $p_i^{(1)}$ vs. mass flux density $J_{[n]}$ diagram, see the example in figure 3.1. The jump conditions are supplemented by the entropy condition

$$[s] \geq 0 \tag{3.2}$$

expressing the fact that the thermodynamic entropy has to increase over an admissible shock. Kluwick showed in [35] that the entropy condition (3.2) together with the Rankine Hugoniot conditions can be used to formulate the following inequality

$$[s] \sim -\tfrac{1}{6}\epsilon_1^2 [\rho_i^{(1)}]^2 [M] - \tfrac{1}{360}\epsilon_1^5 \bar{N} [\rho_i^{(1)}]^5 \geq 0 \tag{3.3}$$

which has to hold in case of weak normal shocks described by the one-dimensional theory of the transonic flow of dense gases in slowly varying nozzles in section 2.1.1. From that follows the inequality

$$[M] \leq 0 \tag{3.4}$$

which in case of a stationary weak normal shock is equal to stating that an admissible shock has to lead to a transition from super- to subsonic flow, in general. Interestingly enough, shocks may have sonic upstream conditions $M^b = 1$ or sonic downstream conditions $M^a = 1$ or both. It is in the latter case that the equality sign in equation (3.4) holds.

In case of a strictly convex or concave flux function $J_{[n]}$, i.e. case of positive or negative nonlinearity, the conditions mentioned above are enough to rule out inadmissible shocks. This, however, is not always true in case of mixed nonlinearity which is demonstrated for the example in figure 3.1. The shock connecting the points A and B and the shock connecting the points A
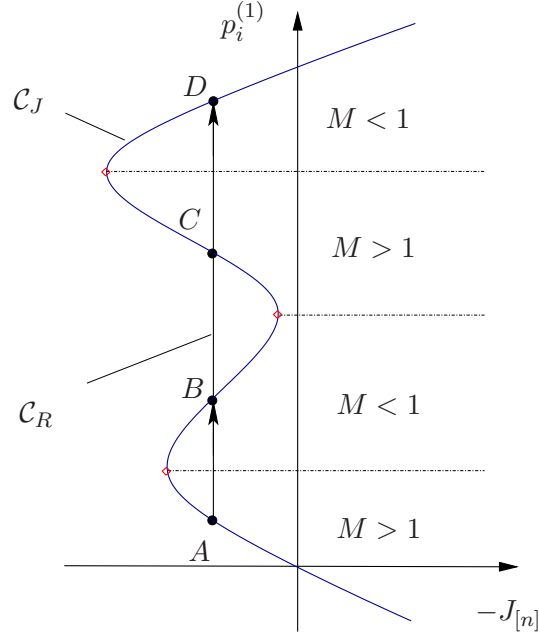
Figure 3.1: Plot of the negative perturbation of the mass flux density $-J_{[n]}$ vs. the pressure $p_i^{(1)}$, denoted by $\mathcal{C}_J$, and a example of a Rayleigh line $\mathcal{C}_R$.

and D both result in a transition from super- to subsonic and hence satisfy the shock admissibility criteria stated so far. However, it turns out that only the shock AB is consistent with a thermo-viscous internal shock profile, cf. e.g. [35]. Therefore, the shock admissibility criteria have been generalized in [35] in order to cover all the possible weak shock forms occurring in steady flows of dense gases governed by a mass flux density $J_{[n]}$ with a nonlinearity of up to forth order in the pressure.

Shock Admissibility Criteria, [35]

Theorem 3.1.1 (Shock admissibility criterion). *A shock forming in the single phase dense gas regime, which is governed by the density of the perturbation mass flux $J_{[n]}$, see definition 2.1.2, for one dimensional nozzle flow, is admissible if and only if the following conditions are met:*

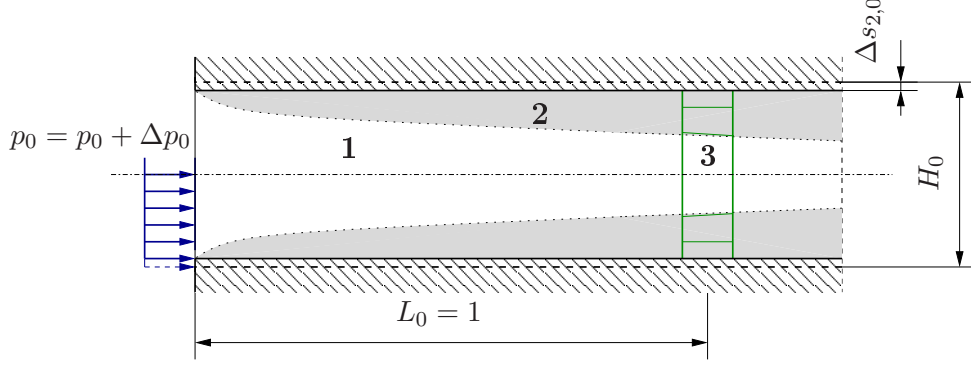   *1. The Rayleigh line connecting the states before and after the shock does*

Figure 3.2: Schematic sketch for introducing small variations of the channel height, $\Delta s_{2,0} = \epsilon_3^{4+n+\mathfrak{N}_{1D}/2} S_{-\infty}$, and of the inflow conditions, $\Delta p_0 = \epsilon_3^2 P_{-\infty}$. If the variations satisfy the relation $G_{[n]}(P_{-\infty}; \dots) = -QS_{-\infty}$, then the interaction region is located at the fixed position $L_0 = 1$.

　　　not cut intervening branches of the graph

$$\mathcal{C}_J = \{(p_i^{(1)}, J) : J = J_{[n]}(p_i^{(1)}), \; p_i^{(1)} \in [p_i^{(1)b}, p_i^{(1)a}]\}.$$

2. *The flow conditions before and after a shock have to satisfy*
   $M^b \geq 1 \geq M^a$.

3. *In case of a double sonic shock, $M^a = 1 = M^b$, the shock has to be an expansion shock.*

Remark 3.1.1. Obviously, the results of the above theorem equally apply to the situation where $J_{[n]}$ is substituted by $G_{[n]}$, equation (2.215) in definition 2.2.1, and where $p_i^{(1)}$ is substituted by P since $G_{[n]}$ is a scaled version of $-J_{[n]}$.

3.2　Varying the Inflow Conditions

The fundamental problem for steady interacting flow is extended to allow small variations of the inflow conditions at the channel entry, represented by Δp_0, and of the channel height, represented by $\Delta s_{2,0}$, see figure 3.2. These small variations shall affect the flow in the interaction region, which shall be located at the fixed position $\tilde{L}_0$, leaving the reference state unchanged independently of the new configuration. Therefore, the scaling of the ma-

terial parameters, (2.201), entering the interaction law in canonical form, (2.215), which are dependent on the reference state, do not change either. This is convenient, because it allows to vary the inflow conditions under an unchanged representation of the flux function $G_{[n]}$. Taking into account the affine transformation (2.201) Δp_0 is defined by

$$\Delta p_0 = \epsilon_3^3 C^{-1} P_{-\infty}, \tag{3.5}$$

which implies

$$\lim_{X \to -\infty} P = P_{-\infty} \tag{3.6}$$

for the upstream value of the pressure in the triple deck. $\Delta s_{2,0}$ has to be of the same vertical length scale as the lower deck and thus

$$\Delta s_{2,0} = \epsilon_3^{4+n+\mathfrak{N}_{1D}/2} R_w^{-\frac{1}{2}} U_{20}'(0)^{-1} C^{-\frac{1}{2}} S_{-\infty}. \tag{3.7}$$

As a result the no slip conditions have to be prescribed at the shifted wall

$$U^{\star} = V^{\star} = 0 \qquad @\mathbf{X}^{\star} = (X^{\star}, Y^{\star} = S_{-\infty})^{T}. \tag{3.8}$$

Note that $\star$ denotes quantities before the application of Prandtl's transposition theorem, (2.206), used in the definition of the fundamental problem in canonical form. Prandtl's transposition theorem for $S(X) \equiv S_{-\infty}$ simplifies to

$$Y = Y^{\star} - S_{-\infty}, \qquad A = A^{\star} + S_{-\infty}. \tag{3.9}$$

Inspection of equations (2.210) and (2.213) reveals

$$\lim_{X \to -\infty} A(X) = 0. \tag{3.10}$$

Integration of the interaction law (2.214) for steady flows with respect to X gives

$$G_{[n]}(P) - Q\left(A - S_{-\infty}\right) = G_{[n]}(P^{\star}) - QA^{\star} = c_1 \qquad (3.11)$$

where the dependence of $G_{[n]}$ on the parameters has been suppressed. Taking note of remark 2.1.6 on equation (2.75), which is the inviscid complement of the above expression, equation (3.11) expresses the continuity of the mass flux of the one-dimensional upper deck flow passing cross sections of the channel which are reduced by the displacement effect $A^{\star}$ caused by the interacting boundary layers at the wall. Consulting Prandtl's transposition theorem $A^{\star}$ results from a geometric variation of the channel height expressed by $S_{-\infty}$ and from a viscous part A generated by the lower deck reaction to pressure variations in the upper deck. Obviously c_1 then quantifies the change of the mass flux which has been effected by the variation of the inflow conditions, i.e. $P_{-\infty}$, and the variation of the channel height $S_{-\infty}$ since $c_1 = 0$ for the initial configuration, i.e. $P_{-\infty} = S_{-\infty} = 0$. Therefore, in order to be consistent c_1 in equation has to be $c_1 = 0$ and consequently $S_{-\infty}$ and $P_{-\infty}$ have to satisfy the compatibility relation

$$G_{[n]}\left(P_{-\infty}; K, \Gamma_{-\infty}, \Lambda_{-\infty}, N_{-\infty}\right) = -QS_{-\infty}. \qquad (3.12)$$

Finally, the changes introduced in this section are summarized in the following definition of the fundamental problem for varying inflow conditions.

Definition 3.2.1 (Fundamental canonical problem (steady interacting flow, varying inflow conditions)). *The fundamental lower deck problem for an oncoming plane parallel channel flow, see definition 2.1.2, in canonical form is given by*

$$\frac{\partial}{\partial X}U(X,Y) + \frac{\partial}{\partial Y}V(X,Y) = 0, \qquad (3.13)$$

$$U\frac{\partial U}{\partial X} + V\frac{\partial U}{\partial Y} = -\frac{\mathrm{d}}{\mathrm{d}X}P(X) + \frac{\partial^2 U}{\partial Y^2} \qquad (3.14)$$

supplemented by the no slip condition at the wall

$$U = V = 0 \qquad @\mathbf{X} = (X, Y = 0)^T, \tag{3.15}$$

the conditions of matching with the undisturbed noninteracting boundary layer upstream

$$\lim_{X \to -\infty} P = P_{-\infty}, \ \lim_{X \to -\infty} U = Y, \ \lim_{X \to -\infty} V = 0 \tag{3.16}$$

and the conditions of matching with the main deck flow

$$\lim_{Y \to \infty} (U - Y) = A(X). \tag{3.17}$$

Y and A defined by Prandtl's transposition theorem, (3.9). The interaction law for steady flow in the interaction region is given by

$$G_{[n]} \left(P; K, \Gamma_{-\infty}, \Lambda_{-\infty}, N_{-\infty} \right) = Q \left(A - S_{-\infty} \right). \tag{3.18}$$

Parameter Q > 0 has been defined in equation (2.205), and the material parameters $\Gamma_{-\infty}$, $\Lambda_{-\infty}$, $N_{-\infty}$ in equations (2.202) to (2.204). $G_{[n]}$ is given by (2.215).

3.3 Eigensolutions & Internal Shock Profiles

An interesting property of nontrivial eigensolutions to the steady interaction problem formulated in definition 3.2.1 is that these correspond to the internal structures of weak normal shocks. As has been mentioned before the internal shock profile resulting from shock boundary layer interaction has to connect the undisturbed flow states before and after the shock which can be expressed by the relations

$$\lim_{X \to -\infty} P = P^b = P_{-\infty}, \quad \lim_{X \to -\infty} A = 0, \quad \lim_{X \to -\infty} U = Y;$$
$$\lim_{X \to \infty} P = P^a, \quad \lim_{X \to \infty} A = 0, \quad \lim_{X \to \infty} U = Y.$$

The values of P before and after the shock, P^b ($= P_{-\infty}$) and P^a, have to satisfy the jump condition $[G_{[n]}] = G_{[n]}(P^a) - G_{[n]}(P^b) = 0$ expressing the continuity of the mass flux across a shock front which is a result of the underlying inviscid theory, see theorem 3.1.1 or [35]. The Rayleigh line for a given undisturbed flow state upstream, P^b, is defined by

$$\mathcal{C}_R = \{(P, G) : G = G_{[n]}(P^b; K, \Gamma_{-\infty}, \Lambda_{-\infty}, N_{-\infty}) = -QS_{-\infty}\}.$$

Hence, by varying $S_{-\infty}$ the Rayleigh line is moved in the $G_{[n]}$ vs. P diagram which is equal to varying P^b and P^a, i.e. the shock strength $[P]$.

It is important to note, that besides a nontrivial eigensolution there always exists a trivial eigensolution to the problem

$$P \equiv P_{-\infty}, \quad A \equiv 0, \quad U \equiv Y.$$

In the following, general properties of eigensolutions shall be discussed and instructive numerical results of internal shock profiles corresponding to weak normal shocks will be given.

3.3.1   Asymptotic Properties Upstream $(X \to -\infty)$

The upstream behavior of the interacting flow for $X \to -\infty$ shall be investigated. Therefore, the analysis of Lighthill, [52], and Stewartson & Williams, [81], dealing with freely interacting boundary layers in external supersonic flows has to be extended to incorporate the algebraic interaction law, (3.18), and the new matching conditions upstream (3.16). The ansatz

$$U = Y - a_1 \mathrm{e}^{\kappa X} f_1(Y), \ V = a_1 \kappa \mathrm{e}^{\kappa X} f_1'(Y), \ P = P_{-\infty} + a_1 \mathrm{e}^{\kappa X}, \qquad (3.19)$$

with $\exp(\kappa X) \to 0$ for $X \to -\infty$, leads to the following expression for f_1

$$f_1'(Y) = \int_0^Y \mathrm{Ai}(\kappa^{\frac{1}{3}} s)\mathrm{d}s, \qquad f_1(Y) = \int_0^Y \int_0^z \mathrm{Ai}(\kappa^{\frac{1}{3}} s)\mathrm{d}s\mathrm{d}z. \qquad (3.20)$$

From that follows the well known result for the displacement function

$$A(X) = \frac{a_1}{3\text{Ai}'(0)} \kappa^{\frac{1}{3}} e^{\kappa X}, \qquad \text{Ai}'(0) < 0 \tag{3.21}$$

where Ai denotes the Airy function, [1]. Substitution of the expressions for P and A into the algebraic interaction law (3.18) and collecting terms of $\mathcal{O}(\exp(m\kappa X))$ with $m \in \mathbb{N}^0$ yields to leading order

$$G_{[n]}\left(P_{-\infty}; K, \Gamma_{-\infty}, \Lambda_{-\infty}, N_{-\infty}\right) = -QS_{-\infty}, \tag{3.22}$$

which is immediately satisfied because of the compatibility assumptions made for the variation of the inflow condition (3.12). The next higher order is found to be

$$G'_{[n]}\left(P_{-\infty}; K, \Gamma_{-\infty}, \Lambda_{-\infty}, N_{-\infty}\right) = \frac{Q}{3\text{Ai}'(0)}\kappa^{\frac{1}{3}} \tag{3.23}$$

yielding a relation for κ

$$\kappa = \left(G'_{[n]}\left(P_{-\infty}; K, \Gamma_{-\infty}, \Lambda_{-\infty}, N_{-\infty}\right)\frac{3\text{Ai}'(0)}{Q}\right)^3. \tag{3.24}$$

A nontrivial eigensolution to the fundamental problem (definition 3.2.1) can only exist, if it decays for $X \to -\infty$. Therefore, considering the sign of $\text{Ai}'(0) < 0$, see [1], and $Q > 0$, see definition 3.2.1, this can only be the case, if $G'_{[n]}(P_{-\infty}, \dots) \leq 0$. Taking into account relation (2.216) this, however, implies that the oncoming channel flow has to be supersonic, i.e. $G'_{[n]}(P_{-\infty}, \dots) < 0$, or sonic in the limiting case $G'_{[n]}(P_{-\infty}, \dots) \to 0-$. An interpretation of internal shock profiles to sonic shocks will be given in the discussion of the numerical results, cf. section 3.3.7 and 3.3.8.

Therefore, one concludes that nontrivial eigensolutions, or in other words admissible internal shock profiles, can only exist if and only if the oncoming flow -that is the flow before the regularized shock- is supersonic or sonic. Moreover, this result is in accordance with the shock admissibility criteria formulated for inviscid nozzle flow.

Linear Spatial Stability of Undisturbed Flow States

The generalized ansatz of Lighthill used before, (3.19), can be extended even further in order to study the linear spatial stability of an arbitrary undisturbed flow state represented by $P_{-\infty}$ and $S_{-\infty}$ which always is a trivial solution of the interaction problem. To this end we write

$$
\begin{aligned}
U &= \Re\{\hat{U}\} = Y - \Re\{a_1 \mathrm{e}^{\kappa X - \mathrm{i}\omega T} f_1(Y)\}, \\
V &= \Re\{\hat{V}\} = \Re\{a_1 \kappa \mathrm{e}^{\kappa X - \mathrm{i}\omega T} f_1'(Y)\}, \\
P &= \Re\{\hat{P}\} = P_{-\infty} + \Re\{a_1 \mathrm{e}^{\kappa X - \mathrm{i}\omega T}\}
\end{aligned}
\tag{3.25}
$$

with $\omega \in \mathbb{R}$ some given harmonic frequency and $\kappa \in \mathbb{C}$ the corresponding unknown complex wave number. Furthermore, $X,\ Y, P_{-\infty} \in \mathbb{R}$, $a_1 \in \mathbb{C}$ and $f_1 : \mathbb{R} \to \mathbb{C}$.

By plugging (3.25) into the equation for the quasi steady lower deck flow (3.13) to (3.16) one recovers the already obtained result for f_1, equation (3.20),

$$
f_1'(Y) = \int_0^Y \mathrm{Ai}(\kappa^{\frac{1}{3}} s)\mathrm{d}s, \qquad f_1(Y) = \int_0^Y \int_0^z \mathrm{Ai}(\kappa^{\frac{1}{3}} s)\mathrm{d}s\mathrm{d}z
$$

with the main difference that now $\kappa \in \mathbb{C}$. Taking a look at the asymptotic properties of the Airy function $\mathrm{Ai}(z)$ for $z \in \mathbb{C}$ and $|z| \to \infty$, see appendix C, the integrals only exist properly for $Y \to \infty$ if $\kappa \in \{z \in \mathbb{C} : |\mathrm{Arg}(z)| \leq \pi/3\}$. Evaluating the matching condition (3.17) then leads to

$$
A = \Re\{\hat{A}\} = \Re\{\frac{a_1}{3\mathrm{Ai}'(0)} \kappa^{1/3} \mathrm{e}^{\kappa X - \mathrm{i}\omega T}\}
\tag{3.26}
$$

and after insertion into the linearized interaction law for unsteady flow one finally obtains a relation between the harmonic frequency and the complex wave number

$$
\mathrm{i}\omega + G_{[n]}'(P_{-\infty})\kappa = \frac{Q}{3\mathrm{Ai}'(0)} \kappa^{4/3}
\tag{3.27}
$$

where the dependence of $G_{[n]}$ on the parameters $K, \Gamma_{-\infty}, \Lambda_{-\infty}, N_{-\infty}$ has been

suppressed. Provided $G'_{[n]}(P_{-\infty}) \neq 0$ (3.27) can be written in the following way

$$\mathrm{i}\bar{\omega} + \bar{\kappa} = \mathrm{sign}\left(\mathrm{Ai}'(0)G'_{[n]}(P_{-\infty})\right)\bar{\kappa}^{4/3} \qquad (3.28)$$

introducing a modified definition of the harmonic frequency and of the wave number, $\bar{\omega}$ and $\bar{\kappa}$,

$$\bar{\omega} = C\frac{\omega}{G'_{[n]}(P_{-\infty})} \in \mathbb{R}, \qquad (3.29)$$

$$\bar{\kappa} = C\kappa \in \mathbb{C} \qquad (3.30)$$

with

$$C = \left|\frac{Q}{3\mathrm{Ai}'(0)G'_{[n]}(P_{-\infty})}\right|^3 > 0. \qquad (3.31)$$

It is important to note that the new definition $\bar{\kappa}$ for the wave number is only a rescaling of κ, i.e. $\mathrm{Arg}(\kappa) = \mathrm{Arg}(\bar{\kappa})$. Interestingly enough, for the discussion of (3.28) only two cases have to be considered, i.e. $G'_{[n]} < 0$ and $G'_{[n]} > 0$. That is, one simply has to distinguish between supersonic and subsonic flow.

A candidate for a solution to (3.28) for a given $\bar{\omega}$ can be obtained by finding a root of the polynomial

$$\mathrm{sign}\left(\mathrm{Ai}'(0)G'_{[n]}(P_{-\infty})\right)\bar{\kappa}^4 - \bar{\kappa}^3 - 3\mathrm{i}\bar{\omega}\bar{\kappa}^2 + 3\bar{\omega}^2\bar{\kappa} + \mathrm{i}\bar{\kappa}^3 = 0 \qquad (3.32)$$

which has been obtained by taking the left and right hand side of (3.28) to the power of three. The roots plotted in figure 3.3 have been checked against (3.28). It has been found that all four roots of the polynomial (3.32) are a solution of (3.28) as well.

Out of the four possible wave numbers $\bar{\kappa}$ for a given harmonic frequency of some disturbance $\bar{\omega}$ only those that lie in the set $\Omega_\kappa = \{z \in \mathbb{C} : |\mathrm{Arg}(z)| \leq \pi/3\}$, depicted by the shaded region in figure 3.3, lead to a nontrivial solution of the lower deck as has been noted before. On the other hand, for the linear spatial stability of the trivial solution of the interaction problem the real

part of $\bar{\kappa}$ has to be negative, $\Re\{\bar{\kappa}\} < 0$, i.e. some disturbance generated at a purely harmonic frequency $\bar{\omega}$ is dying out downstream. In case of $\Re\{\bar{\kappa}\} > 0$ the disturbances are growing exponentially downstream until nonlinearity takes over.

Keeping that in mind, figure 3.3 allows for the following interpretation. Taking a look at 3.3.1(a), the case of a supersonic trivial solution of the interaction problem, and setting $\bar{\omega} = 0$, i.e. applying a steady disturbance, one obtains the result for the first three wave numbers $\bar{\kappa}_{1,2,3} = 0$, which is the trivial solution again, and $\bar{\kappa}_4 = 1 \in \mathbb{R}$. $\bar{\kappa}_4$ lies within the set Ω_κ and therefore ansatz (3.25) leads to a nontrivial solution for $\bar{\kappa}_4$ which is growing downstream because of $\Re\{\bar{\kappa}\} > 0$. Making use of (3.29) the result (3.24) based on Lighthill's ansatz (3.19) is retrieved. For $\bar{\omega} \in [-\bar{\omega}_c, \bar{\omega}_c]$ there exists only the one nontrivial solution on the branch 4 which is exponentially growing downstream. For $\bar{\omega} > |\bar{\omega}_c|$ the second branch, number 3 in figure 3.3.1(a), enters the region Ω_κ. The situation in the case of a subsonic trivial solution of the interaction problem is quite different, see figure 3.3.1(b). For $\bar{\omega} = 0$ no nontrivial growing mode can exist since $\bar{\kappa}_{1,2,3,4} \in \mathbb{C} \setminus \Omega_\kappa$. This situation does not change as long $\bar{\omega} \in [-\bar{\omega}_c, \bar{\omega}_c]$, however, as soon as $\bar{\omega} > |\bar{\omega}_c|$ the branch 4 enters Ω_κ and a growing mode exists besides the trivial flow state.

Therefore, the supersonic trivial flow state, i.e.

$$P = P_{-\infty}, \ A = 0, \ U = Y, \ G'_{[n]}(P_{-\infty}) < 0,$$

is unconditional unstable according to the concept of linear spatial stability and the subsonic trivial flow state, i.e.

$$P = P_{-\infty}, \ A = 0, \ U = Y, \ G'_{[n]}(P_{-\infty}) > 0,$$

is stable as long the harmonic frequency of the disturbance satisfies the condition $\bar{\omega} \in [-\bar{\omega}_c, \bar{\omega}_c]$.
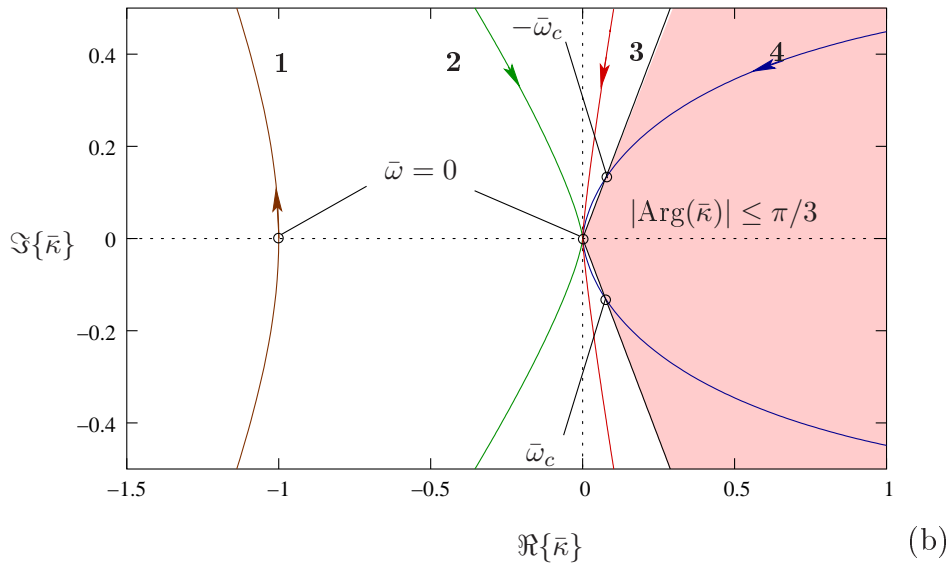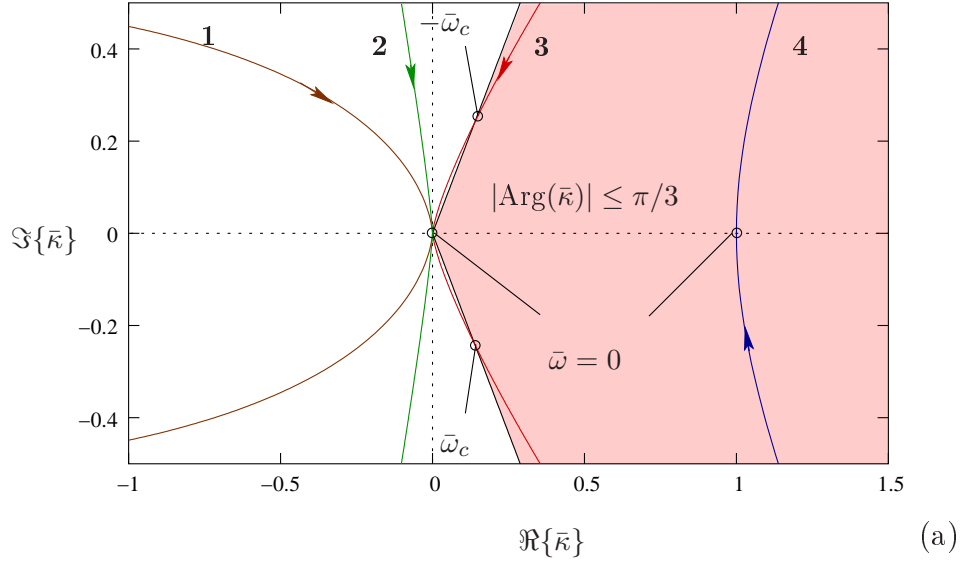
Figure 3.3: Roots $\bar{\kappa}$ of equation (3.28) under variation of $\bar{\omega}$ for a) supersonic, i.e. $G'_{[n]}(P_{-\infty}) < 0$, and b) subsonic, i.e. $G'_{[n]}(P_{-\infty}) > 0$, undisturbed initial flow.

3.3.2   Asymptotic Properties Downstream ($X \to \infty$)

In order to justify the interpretation of nontrivial eigensolutions as internal shock profiles it is mandatory to show that the flow in the interaction region approaches an undisturbed flow state downstream of the interaction region indeed. The investigation of the downstream behavior exactly follows the analysis performed by Kluwick, Exner & Cox, [42]. They applied the results found by Gittler, [23], for the asymptotic properties of steady triple deck problems of a general kind in case of $Y \gg 1$ and $X \gg 1$ to a triple deck problem with a local interaction law, closely resembling (2.214) and describing the interaction process of weakly nonlinear bores in laminar high Reynolds number flow. The significant and fundamental difference to the interaction problem considered in this treatise is, besides the different underlying physics involved, that their interaction law accounts only for terms of quadratic nonlinearity in the pressure and that additionally a dispersive term is present in their relation.

Their starting point has been the expansion of the stream function $\Psi(X, Y)$: $U = \partial\Psi/\partial Y, \ V = -\partial\Psi/\partial X$ for $Y \to \infty$

$$\Psi(X, Y) \sim \frac{1}{2}\left(Y + A(X)\right)^2 + P(X) + K_{rs}Y^r(lnY)^s + \dots \qquad (3.33)$$

with $r < 2$. This expression is valid for all X and contains free constants K_{rs}. Since the flow structure far upstream is given by (3.19) and (3.20), the corresponding velocity disturbances $U - Y$, V decay exponentially with $Y \to \infty$ because of the asymptotic properties of the Airy function, see [1]. Consequently the algebraic terms in Y in (3.33) vanish, $K_{rs} = 0$. Therefore, if the assumption that the interacting flow approaches an undisturbed state downstream is correct, then Ψ has to take on the following form far downstream

$$\Psi(X, Y) \sim \frac{1}{2}Y^2 + A(X)Y + P^a + \dots \qquad X \to \infty, \ Y \to \infty. \qquad (3.34)$$

This result has to be compared with the similarity form of the stream function

far downstream, [23],

$$\Psi(X, Y) \sim \frac{1}{2}Y^2 + \alpha X^\beta f_2(\eta) + C_2 X^\lambda h_2(\eta) + \cdots, \qquad \eta = \frac{Y}{X^{1/3}}. \quad (3.35)$$

If as in the present case no external agencies are affecting the flow under consideration (no external surface mounted obstacle, say) then the parameter $\alpha = 0$ thereby eliminating the second term in (3.35). The third term represents a homogeneous eigensolution with the eigenvalue λ and its asymptotic behavior of $h(\eta)$ for $\eta \to \infty$ has been given by Gittler in [23]

$$h(\eta) \sim K_1\eta + K_2\eta^{3\lambda} + K_3 \mathrm{e}^{-3\lambda-4}\mathrm{e}^{-\eta^2/9} + \ldots \qquad \eta \to \infty. \quad (3.36)$$

The two constants K_1 and K_3 are arbitrary while

$$K_2 = \frac{\Gamma\left(\frac{2}{3}\right)3^{-2\lambda+1/3}}{(3\lambda-1)\Gamma(\lambda+1)} \quad (3.37)$$

with $\Gamma(\cdot)$ denoting the Gamma function. Therefore, in the end a second expression describing the properties of Ψ in the limit $X \to \infty, Y \to \infty$ is obtained

$$\Psi(X, Y) \sim \frac{1}{2}Y^2 + C_2 K_1 X^{\lambda-1/3}Y + C_2 K_2 Y^{3\lambda} + \ldots, \\ X \to \infty, Y \to \infty. \quad (3.38)$$

Comparison of the two expressions, (3.34) and (3.38), for Ψ implies $\lambda = 0$ and

$$A(X) \sim C_2 K_1 X^{-1/3}, \qquad X \to \infty. \quad (3.39)$$

Finally, substitution of (3.39) into the linearized interaction law for steady flow, (3.18), yields the asymptotic behavior of the pressure downstream. Provided $G'_{[n]}(P^a) \neq 0$ it assumes

$$P(X) \sim P^a + \frac{QC_2K_1}{G'_{[n]}(P^a)}X^{-1/3}, \qquad X \to \infty \quad (3.40)$$

again suppressing the dependence of $G_{[n]}$ on the scaled parameters K, $\Gamma_{-\infty}$, $\Lambda_{-\infty}$ and $N_{-\infty}$. However, if the shock terminates in a sonic flow state far downstream, i.e. $G'_{[n]}(P^a) = 0$, then the asymptotic behavior of the pressure downstream is given by

$$P(X) \sim P^a + sign\left(G''(P^a)\right) \left(\frac{2QC_2K_1}{G''_{[n]}(P^a)}\right)^{1/2} X^{-1/6}, \qquad X \to \infty \quad (3.41)$$

indicating an even weaker algebraic decay of the pressure than that found in case of $G'_{[n]}(P^a) \neq 0$. Interestingly enough, the expression $2QC_2K_1/G''_{[n]}(P^a)$ in (3.41) is found to be always positive due to the fact that C_2K_1 has the same sign as A. Figure 3.4 gives a geometrical justification for this statement for two typical variants of a sonic shock. The sign of A follows from $QA = G_{[3]}(P) - (-QS_{-\infty})$ for $P \in [P^b, P^a]$. In case of the shock connecting the points A and C the curvature of the flux function $G''_{[3]} < 0$ at the sonic state and $A \leq 0$ for $P \in [P^b, P^a]$. Therefore, C_2K_1 is negative. In the other case of a shock connecting the points D and B $G''_{[3]} > 0$ at the sonic state and $A \geq 0$ and consequently C_2K_1 is positive. In both cases $2QC_2K_1/G''_{[3]}(P^a)$ is a positive quantity.
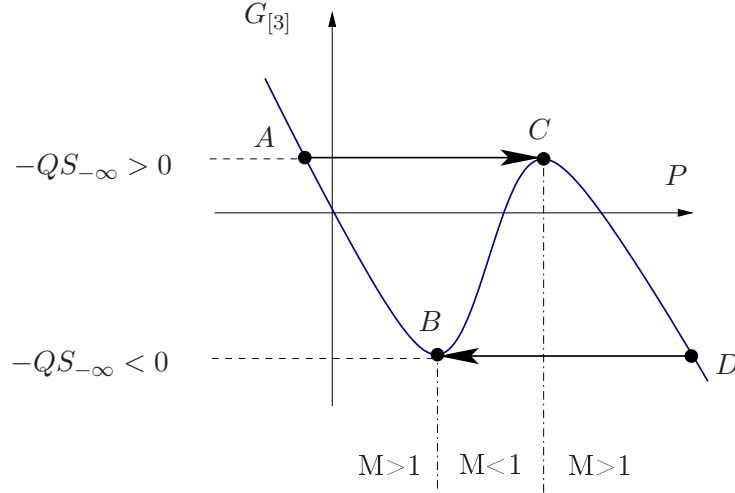

Figure 3.4: Two examples for a shock terminating in a sonic state. At point C: $G''_{[3]} > 0$, and at point B: $G''_{[3]} < 0$.

Therefore, it is found that the flow in the interaction region, represented by nontrivial eigensolutions of the triple deck problem, approaches an undisturbed flow state downstream of the interaction region at a pressure P^a predicted by inviscid theory. The flow before and after the shock is truly connected by an internal shock profile and, since $A(X) \to 0$ for $X \to \pm\infty$, the pressure jump across the shock is given by $[G_{[n]}] = G_{[n]}(P^a) - G_{[n]}(P^b)$ in accordance with the jump/Rankine Hugoniot conditions for the inviscid case, see section 3.1.1.

Moreover, the requirement that the Rayleigh line connecting the states before and after the shock does not cut intervening branches of the graph $\mathcal{C}_G = \{(P, G_{[n]}(P)) \mid P \in [P^b, P^a]\}$ formulated in the shock admissibility criteria in theorem 3.1.1 can be motivated too. Since a nontrivial eigensolution can only exist for supersonic flow conditions upstream, i.e. $G'_{[n]}(P^b) < 0$ (see discussion of the asymptotic behavior of nontrivial eigensolutions in section 3.3.1), the next undisturbed state, which a fluid particle passing through the interaction region is approaching far downstream, is bound to be subsonic or sonic, i.e. $G'_{[n]}(P^a) > 0$. The results of section 3.3.1 also showed that the subsonic undisturbed flow state is stable according to the concept of linear spatial stability at least for disturbances with a harmonic frequency below some bound $\bar{\omega}_c$. Consequently, without the action of external agencies like a variation of the throat area of the channel the fluid particle is attracted towards the undisturbed subsonic flow state and will not pass through it. Hence the Rayleigh line does not cross the graph $\mathcal{C}_G$.

So far the internal shock profiles which are resulting from a shock regularization due to viscous inviscid interactions are in accordance with the prediction based on the the shock admissibility criteria formulated for the noninteracting inviscid case, theorem 3.1.1. However, the last issue of theorem 3.1.1 stating that a double sonic shock is bound to be a rarefaction shock can only be seen by studying numerical results for the nontrivial eigensolutions of the interaction problem. The case of a double sonic shock will be addressed in section 3.3.8 after the discussion of the internal shock profiles for a standard compression and rarefaction shock, section 3.3.5 and 3.3.6, where the flux function $G_{[n]}$ exhibits a quadratic nonlinearity (case of positive or

negative nonlinearity, i.e. $n = 2$) and for a nonstandard sonic shock (section 3.3.7, where $G_{[n]}$ is of third order in the pressure, i.e. $n = 3$), a case of mixed nonlinearity. Finally, section 3.3.9 will deal with the case of a split shock, a case of mixed nonlinearity where as in case of a double sonic shock as well $G_{[n]}$ is of forth order in the pressure, i.e. $n = 4$.

3.3.3   Numerical Results & Numerical Method

The fundamental problem, see definition 3.2.1, is integrated using a finite difference scheme of second order and by applying a marching technique downstream in X-direction, the main flow direction, starting from an initial velocity profile which is given by the flow profile for a nontrivial eigensolution far upstream, cf. section 3.3.1.

To this end, a new variable $\bar{U} := U - Y$ is introduced, whereas V in the momentum equation (3.14) is expressed by means of the continuity equation (3.13) via

$$V(X, Y) = - \int_0^Y \frac{\partial \bar{U}}{\partial X}(X, \bar{Y}) \mathrm{d}\bar{Y}.$$

With the mapping of Y onto the computational domain $\eta \in [0, 1]$

$$Y(\eta) = Y_s \left(\frac{1}{1 - \alpha_s \eta} - \frac{1}{1 + \alpha_s \eta} \right)$$

with the scaling parameters α_s , Y_s the representation of the numerical grid in the new coordinates (X, η) is introduced

$$(X_i, \eta_j) = (X_0 + i\Delta X_i, j\Delta \eta) \quad i \in \mathbb{N}^0, \ j = 0, \dots N_j$$

where the step size in X-direction ΔX_i is adaptable and the step size in η direction $\Delta \eta = 1/N_j$ is fixed. X_0 represents some initial value which is no loss of generality because of the translation invariance of the eigensolutions. Specifically, values $\alpha_s = 0.75$, $Y_s = 20.0$ for the results for $n = 2$, 3 in section 3.3.5, 3.3.6 and section 3.3.7 and $Y_s = 10.0$ for the results for $n = 4$

in section 3.3.8 and 3.3.9.

The derivatives in X-direction are resolved by means of a Cranck-Nicholson discretization, making use of the known/old velocity profile evaluated upstream at X_{i-1} and the unknown/new velocity profile downstream at the next grid point at X_i. For the derivatives in η-direction central differences evaluated at the grid point η_j are used.

The matching condition (3.17) is implemented as

$$A = \bar{U}(X, Y_{max} = Y(1)).$$

This is justified because of the exponential decay of $\bar{U}$ for $Y \gg 1$ which one infers from the asymptotic representation of the stream function Ψ for $Y \gg 1$, $\forall X$, see the discussion following equation (3.33).

The results of the numerical calculations presented in the following sections 3.3.5, 3.3.6 and 3.3.7 have been obtained by choosing the values $Y_{max} = 68.57$ and $Y_{max} = 34.29$ in the sections 3.3.8 and 3.3.9. The number of grid points in η-direction $N_j = 200$.

In the rare cases, where separation occurs, the FLARE approximation, Reyhner & Flügge-Lotz, [67], has been applied which yields reasonable good results as long as the region of separated flow remains small, [2].

3.3.4 Calculation of the Material Parameters for PP10

Due to the canonical form of the fundamental problem, its solutions are independent of specific physical values for the parameters governing the channel geometry and working medium. However, it is instructive to choose a definitive physical setup for numerical experiments in order to verify that the proposed scalings, which are at the bottom of the interaction problem considered here, do lead to sensible numerical values for the scaled material parameters, $\Gamma_{-\infty}$, $\Lambda_{-\infty}$, $N_{-\infty}$ and Q, in case of realistic working media, inflow conditions and geometric dimensions.

As an example medium for a possible candidate of a BZT fluid PP10, $C_{13}F_{22}$, has been chosen. Guardone & Argrow, cf. [25], commented on the expected thermal stability of PP10 and presented more recent material prop-

Commercial name	Chemical formula	$\tilde{M}$ (g/mol)	$\tilde{\theta}_c$ (K)	$\tilde{P}_c$ (atm)	Z_c	$\tilde{\theta}_b$ (K)	$\frac{\tilde{c}_{v,\infty}^c}{\tilde{R}}$	n	ω
PP10	$C_{13}F_{22}$	574	630.2	16.2	0.2859	467	78.37	0.5255	0.4833

Table 3.1: Experimental data for PP10, [25]. $\tilde{M}$ molecular weight, $\tilde{P}_c$ critical pressure, $\tilde{\theta}_c$ critical temperature, Z_c critical compressibility factor, $\tilde{\theta}_b$ boiling temperature at 1 atm, $\tilde{c}_{v,\infty}^c$ specific heat for dilute states ($\rho \to 0$) at $\tilde{\theta}_c$, $\tilde{R}$ specific gas constant, n exponent in (3.43), ω acentric factor

erties than those that can found in [16] or [17], see table 3.3.4. Another promising class of media suitable for experimental usage are Siloxanes, [12].

The fundamental derivative is a secondary thermodynamic quantity, i.e. it cannot be accessed by direct measurements or, in case of numerical calculations, partial derivatives of the thermodynamic state variables $\tilde{p}$ and $\tilde{\rho}$ have to be calculated for isentropic flow conditions; see the definition of Γ in equation (1.1). Therefore, a functional representation of the thermodynamical equation of state (EOS) for PP10 has to be chosen. The selection of an appropriate EOS, also in the light of the scarce and inaccurate data accessible, is a vast field in itself, see [19], [25], [11], [12] or [95]. For the presented numerical calculations the Martin-Hou EOS, [53], has been chosen, since the Martin-Hou EOS is reasonably realistic in predicting regions of negative Γ using a small number of experimental data and being applicably with acceptable numerical efforts.

Since the Martin-Hou EOS is only a thermal EOS, i.e. an incomplete form of an EOS in the sense that it provides a function for $\tilde{p} = \tilde{p}(\tilde{\theta}, \tilde{\rho})$ only, the thermodynamic character of the fluid under consideration has to be completed by providing a caloric EOS

$$\tilde{e}(\tilde{\theta}, \tilde{\rho}) = \tilde{e}_r + \int_{\tilde{\theta}_r}^{\tilde{\theta}} \tilde{c}_{v,\infty}(\tau)\mathrm{d}\tau + \int_{\tilde{\rho}_r}^{\tilde{\rho}} \left(\tilde{\theta}\frac{\partial \tilde{p}}{\partial \tilde{\theta}}(\tilde{\theta}, \varrho) - \tilde{p}(\tilde{\theta}, \varrho) \right) \, \mathrm{d}\left(\tfrac{1}{\varrho} \right), \quad (3.42)$$

[53], [25], where $\tilde{e}$ denotes the specific inner energy, the subscript r denotes some reference state and the subscript ∞ indicates that the quantity is evaluated for dilute states, i.e. $\tilde{\rho} \to 0$. Following [88] the functional form of $\tilde{c}_{v,\infty}(\tilde{\theta})$ in the neighborhood of the critical temperature is approximated by

a power law

$$\tilde{c}_{v,\infty} \simeq \tilde{c}_{v,\infty}^c \left(\frac{\tilde{\theta}}{\tilde{\theta}_r} \right)^n . \tag{3.43}$$

The numerical implementation of the EOS for the calculation of Γ and its higher derivatives Λ and N follows the procedure applied by Colonna in [13], which moreover gives a very comprehensive selection of various thermodynamic expressions applicable for the calculation of secondary thermodynamic quantities.

The dynamic viscosity has been calculated using the method of Chung, Ajlan, Lee & Starling, [9] for nonpolar fluids. The data used is listed in table 3.3.4. The method itself as well as the used data have to be taken with caution, [36], in case of dense gases, however, the main purpose here is simply to provide realistic values for the transport quantity.

Finally, one has to make assumptions on the position of the interaction region in the channel. For the numerical results presented in the following sections it has been assumed that the interaction region is located at $\tilde{L}_0 = 1$m from the channel entry. Furthermore, $\mathfrak{N}_{1D} = 1$, see section 2.2.1, being the most general situation.

The properties of the undisturbed boundary layer needed in the affine transformation (2.201), i.e. R_w, μ_w and U'_{20}, are obtained by considering the compressible boundary layer equations in the limit of dense gases having large relative specific heats. In section 2.1.2 it has been argued that in case of a plane parallel constant flow in the core region of the channel the temperature and the pressure are constant in the whole boundary layer. Therefore, $R_w = 1$ and $\mu_w = 1$. The boundary layer flow can be considered to be incompressible and has a self-similar representation in the form of (2.103) leading to $U'_{20} = f'(0)$. $f'(0) = 0.332$ can be calculated by numerically solving Blasius' equation (2.104) or by referring to the literature.

Figure 3.5 shows the various pressure and density pairs at channel entry used for the numerical calculations in the following sections.
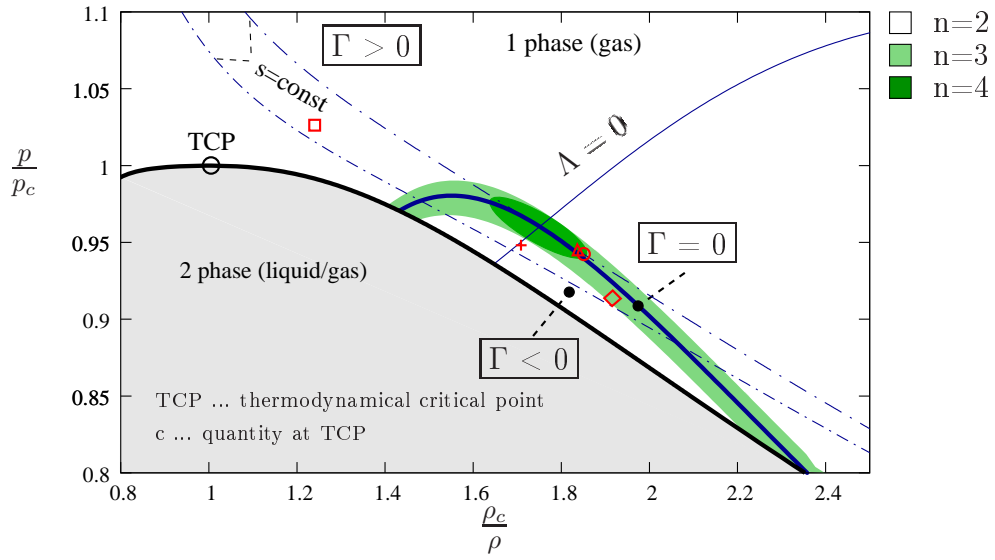
Figure 3.5: Reduced pressure vs. reduced density diagram for PP10 according to the Martin-Hou EOS. Red symbols mark the pressure and density at channel entry used in the numerical calculations. □: example 1, section 3.3.5, +: example 2, section 3.3.6, ◊: example 3, section 3.3.7, ◯ : example 4, section 3.3.8, △: example 5, section 3.3.9. n indicates the nonlinearity in the pressure to be considered in the interaction law.

3.3.5 Example 1: Compression Shock

As first example the internal profile of a compression shock is considered here. The selected inflow conditions and scaled quantities are summed up in table 3.2. The chosen inflow pressure and the inflow density are depicted in the pressure vs. density diagram for PP10 shown by figure 3.5.

On the left hand side in figure 3.6 the negative perturbation of the mass flux density $G_{[2]}$ vs. the pressure P is shown. As stated in the shock admissibility criteria theorem 3.1.1, the pressure before and after the shock in inviscid flows, P^b and P^a, are connected by the Rayleigh line. The arrow indicates the transition from super- to subsonic as required by the admissibility criteria. Sonic flow conditions are obtained at $P = 1$ where $G_{[2]}$ exhibits an extremum. A shock discontinuity in the pressure is sketched to the right in figure 3.6 indicated by the dashed lines. Interestingly enough, the shock discontinuity predicted by the theory of inviscid flows resolves into a smooth transition from super- to subsonic the moment the interacting boundary layers at the wall are considered in the model as is shown for the pressure, displacement thickness and wall shear stress distribution in figure 3.6. Moreover, figure 3.6 immediately gives an interpretation for the physical mechanism of shock regularization encountered. If the distribution of the displacement thickness $-A$ would be a given function of X, then the interaction law (3.18) would describe the inviscid core region flow of dense gases through a nozzle of variable throat area, compare section 2.1.1 or equation (2.75). However, in contrast to a nozzle of fixed geometry the flow in the boundary layers at the wall and thus $-A$ has the possibility to adapt to the local pressure acting in the interaction region. Since the pressure in a compressive pseudo-shock is increasing monotonously, $\frac{dP}{dX} \geq 0$, the flow passing through the upper deck is decelerated throughout the interaction region, see (2.180). This is brought about by a reduction of the effective throat area, i.e. by an increase of the disturbance of the displacement thickness, $\frac{d(-A)}{dX} > 0$, in the part of the upper deck where the flow is supersonic. A smooth transition of the upper deck flow through the sonic state characterized by $P = 1$ can only be effected if at the same time the effective throat exhibits an extremum, i.e. $\frac{d(-A)}{dX} = 0$, see figure 3.6.

p_0/p_c	ρ_c/ρ_0	θ_0/θ_c	$\tilde{u}_0$ (m/s)	$\tilde{\mu}_0$ (Pas)	K	Γ_0	Re
1.0268	1.240	1.00490	28.1	$3.67\ 10^{-5}$	< 0	1.00	$3.88\ 10^8$
ϵ_3	Δ_3	δ_{3l}	δ_{3m}	H_{3u}		$\Gamma_{-\infty}$	Q_1
0.166	0.00455	$8.42\ 10^{-6}$	$5.08\ 10^{-5}$	0.0112		1.00	4.26

Table 3.2: Selected inflow conditions at channel entry and resulting scaled parameters for the interaction problem. $Q_1 = Q(H_{30} = 1)$.
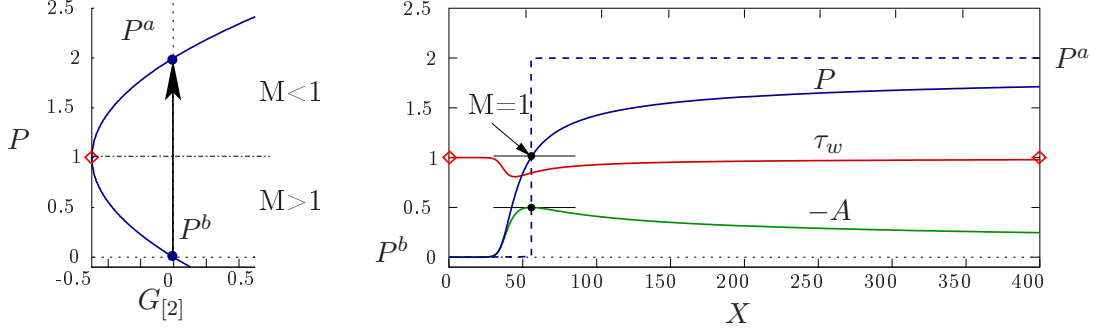
Figure 3.6: To the left, plot of the mass flux density $G_{[2]}$ for quadratic nonlinearity in the pressure and Rayleigh line connecting the pressure before and after the shock, P^b and P^a. To the right, plot of the perturbation of the pressure, displacement thickness and wall shear for $Q = 1$, $S_{-\infty} = 0$.

After the sonic state has been transversed the upper deck flow is subsonic and a further deceleration is achieved by a successive decrease of $\frac{\mathrm{d}(-A)}{\mathrm{d}X} < 0$. On the other hand, the displacement effect characterized by $-A$ originates from the lower deck reacting to the acting pressure gradient. Because of the small velocities close to the walls the flow in the lower deck behaves incompressible, see section 2.2.2, and consequently, the reduction of the effective throat area for the upper deck flow, corresponding to $\frac{\mathrm{d}(-A)}{\mathrm{d}X} > 0$, is brought about by a deceleration of the lower deck flow and the increase, i.e. $\frac{\mathrm{d}(-A)}{\mathrm{d}X} < 0$, by an acceleration. Finally the lower deck flow reaches an undisturbed flow profile far downstream again. Summing up, one therefore concludes that the viscous boundary layers are forming a "viscous" Laval nozzle that adapts to the pressure, diminishing or expanding the effective throat area the upper deck flow feels ensuring a smooth transition of the flow conditions from super- to subsonic and thus regularizing a possible shock discontinuity in the inviscid upper deck flow.

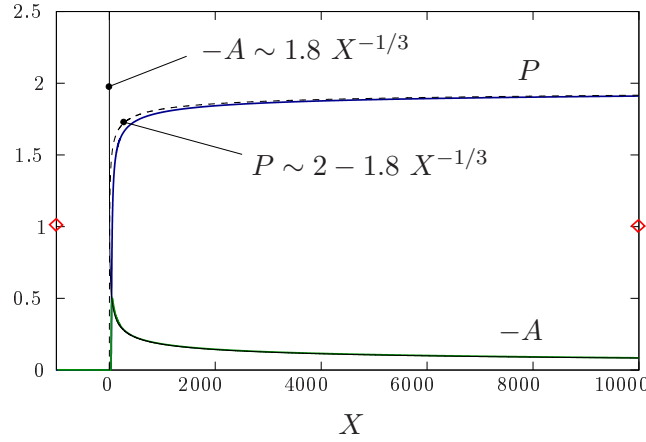Furthermore, the internal shock profile truly connects the undisturbed

Figure 3.7: Plot of the pressure P and the displacement thickness $-A$ for $Q = 1$, $S_{-\infty} = 0$ and comparison of the asymptotic behavior far downstream $X \gg 1$ predicted by equation (3.39) and (3.40).

flow states up- and downstream of the interaction region represented by $P^b = 0$ and $P^a = 2$. As this can be seen simply by inspection of the numerical results for the upstream part of the shock profile due to the exponential behavior exhibited by the solution for $X \to -\infty$, see equation (3.19), the theory predicts only a weak algebraic decay for the far downstream behavior, see (3.40) and (3.39). Therefore, the theoretically expected downstream pressure P^a has to be confirmed by the comparison between the leading order terms of the pressure and displacement thickness for $X \gg 1$ with numerical results, shown in figure 3.7. In the first step, the function describing the asymptotic far downstream behavior of A (3.39) is fitted to the numerical results delivering the numeric value for $C_2 K_1 \approx -1.8$ in (3.39). In the next step the unknown coefficient in (3.40) can be calculated leading to $P \sim 2 - 1.8 X^{-1/3}$ taking into account $P^a = 2$. Therefore, in the limit $X \to \infty$ an undisturbed flow state, $P \to P^a$ and $A \to 0$, is approached far downstream as well.

Figure 3.8 shows the influence of the parameter Q entering the interaction law on the distribution of the pressure, displacement thickness and wall shear stress. As has been mentioned earlier, Q is a measure for the intensity of the coupling between the upper- and lower deck reactions to changes in the flow field. Taking a look at the definition of Q, (2.205), a variation of Q could
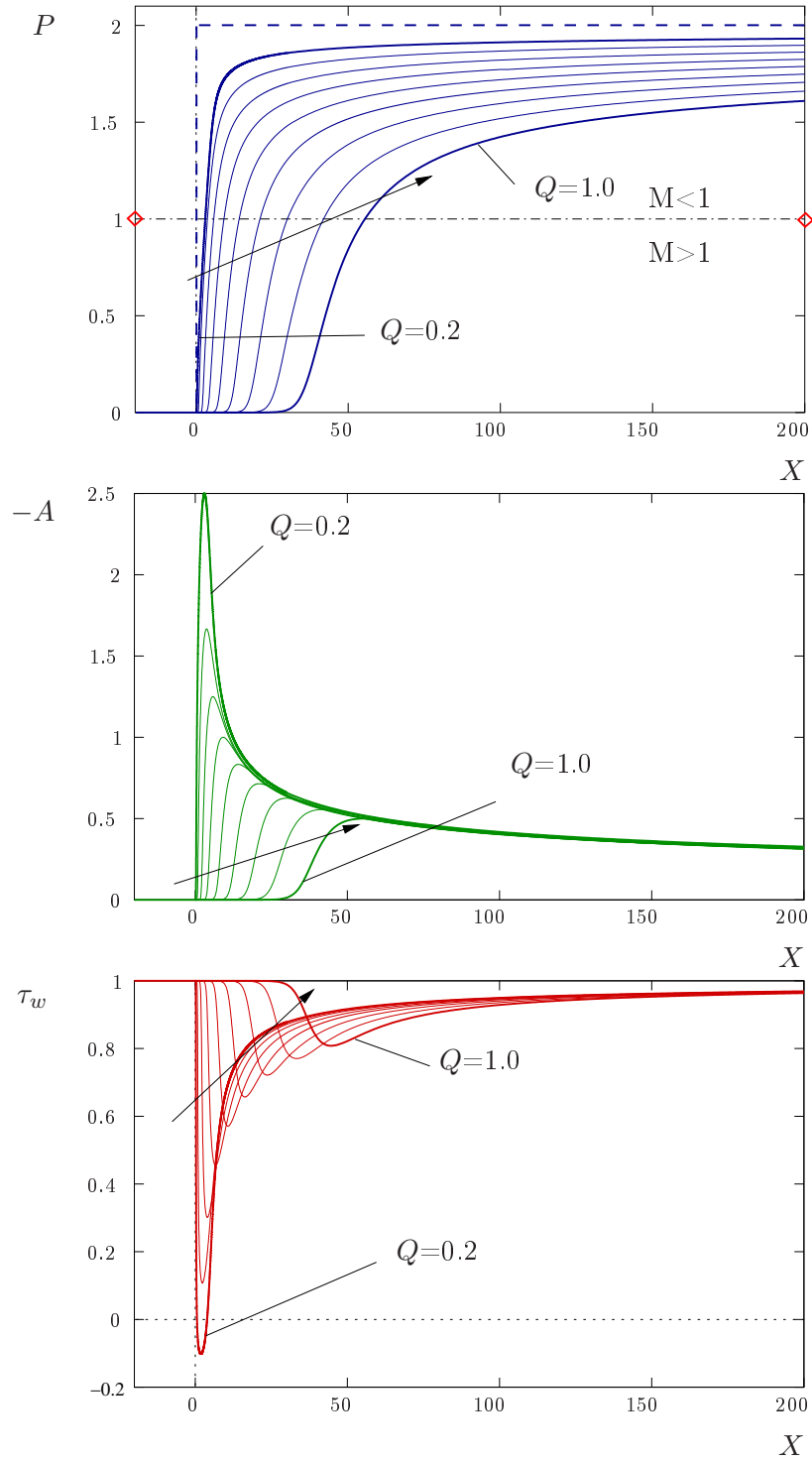
Figure 3.8: Plots of the distribution of the pressure, the displacement thickness and the wall shear stress in an internal shock profile connecting P^b and P^a for various values of Q and $S_{-\infty} = 0$. $Q = 0.2, 0.3, \ldots, 1.0$.

be achieved, e.g., by varying the scaled height of the channel H_{30}, (2.161). By reducing Q, i.e. reducing the strength of the regularizing effect of viscous inviscid interaction, the pressure profile more and more seems to approach the discontinuous solution of a shock, again depicted by the dashed lines in figure 3.8. However, this forces an increasingly stronger reaction of the lower deck flow as is revealed by inspecting the plot of the displacement thickness in figure 3.8. Because of the destabilizing effect of the unfavorable pressure gradient acting in a compressive shock profile, i.e. $\frac{\mathrm{d}P}{\mathrm{d}X} \geq 0$, on the boundary layer flow the minimum of the wall shear stress decreases with increasing steepness of the pressure profile. Finally, the flow starts to separate locally, $\tau_w \leq 0$, the beginning of which is shown in 3.8 for a small region of separation.

3.3.6 Example 2: Rarefaction Shock

As second example the internal profile of a rarefaction shock has been calculated. The selected inflow conditions and scaled quantities are summed up in table 3.3. The chosen inflow pressure and the inflow density are depicted in the pressure vs. density diagram for PP10 shown by figure 3.5. As can be observed the flow conditions lie in the thermodynamic region $\Gamma < 0$, case of negative nonlinearity.

On the left hand side in figure 3.9 the negative perturbation of the mass flux density $G_{[2]}$ vs. the pressure P is shown being strictly concave in the case of negative nonlinearity. Application of the shock admissibility criteria in theorem 3.1.1 indicates that a rarefaction shock is the admissible type of shock for this flow configuration as it leads to a transition from super- to subsonic flow conditions. As before the shock discontinuity in the pressure is sketched to the right in figure 3.9 indicated by the dashed lines. Again,

p_0/p_c	ρ_c/ρ_0	θ_0/θ_c	$\tilde{u}_0$ m/s	$\tilde{\mu}_0$ Pas	K	Γ_0	Re
0.949	1.710	0.997	35.5	$3.00\ 10^{-5}$	< 0	-0.115	$4.36\ 10^8$
ϵ_3	Δ_3	δ_{3l}	δ_{3m}	H_{3u}		$\Gamma_{-\infty}$	Q_1
0.133	0.0235	$2.014\ 10^{-5}$	$1.52\ 10^{-4}$	0.0645		-1.00	24.9

Table 3.3: Selected inflow conditions at channel entry and resulting scaled parameters for the interaction problem. $Q_1 = Q(H_{30} = 1)$.
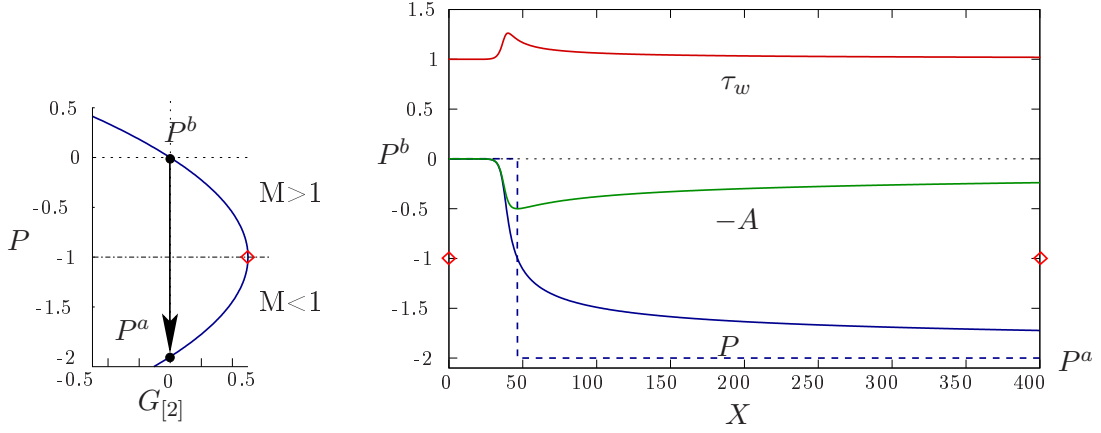
Figure 3.9: To the left, plot of the mass flux density $G_{[2]}$ for quadratic nonlinearity in the pressure and Rayleigh line connecting the pressure before and after the shock, P^b and P^a. To the right, plot of the perturbation of the pressure, displacement thickness and wall shear for $Q = 1$, $S_{-\infty} = 0$.

the shock discontinuity resolves into a smooth internal shock profile if the interacting boundary layers at the wall are taken into account; see the plot of the pressure, displacement thickness and wall shear stress distribution in figure 3.9.

As has been noted in the case of a compression shock, the internal shock profile truly connects the undisturbed flow states up- and downstream of the interaction region represented by P^b and P^a. The internal profile is characterized by exponential behavior far upstream, (3.19), and by weak algebraic behavior far downstream, (3.40) and (3.39).

The influence of the parameter Q on the internal profile is depicted in figure 3.8. Most important of all, it illustrates the stabilizing effect the favorable pressure gradient in an expansive pseudoshock has on the boundary layer flow at the wall. At the beginning, the lower deck flow passing the interaction region is accelerated rather than decelerated as in the classical compressive case treated in the previous section. This leads to a widening of the effective throat area in the supersonic, or in other words to negative values of the disturbance of the displacement thickness $-A$. After the sonic state has been transversed in the upper deck flow regime the lower deck flow decelerates again back to the undisturbed flow profile leading to an successive
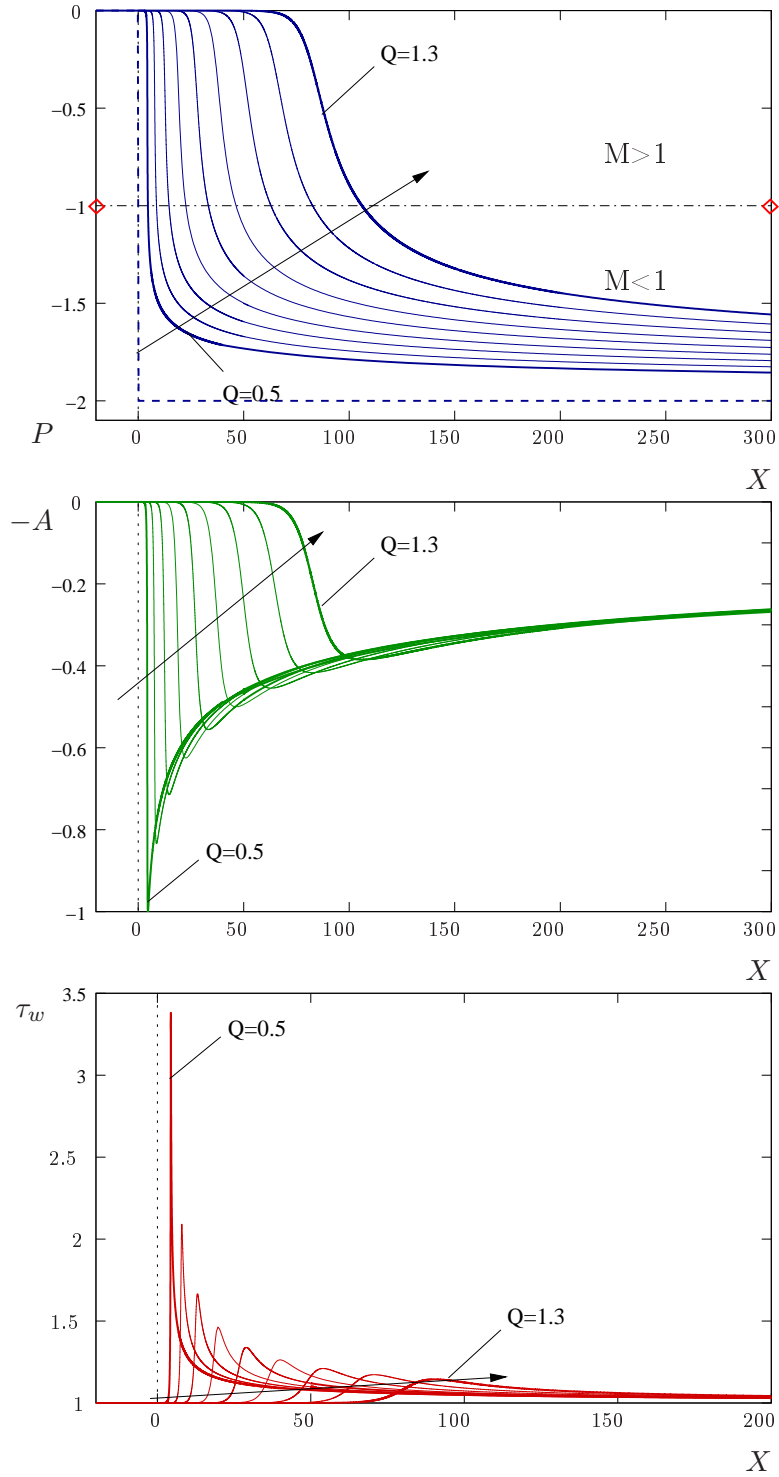
Figure 3.10: Plots of the distribution of the pressure, the displacement thickness and the wall shear stress in an internal shock profile connecting P^b and P^a for various values of Q and $S_{-\infty} = 0$. $Q = 0.5, 0.6, \ldots, 1.3$.
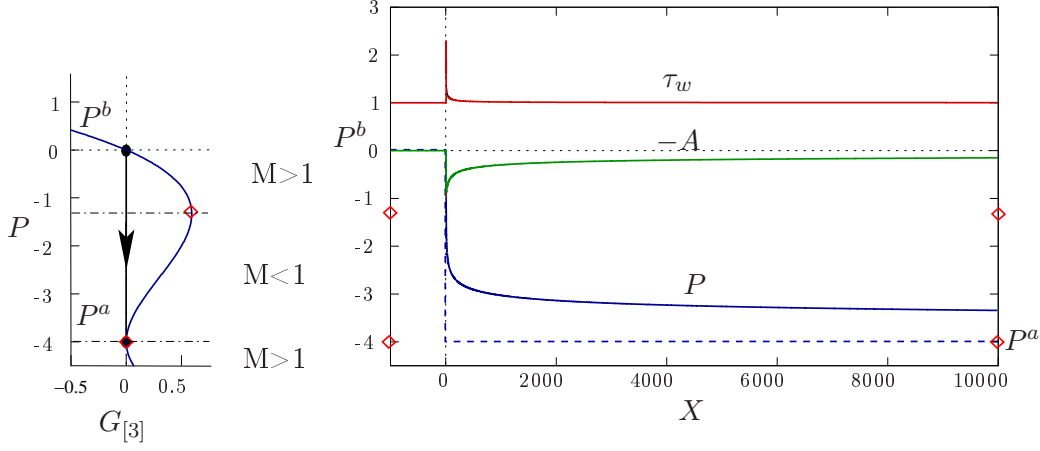
Figure 3.11: To the left, plot of the mass flux density $G_{[3]}$ for cubic nonlinearity in the pressure and Rayleigh line connecting the pressure before and after the shock, P^b and P^a. To the right, plot of the perturbation of the pressure, displacement thickness and wall shear for $Q = 1$, $S_{-\infty} = 0$.

ascent of $-A$. Consequently, the maximum of the wall shear stress increases with increasing steepness of the pressure profile. The wall shear stress itself always is ≥ 1 and thus flow separation is avoided in the entire flow field.

3.3.7   Example 3: Sonic Shock

As third example the internal profile of a rarefying sonic shock has been calculated. The selected inflow conditions and scaled quantities are summed up in table 3.4. The chosen inflow pressure and inflow density are depicted in the pressure vs. density diagram for PP10 in figure 3.5.

On the left hand side in figure 3.11 the negative perturbation of the mass flux density $G_{[3]}$ vs. the pressure P is shown. A sonic shock is only possible in the case of mixed nonlinearity, if Γ changes its sign in the considered

p_0/p_c	ρ_c/ρ_0	θ_0/θ_c	$\tilde{u}_0$ (m/s)	$\tilde{\mu}_0$ (Pas)	K	Γ_0	Λ_0	Re
0.914	1.917	0.994	40.2	2.80 10^{-5}	< 0	-0.0512	-0.918	4.71 10^8
ϵ_3	Δ_3	δ_{3l}	δ_{3m}	H_{3u}		$\Gamma_{-\infty}$	$\Lambda_{-\infty}$	Q_1
0.215	0.00997	9.93 10^{-6}	4.61 10^{-5}	0.0999		-1.00	-0.375	4.48

Table 3.4: Selected inflow conditions at channel entry and resulting scaled parameters for the interaction problem. $Q_1 = Q(H_{30} = 1)$.
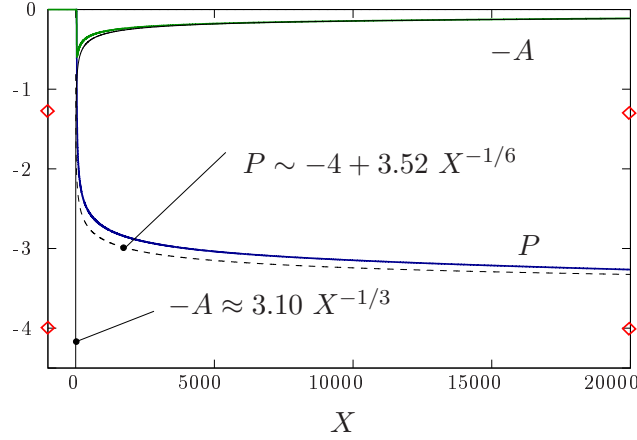
Figure 3.12: Plot of the pressure P and the displacement thickness $-A$ for $Q = 1$, $S_{-\infty} = 0$ and comparison of the asymptotic behavior far downstream $X \gg 1$ predicted by equation (3.39) and (3.41).

flow regime, resulting in a non-convex flux function. The admissible rarefaction shock in the situation under consideration results in a transition from a supersonic flow state to a sonic state, i.e. $M = 1$. As before, the shock discontinuity in the pressure is sketched on the right hand side in figure 3.11 indicated by the dashed lines. And again, the shock discontinuity resolves into a smooth internal shock profile connecting the two states before and after the interaction region characterized by $P^b = 0$ and $P^a = -4$. The influence of the coupling parameter Q on the steepness of the internal shock profiles has already been discussed in the previous section and no new phenomenons enter here. More interesting is the algebraic decay of the pressure in case of a shock terminating in a sonic state, i.e. $G'_{[n]}(P^a) = 0$, which is even weaker than in the case of a shock terminating at a subsonic state, i.e. $G'_{[n]}(P^a) \neq 0$. As in the latter case, see figure 3.7, figure 3.12 shows a reasonable good agreement of the leading order term of the pressure distribution far downstream predicted by theory for a shock ending in a sonic state, equation (3.39) and (3.41), and the numerical results. This weaker algebraic decay results in an increased length of the shock profile as can be seen by comparing e.g. figure 3.7 and 3.12.

Alternatively to a shock connecting supersonic flow upstream with sonic

flow downstream considered so far, a sonic shock can equally well connect sonic flow upstream with subsonic flow downstream in accordance with the shock admissibility criteria theorem 3.1.1 since the condition $[M] < 0$ is satisfied in the latter case just as well. Evaluation of the exponent (3.24) governing the exponential growth of the flow quantities far upstream, (3.19), results in $\kappa = 0$ because of $G'_{[3]}(P^b) = 0$ meaning that the Ansatz of Lighthill yields the trivial eigensolution in this case. On the other hand, there always exists a nontrivial eigensolution for each supersonic flow state upstream no matter how close it is to the sonic flow state. Consequently, the internal shock profile of a sonic shock originating in a sonic flow can be seen as the limiting case of internal shock profiles originating in supersonic flow when $M^b \to 1^+$. This will be used and shown in the next section dealing with the internal shock profile of a double sonic shock.

3.3.8 Example 4: Double Sonic Shock

As fourth example the internal profile of a double sonic shock has been calculated. The selected inflow conditions and scaled quantities are summed up in table 3.5. The chosen inflow pressure and the inflow density are depicted in the pressure vs. density diagram for PP10 in figure 3.5.

On the left hand side in figure 3.3.8 the negative perturbation of the mass flux density $G_{[4]}$ vs. the pressure P is shown. Similar to the case of a simple sonic shock a double sonic shock is only possible in the case of mixed nonlinearity, if Γ changes its sign in the considered flow regime, resulting in a non-convex flux function. For the existence of a simple sonic shock a single change of the sign of Γ in the flow region is sufficient. However, a double sonic shock in principle can only exist if Γ changes sing twice resulting in

p_0/p_c	ρ_c/ρ_0	θ_0/θ_c	$\tilde{u}_0$ (m/s)	$\tilde{\mu}_0$ (Pas)	K	Γ_0	Λ_0	N_0	Re
0.942	1.850	1.00023	40.1	$2.87\ 10^{-5}$	< 0	0.0134	-0.455	6.48	$4.75\ 10^8$
ϵ_3	Δ_3	δ_{3l}	δ_{3m}	H_{3u}		$\Gamma_{-\infty}$	$\Lambda_{-\infty}$	$N_{-\infty}$	Q_1
0.264	0.0184	$1.21\ 10^{-5}$	$4.59\ 10^{-5}$	0.514		-1.00	-0.434	0.0761	7.08

Table 3.5: Selected inflow conditions at channel entry and resulting scaled parameters for the interaction problem. $Q_1 = Q(H_{30} = 1)$.
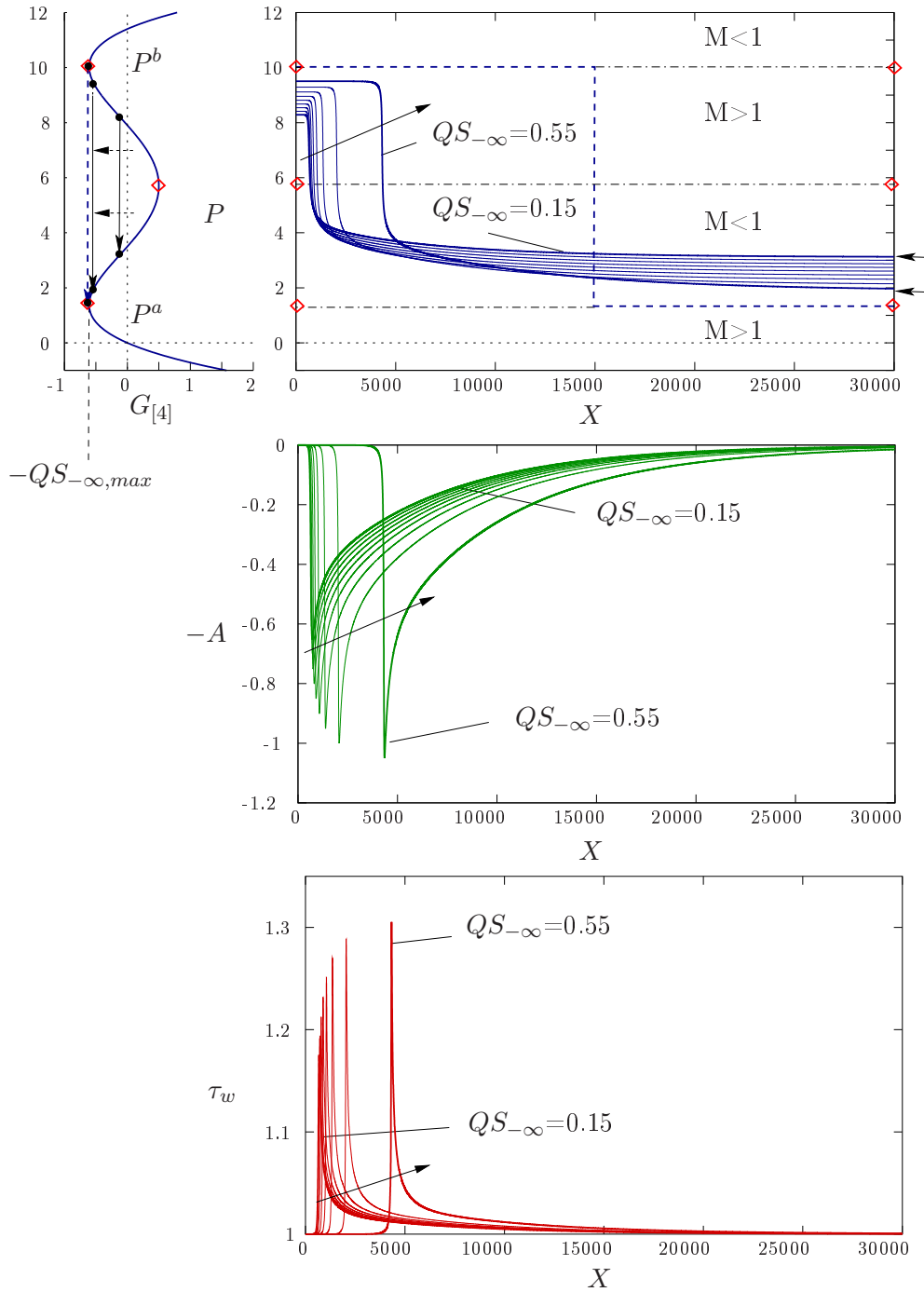
Figure 3.13: To the left, plot of pressure P vs. the mass flux density $G_{[4]}$. The Rayleigh lines are shifted from right to left by varying $QS_{-\infty}$ successively approaching the limiting case of a double sonic shock for $QS_{-\infty,max}$ indicated by the dashed Rayleigh line. To the right, plots of the perturbation of the pressure, displacement thickness and wall shear stress for $Q = 1$, $QS_{-\infty} = 0.15, 0.20, \ldots, 0.55$. In the plot of the pressure a double sonic shock for the inviscid case indicated by the dashed lines is sketched for illustration.

a mass flux density which is represented by a polynomial of fourth order
in the pressure, i.e. $n = 4$. Consulting figure 3.5, the double sonic shock
originates in a thermodynamic region in the pressure vs. density diagram
close to the point where an insentrope touches the transition line $\Gamma = 0$.
Since the second derivative of Γ, i.e. N, has to be positive in the region
of interest, cf. e.g. [35], the flux function $G_{[4]}$ always takes a shape similar
to the example depicted in figure 3.3.8 in the sense that $G_{[4]}(P) \rightarrow +\infty$
for $P \rightarrow \pm\infty$, see equation (2.2.2). As has been discussed in the previous
section, an eigensolution representing the internal shock profile degenerates
to the trivial eigensolution if the shock originates at sonic flow conditions.
Still, the internal shock profile is the limiting case for the internal shock
profiles originating in supersonic flow when $M^b \rightarrow 1^+$ for which nontrivial
eigensolutions exist no matter how close the flow conditions upstream are
to a sonic flow state. This fact has been used in figure 3.3.8. Again, the
double sonic shock is sketched by the dashed lines in the plot of the pressure
distribution to the right. The flow conditions upstream of the interaction
region are adjusted by varying the parameter $QS_{-\infty}$ in the interaction law
and thus shifting the Rayleigh lines from right to left by a distance $-QS_{-\infty}$
from the origin, see left hand side of figure 3.3.8. The limiting case of a
double sonic shock would be obtained for $QS_{-\infty} = QS_{-\infty,max}$, see figure
3.3.8. Prescribing a value $QS_{-\infty} \neq 0$ is identical to changing the height
of the channel and the inflow conditions according to the way described in
section 3.2; see figure 3.2 in particular.

Considering the various Rayleigh lines in figure 3.3.8 it is evident that
the overall shock strength increases whilst approaching the limiting double
sonic shock. On the other hand, considering the plot of the internal pressure
profiles, the length of a shock profile, i.e. the region of significant variation of
the pressure, is increasing accordingly. Taking a look at the formulas for the
asymptotic behavior far up- and downstream immediately reveals that both
the exponent in (3.19) and the coefficient in (3.40) are becoming successively
smaller for $M^b \rightarrow 1^+$, i.e. $G'_{[n]} \rightarrow 0^-$ and thus explaining the increasing
length of the internal shock profiles. This phenomenon of increasing shock
length for increasing shock strength already has been reported in a different

context by Cramer & Crickenberger, [18], who studied internal shock profiles resulting from a classical thermo-viscous regularization.

Moreover, an admissible double sonic shock is bound to be a rarefaction shock in accordance with the shock admissibility criteria for the inviscid case, theorem 3.1.1. This can be concluded from inspection of figure 3.3.8 and by additionally considering the arguments about the possible shapes of a flux function $G_{[4]}$ addressed in the beginning of this section. A double sonic shock has to connect two separate extrema of of $G_{[4]}$ and, since $G_{[4]} \to \infty$ for $P \to \pm\infty$ because of $N > 0$, these two extrema have to be minima. The remaining extremum of $G_{[4]}$ is a maximum and has to lie in-between. Let $P_{min}^1 > P_{min}^2$ characterize the two separate minima and P_{max} the maximum. Then $G'_{[4]} < 0$ for $P \in \{P_{min}^1, P_{max}\}$ and $G'_{[4]} > 0$ for $P \in \{P_{max}, P_{min}^2\}$ and, consequently, the internal shock profiles used to construct the limiting solution of a double sonic shock can correspond to rarefaction shocks only and thus a double sonic shock likewise has to be a rarefaction shock.

3.3.9 Example 5: Split Shock

As fifth and last example the internal profile of a split shock has been calculated. The selected inflow conditions and scaled quantities are summed up in table 3.6. The chosen inflow pressure and the inflow density density are depicted in the pressure vs. density diagram for PP10 in figure 3.5.

On the left hand side in figure 3.3.9 the negative perturbation of the mass flux density $G_{[4]}$ vs. the pressure P is shown. similar to the case of a double sonic shock a split shock is possible only in the case of mixed nonlinearity where Γ changes its sign twice in the considered flow regime, i.e. $n = 4$, resulting in a non-convex flux function which is represented by a polynomial

p_0/p_c	ρ_c/ρ_0	θ_0/θ_c	$\tilde{u}_0$ (m/s)	$\tilde{\mu}_0$ (Pas)	K	Γ_0	Λ_0	N_0	Re
0.945	1.84	1.00042	39.8	$2.88 \ 10^{-5}$	< 0	0.0110	-0.407	6.90	$4.72 \ 10^8$
ϵ_3	Δ_3	δ_{3l}	δ_{3m}	H_{3u}		$\Gamma_{-\infty}$	$\Lambda_{-\infty}$	$N_{-\infty}$	Q_1
0.264	0.0184	$1.21 \ 10^{-5}$	$4.59 \ 10^{-5}$	0.514		-1.00	-0.563	0.141	6.44

Table 3.6: Selected inflow conditions at channel entry and resulting scaled parameters for the interaction problem. $Q_1 = Q(H_{30} = 1)$.
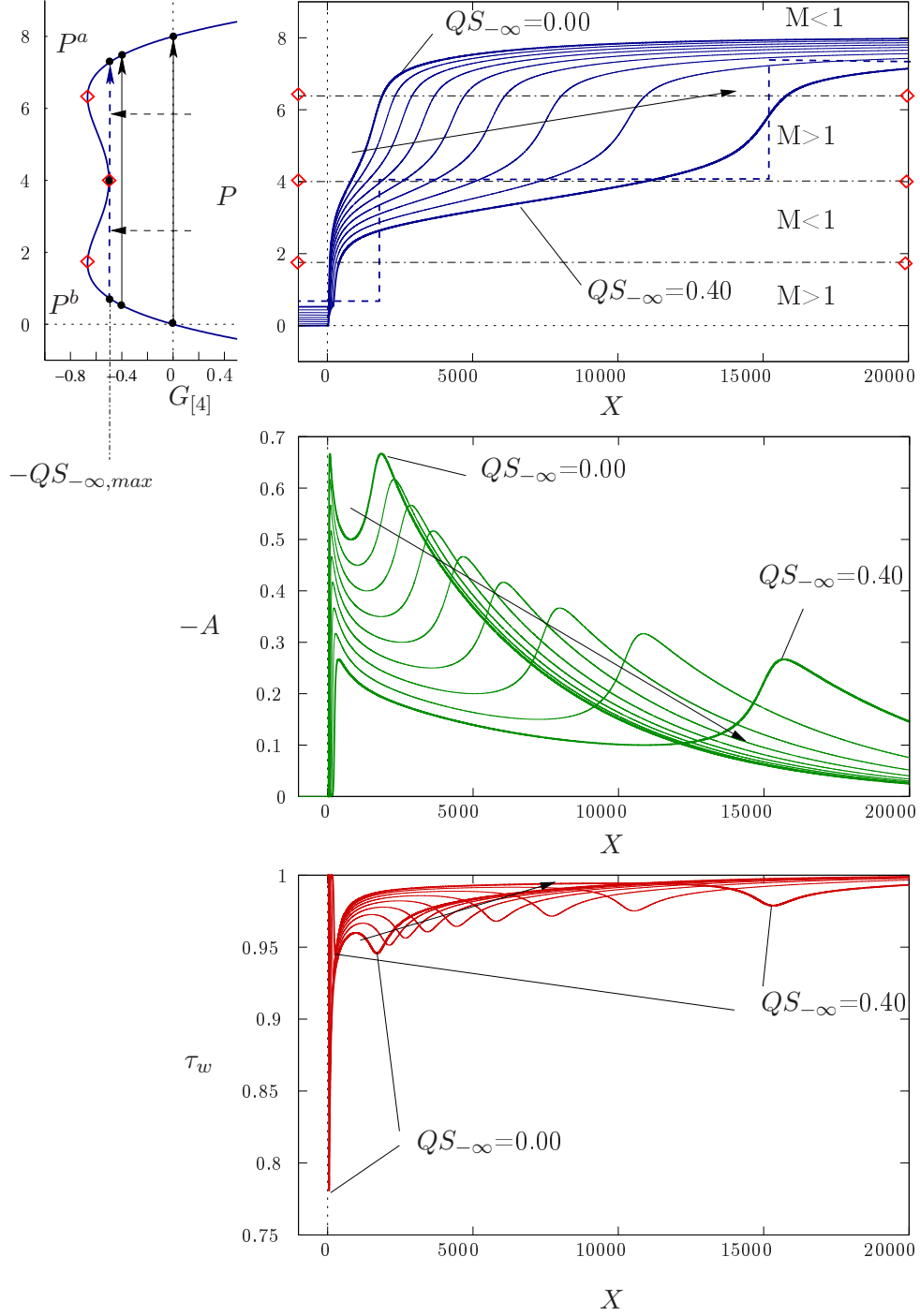
Figure 3.14: To the left, plot of pressure P vs. the mass flux density $G_{[4]}$. The Rayleigh lines are shifted from right to left by varying $QS_{-\infty}$ successively approaching the limiting case of a split shock for $QS_{-\infty,max}$ indicated by the dashed Rayleigh line. To the right, plots of the perturbation of the pressure, displacement thickness and wall shear stress for $Q = 1$, $QS_{-\infty} = 0.00, 0.05, \ldots, 0.40$. In the plot of the pressure a split shock for the inviscid case indicated by the dashed lines is sketched for illustration.

of fourth order in the pressure. The Rayleigh line of the split shock is given by the dashed line which touches the flux function $G_{[4]}$ at a sonic point at the distance $QS_{-\infty,max}$ from the origin. Again, the split shock can be interpreted as the limiting case for simple shocks for $QS_{-\infty} \to QS_{-\infty,max}$. The flow in the upper deck region has to pass through three sonic sates, see figure 3.3.9, while the overall shock leads to a transition from super- to subsonic conditions. The three sonic states result in three extrema in the distribution of the disturbance of the displacement thickness $-A$. The lower deck flow generates a viscous Laval nozzle which consists of two throats and one anti-throat in order to allow a smooth acceleration of the upper deck flow through the different Mach number regimes. Taking a look at the calculated pressure distribution of internal shock profiles for various values of $QS_{-\infty}$ on the right hand side in figure 3.3.9 reveals that the shock splitting can already be anticipated in the pressure profiles for vales of $QS_{-\infty} < QS_{-\infty,max}$. After the upper deck flow has passed through the first sonic state resulting in a passage from super- to subsonic flow, the pressure enters a plateau region while passing the second sonic state as the the flow is accelerated from sub- to supersonic again. Finally, the then supersonic flow passes the third sonic state and the flow becomes subsonic again. The last transition from supersonic to subsonic conditions results in a second steepening of the shock profile. This phenomenon of impending shock splitting becomes more and more pronounced successively separating the two regions of largest ascent in the pressure profile for $QS_{-\infty} \to QS_{-\infty,max}$. The existence of an internal shock profile infers that indeed two shocks forming a split shock may coexist next to each other in purely inviscid flow throughout this limited thermodynamic region as predicted by the shock admissibility criteria . Interestingly enough, similar to the case of a double sonic shock discussed before, this phenomenon of impending shock splitting has also been observed first by Cramer & Crickenberger, [18], for internal shock profiles resulting from a thermo-viscous regularization.

Chapter 4

Viscous Laval Nozzle

The flow field resulting form viscous inviscid interactions generated by the presence of a small surface mounted hump within the transonic flow field in a slender channel, cf. figure 4.1, will be discussed. Considering the centerline symmetry of the problem this surface mounted hump in fact forms a small nozzle. The viscous inviscid interactions shall be described by the problem previously formulated in definition 2.2.1, i.e. the dimensions of the channel and the surface mounted hump shall be consistent with the length scales proposed in the formulation of the distinguished limit for this Re number regime, cf. section 2.2, and the inviscid flow in the upper deck of the interaction region is one-dimensional to the leading order.

Section 4.2 will discuss the influence of the interaction between the steady flow field developing in the core region of such slender nozzles and the viscous boundary layers at the walls highlighting the similarities and differences to purely inviscid one-dimensional theory of Laval nozzles. In the major part of this chapter the working media will be considered to be perfect gas like, i.e. $\Gamma > 1$. The conversion of subsonic flow to supersonic flow by means of Laval nozzles is of importance in technical applications and taking into account the trend towards miniaturization the presented solutions will give a qualitative description of phenomena expected to be encountered in such flow devices where the influence of the viscous boundary layers at the walls on the inviscid flow in the core region no longer can be considered to be an effect of higher
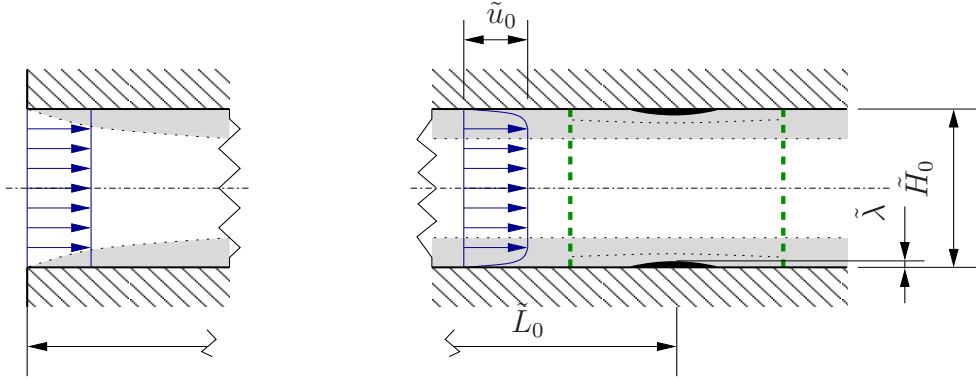
Figure 4.1: Small surface mounted hump of height $\tilde{\lambda}$ in a slender channel.

order as it would be the case in classical hierarchical boundary layer theory.

Incidentally, an operating mode close to choking conditions, that is close to flow conditions for which no stationary solutions exist, will be identified for such slender nozzles connected with the appearance of pseudo-normal shocks, cf. e.g. [54], in the diffuser part of the nozzle. These pseudo-normal shocks are representing regularized versions of weak normal shocks known from purely inviscid Laval nozzle theory. If the strength of such a pseudo-shock is sufficiently large, then the boundary layer flow at the walls is bound to separate. It is known from observations that such shock induced flow separation in transonic diffusers frequently is connected with the occurrence of self sustained shock oscillations, [7], [27], [54], [55], [66], [60], [93]. The problem of viscous inviscid interactions in slender channels stated in definition 2.2.1 poses a simplified model capable of describing the essential features to be expected at the basis of the occurrence of shock oscillations, namely the interaction of the (pseudo-) shock and the separated flow in the wall attached boundary layer. The reaction of an initially steady interacting nearly choked flow field in a slender nozzle to unsteady disturbances will be investigated in section 4.3. Following [54] the transonic diffuser flow can be classified into three types with respect to shock oscillations: no separation flow, shock-induced flow (the separation being triggered at the shock root) and pressure-gradient-induced separation flow. The first case will be discussed in section 4.3.2 and the second in section 4.3.3. The third one will not be covered in the scope of this treatise.

4.1 Numerical Method

4.1.1 Stationary Problem

The fundamental lower deck problem equations (2.207) to (2.213) and the interaction law (2.214) in definition 2.2.1 are discretized by means of finite differences of second order. In the next step, the resulting system of d algebraic equations

$$\mathbf{F(s)} = \mathbf{0} \qquad \mathbf{F}, \mathbf{s} \in \mathbb{R}^d \qquad (4.1)$$

with $\mathbf{s}$ the d-dimensional solution vector is solved by a variant of the Powell Hybrid algorithm, e.g. [63], which has been adapted and used by R. Szeywerth for the numerical treatment of other triple deck problems, [84]. The sparsity of the Jacobian $\mathrm{D_s F}$ of $\mathbf{F}$ is conveniently exploited by the implementation of the sparse solver routine PARDISO, [70], [68], [69]. To this end, the physical domain $(X, Y) \in \mathbb{R} \times \mathbb{R}^+$ is mapped onto the bounded computational domain $(\xi, \eta) \in [-1, 1] \times [0, 1/\alpha_s]$. The mapping $\xi \mapsto X(\xi) \in C^1([-1, 1])$ is sought in the form

$$X(\xi) = \begin{cases} X_-(\xi) & -1 \leq \xi < \xi_s^- \\ X_m(\xi) & \xi_s^- \leq \xi \leq \xi_s^+ \\ X_+(\xi) & \xi_s^+ < \xi \leq 1 \end{cases}$$

introducing three functions X_-, X_+ and X_m

$$X_-(\xi) = X_s^- + \frac{X_s^+ - X_s^-}{\xi_s^+ - \xi_s^-} \frac{1 + \xi_s^-}{2m^-} \left(\frac{1}{1 - \left(\frac{\xi - \xi_s^-}{1 + \xi_s^-} \right)^{m^-}} - \frac{1}{1 + \left(\frac{\xi + \xi_s^-}{1 + \xi_s^-} \right)^{m^-}} \right),$$

$$X_m(\xi) = X_s^- + \frac{X_s^+ - X_s^-}{\xi_s^+ - \xi_s^-} (\xi - \xi_s^-),$$

$$X_+(\xi) = X_s^+ + \frac{X_s^+ - X_s^-}{\xi_s^+ - \xi_s^-} \frac{1 - \xi_s^+}{2m^+} \left(\frac{1}{1 - \left(\frac{\xi - \xi_s^+}{1 - \xi_s^+} \right)^{m^+}} - \frac{1}{1 + \left(\frac{\xi + \xi_s^+}{1 - \xi_s^+} \right)^{m^+}} \right).$$

The parameters m^+ and m^- are chosen to account for the far up- and down-
stream behavior of the numerical solution. Most important of all, X_m is a
linear mapping of an interior region $[X_s^-, X_s^+]$ of the physical domain onto an
interior region $[\xi_s^-, \xi_s^+]$ of the computational domain. The complicated form
of X_- and X_+ originates from the fact that $X(\xi) \in C^1([-1, 1])$ which results
in the requirements $X'_-((\xi_s^-)-) = X'_m((\xi_s^-)+)$ and $X'_m((\xi_s^+)-) = X'_+((\xi_s^+)+)$.
The map $\eta \mapsto Y(\eta) \in C^1([0, 1/\alpha_s])$ is sought in the form of

$$Y(\eta) = Y_s \left(\frac{1}{1 - \alpha_s \eta} - \frac{1}{1 + \alpha_s \eta} \right),$$

where the parameters Y_s and α_s are chosen to properly account for the be-
havior of the solution in Y-direction. The representation of the uniform
numerical grid in the new coordinates (ξ, η) is introduced

$$(\xi_i, \eta_j) = (-1 + i\Delta\xi, j\Delta\eta) \quad i = 0 \ldots N_i, \; j = 0, \ldots N_j - 1$$

where the step size in ξ-direction and in η direction are given by $\Delta\xi = 2/N_i$
and $\Delta\eta = 1/N_j$ respectively. For the numerical treatment of the fundamental
problem the transformation $\bar{U} = U - Y$ is introduced and V in the momentum
equation (2.208) is expressed by means of the continuity equation (2.207)

$$V = -\int_0^Y \frac{\partial \bar{U}}{\partial X}(X, \bar{Y})\mathrm{d}\bar{Y} = -\int_0^\eta \frac{1}{X'(\xi)} \frac{\partial \bar{U}}{\partial \xi}(\xi, \bar{\eta})Y'(\bar{\eta})\mathrm{d}\bar{\eta}. \qquad (4.2)$$

The derivatives in ξ-direction are resolved by means of a Cranck-Nicholson
discretization, i.e. $\partial \bullet /\partial\xi \approx (\bullet_{i,j} - \bullet_{i-1,j})/\Delta\xi$, if $U_{i,j} = Y_{i,j} + \bar{U}_{i,j} > 0$,
and by means of backward finite differences of second order, i.e. $\partial \bullet /\partial\xi \approx$
$(3 \bullet_{i,j} - 4 \bullet_{i-1,j} + \bullet_{i-2,j})/2\Delta\xi$ in regions of separated flow, i.e. $U_{i,j} = Y_{i,j} +$
$\bar{U}_{i,j} < 0$. Numerical experiments showed that the discretization based on a
Cranck-Nicholson approach is superior to a discretization based on backward
differences in regions without flow separation, also in the light of a reduced
computational main memory consumption. However, it has been found that
the Cranck-Nicholson discretization is not always sufficient in regions of larger
flow separation indicated by the occurrence of numerical oscillations. It shall

be mentioned that the initial strategy of formulating the problem by means of the stream function has been abandoned in favor of the described procedure because of the observed numerical problems in regions of flow separation. For the discretization of derivatives in η-direction central differences evaluated at the grid point η_j are used and for the evaluation of the integral in (4.2) the trapezium rule is applied. The matching condition (2.213) is implemented as $A = \bar{U}(X, Y_{max} = Y(1))$. This is justified because of the exponential decay of $\bar{U}$ for $Y \gg 1$ which one infers by inspection of the asymptotic representation of the stream function Ψ for $Y \gg 1$, $\forall X$, see the discussion following equation (3.33). The no slip condition at the wall requires $\bar{U}_{i,0} = 0$ for $i = 0, \ldots, N_i$ and the matching with the undisturbed boundary layer upstreams results in the conditions $\bar{U}_{0,j} = 0$ for $j = 0, \ldots, N_j - 1$.

The discretization of the interaction law for steady upper deck flow, i.e. $\partial P / \partial T \equiv 0$, relies on the formulation in differential form (2.214) and not on the integrated form (3.18), since the formulation (2.214) will be used in the numerical adaption of a linear stability analysis undertaken for selected solutions to the stationary problem in section 4.3.3. Equation (2.214) is rewritten as

$$\frac{\mathrm{d}}{\mathrm{d}X} \left(G_{[n]}(P) - Q(A - S) \right) = \frac{1}{X'(\xi)} \frac{\mathrm{d}}{\mathrm{d}\xi} \left(G_{[n]}(P) - Q(A - S) \right) = 0 \quad (4.3)$$

and afterwards approximated by $\mathcal{G}_i = 0 \quad \forall i$ with

$$\mathcal{G}_i := \begin{cases} \frac{1}{X'_i} \frac{(G_{[n]}(P_{i+1}) - Q(A_{i+1} - S_{i+1})) - (G_{[n]}(P_{i-1}) - Q(A_{i-1} - S_{i-1}))}{2\Delta\xi} & i = 1, \ldots, N_i - 1 \\ \frac{1}{X'_{i-1/2}} \frac{(G_{[n]}(P_i) - Q(A_i - S_i)) - (G_{[n]}(P_{i-1}) - Q(A_{i-1} - S_{i-1}))}{\Delta\xi} & i = N_i \end{cases}$$

$$(4.4)$$

where $X'_{i-1/2} = X'(-1 + (i - 1/2)\Delta\xi)$.

For the numerical results presented in this chapter -unless otherwise stated- the number of grid points in ξ- and η-direction are $N_i = 1400$ and $N_j = 100$ respectively, $\xi_s^- = 100/N_i$, $\xi_s^+ = 1100/N_i$, $m^- = m^+ = 1.3$, $X_s^- = -3$, $X_s^+ = 3$, $Y_s = 0.2$, $\alpha_s = 0.98$, $Y_{max} \approx 9.9$.

4.1.2   Unsteady Problem

It is important to note that the numerical scheme for the interaction law in unsteady form, (2.214), is developed having in mind a strictly convex or concave function $G_{[n]}$, i.e. $n = 2$. To this end, a method of line, [71], is used for the discretization of the partial differential equation. In the first step the discretization scheme for the spatial coordinate which has been described in the previous section, equations (4.3) and (4.4), and which is of second order in space is applied to the expression $\frac{\partial}{\partial X}\left(G_{[n]}(P) - Q(A - S)\right)$ in equation (2.214) yielding the following system

$$\frac{\partial P_i}{\partial T} = \mathcal{G}_i(T) \qquad i = 1, \ldots, N_i \qquad (4.5)$$

of N_i ordinary equations. The time-integration from $T_n = n\Delta T$ to $T_{n+1} = (n + 1)\Delta T$ of the obtained system of ODEs with the known solution at T_n as initial condition then is performed by means of the TR-BDF2 method, cf. [31], [50], an one-step two staged method being of second order in time. The TR-BDF2 method is L-stable, cf. [31], and has been developed for the time integration of a numerically stiff system of ODEs. That such a stiff time integration is necessary has been indicated by preliminary numerical experiments performed with a numerical scheme based on an implicit Lax-Wendroff scheme. The idea behind an implicit Lax-Wendroff scheme has been to think of the interaction law (2.214) as to be consisting of a "hyperbolic part" or "kinetic wave equation part", i.e. $-\frac{\partial P}{\partial T} + \frac{\partial}{\partial X}G_{[n]}(P)$, and a "source term" $\frac{\partial}{\partial X}Q\left(A - S\right)$. Using the Lax-Wendroff approach in order to derive the numerical scheme for equation (2.214), [50], one finally obtains a scheme of second order which can be written in the form of the classical implicit Lax-Wendroff scheme for the "hyperbolic part" extended by the numerical representation of the "source term". The numerical results, however, indicate that disturbances calculated by this method are traveling at wrong finite speeds despite the effort to use a conservative formulation for the hyperbolic part of the interaction law in the first place, cf. the discussion of the linearized problem in section 4.3.1 as well as cf. figure 4.8(a). This phenomenon is well known in the literature dealing with conservative numerical schemes for

hyperbolic PDEs with source terms, cf. [48] and [50], hinting that the source term is stiff indeed.

The first stage of the TR-BDF2 method consists out of the trapezoidal step

$$P_i^{n+\tau} - P_i^n = \tfrac{1}{2}\tau\Delta T\left(G_i^n + G_i^{n+\tau}\right) \qquad i = 1, \ldots, N_i \qquad (4.6)$$

where the superscripts n and $n + \tau$ has the meaning evaluated at the time $n\Delta T$ and $(n+\tau)\Delta T$, respectively. ΔT is the chosen time step which is kept fixed throughout the calculations. In general $\tau \in (0, 1)$ but in order to obtain the property of L-stability for the overall time-integration τ has to be chosen $\tau = 2 - \sqrt{2}$, cf. [31]. The governing equations, cf. (2.207) to (2.213), for the quasi-steady lower deck problem for the time $T_{n+\tau}$ have to be solved as a side-condition

$$\mathbb{R}^{d-N_i} \ni \mathbf{F}_{LD}(\mathbf{s}^{n+\tau}) = 0 \qquad \mathbf{s}^{n+\tau} \in \mathbb{R}^d \qquad (4.7)$$

for equations (4.6) where the system of algebraic equations given by $\mathbf{F}_{LD}$ is obtained by straightforward application of the finite-difference scheme developed for the steady lower deck problem, see previous section. Together with the N_i algebraic equations from (4.6) this results in a system of d algebraic equations for d unknowns. In the second stage of the TR-BDF2 scheme backward differences of second order are used for the time discretization of (4.5) making use of the "old" solutions at the time T_n and the intermediate time $T_{n+\tau}$ yielding

$$\tau(2 - \tau)P_i^{n+1} - P_i^{n+\tau} + (1 - \tau)^2 P_i^n = \tau(1 - \tau)\Delta T\mathcal{G}_i^{n+1} \qquad i = 1, \ldots, N_i.$$
$$(4.8)$$

The system of equations (4.8) again is solved together with

$$\mathbb{R}^{d-N_i} \ni \mathbf{F}_{LD}(\mathbf{s}^{n+1}) = 0 \qquad \mathbf{s}^{n+1} \in \mathbb{R}^d \qquad (4.9)$$

from which the solution at the "new" time T_{n+1} is obtained.

Finally, it shall be noted that the TR-BDF2 scheme can be rewritten in the form of a conservative finite-volume scheme despite the fact that it originally has been derived by a method of lines and finite differences.

4.1.3   Numerical Homotopy Method

In general, the problem under consideration will depend on several parameters. In the following only one of these shall be essential to the problem, i.e. the height λ of a surface mounted obstacle, while the others are kept fixed. Consequently the numerical scheme and the resulting system of algebraic equations (4.1) will depend on λ as well, i.e. $\mathbf{F}(\mathbf{s}; \lambda) = \mathbf{0}$. If the height of the surface mounted obstacle is small, then the trivial solution of the interaction problem $\bar{U} \equiv V \equiv 0$ will be a good initial guess for the numerical equation solver used and convergence is indeed obtained after several steps. For larger λ no convergence can be obtained, therefore a numerical homotopy strategy, cf. e.g. [76], [82], is adopted. The sought after solution $\mathbf{s}_k$ of $\mathbf{F}(\mathbf{s}; \lambda_k) = 0$ is considered to be part of a family of solutions $\mathbf{s}(\lambda)$ of $\mathbf{F}(\mathbf{s}; \lambda) = 0$. If the solutions of two neighboring problems $\mathbf{F}(\mathbf{s}; \lambda_{i-1}) = 0$ and $\mathbf{F}(\mathbf{s}; \lambda_i) = 0$ are known an initial guess $\mathbf{s}_{i+1,est}$ for the solution of $\mathbf{F}(\mathbf{s}; \lambda_{i+1}) = 0$ can be constructed by tangential updating, see figure 4.2(a). If the constructed initial guess is good enough to obtain a new solution for λ_{i+1} the described updating procedure can be used to obtain a solution for λ_{i+2} and so forth until λ_k is reached. One shortcoming of this method is that it fails if a turning point is encountered as has been depicted in figure 4.2(a) or if the solution is very sensitive to variations of the parameter, i.e. even a small variation of λ leads to a large change in the solution. Therefore, the parameter λ is considered to be a variable itself and thus part of the solution . The system of equations $\mathbf{F}(\mathbf{s}, \lambda) = 0$ has to be supplemented by an additional equation $f(\mathbf{s}, \lambda) = 0$ in order to close the problem. The new problem

$$\mathbb{R}^{d+1} \ni \bar{F}(\bar{\mathbf{s}}) = \bar{F}((\mathbf{s}, \lambda)^T) = \begin{cases} \mathbf{F}(\mathbf{s}, \lambda) = \mathbf{0} \\ f(\mathbf{s}, \lambda) = 0 \end{cases} \tag{4.10}$$

can be solved in the manner previously described. The phase condition $f(\mathbf{s}, \lambda) = 0$ is chosen as

$$f(\mathbf{s}, \lambda) = \|(\mathbf{s} - \mathbf{s_i}, \lambda - \lambda_i)\| - \Delta\lambda_i = 0 \qquad (4.11)$$

meaning that the distance in the phase space $\Delta\lambda_i$ between the new solution $\bar{\mathbf{s}}_{i+1}$ and the old solution $\bar{\mathbf{s}}_i$ is prescribed, compare figure 4.2(b). $\Delta\lambda_i$ is chosen according to the method of Seydel

$$\Delta\lambda_i = \Delta\lambda_{i-1} \min(2, \tfrac{iter_{op}}{iter})$$

with *iter* and *iter$_{op}$* the number of the iterations used to obtain the previous solution and some preset optimal number of iterations respectively.
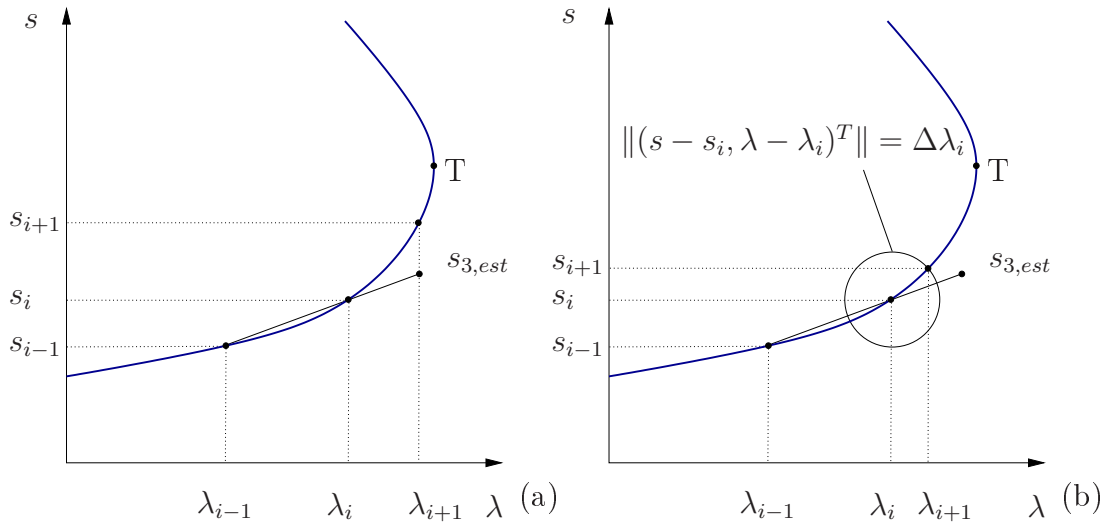

Figure 4.2: Schematic sketch of numerical homotopy method. (a) Homotopy method with prescribed fixed new parameter value λ_{i+1}. (b) Homotopy continuation method. New parameter value λ_{i+1} is part of the solution. $s_{i+1,est}$ initial guess constructed by tangential updating, T turning point.

4.2   Steady Flow in "Viscous" Laval Nozzles

The subsonic near critical flow regime in a slender channel is affected by means of a small surface mounted hump given by the relation, already written

in lower deck scalings,

$$S(X) = \begin{cases} 0 & 2 < |X| \\ \frac{\lambda}{2}(1 + \cos(\pi X/2)) & |X| \leq 2. \end{cases} \tag{4.12}$$

The surface mounted hump forms a small Laval nozzle consisting of a converging, i.e. $S'(X) > 0$ for $X < 0$, and a diverging part, i.e. $S'(X) < 0$ for $X > 0$, cf. figure 4.1. The flow medium under consideration shall be ideal gas like, i.e. $\Gamma > 1$. The corresponding problem of viscous inviscid interaction stated in definition 2.2.1 for steady flows is solved numerically, cf. section 4.1.1, for different heights λ of the surface mounted hump using the numerical homotopy continuation method described in section 4.1.3. The parameter n governing the nonlinearity of the flux function $G_{[n]}$, (2.215), is taken to be 2, because of the premise of $\Gamma > 1$, and $K > 0$ since the oncoming flow in the core region of the nozzle is subsonic, and Q entering the interaction law is taken to be 1. Consequently, supersonic upper deck flow is encountered for $P < -1$, cf. (2.216). The flow conditions far upstream are given by $P = A = \bar{U} = 0$ for $X \to -\infty$. Evaluation of expression (3.24) immediately reveals that for subsonic oncoming core region flow no nontrivial eigensolutions can exist besides the trivial solution. Hence the presence of the surface mounted hump is not felt upstream of the obstruction, i.e. for $X < -2$. Furthermore, there exist two possible undisturbed flow sates downstream of the interaction region which are consistent with the asymptotic far downstream behavior of the solution of the interaction problem predicted by (3.40) and (3.39). The one given by $P = A = \bar{U} = 0$ which is identical with the oncoming far upstream flow conditions indicates subsonic and the other given by $P = -2$ and $A = \bar{U} = 0$ indicates supersonic flow in the core region of the nozzle downstream of the interaction region. Note that equations (3.40) and (3.39) derived for the asymptotic downstream properties of eigensolutions of the interaction problem also apply to the considered situation since the surface mounted hump vanishes for $|X| \gg 1$, i.e. $S(X) \equiv 0$ for $|X| > 2$.

The numerical results for the perturbation of the pressure P, the part of the negative displacement thickness evoked by the viscous lower deck reaction
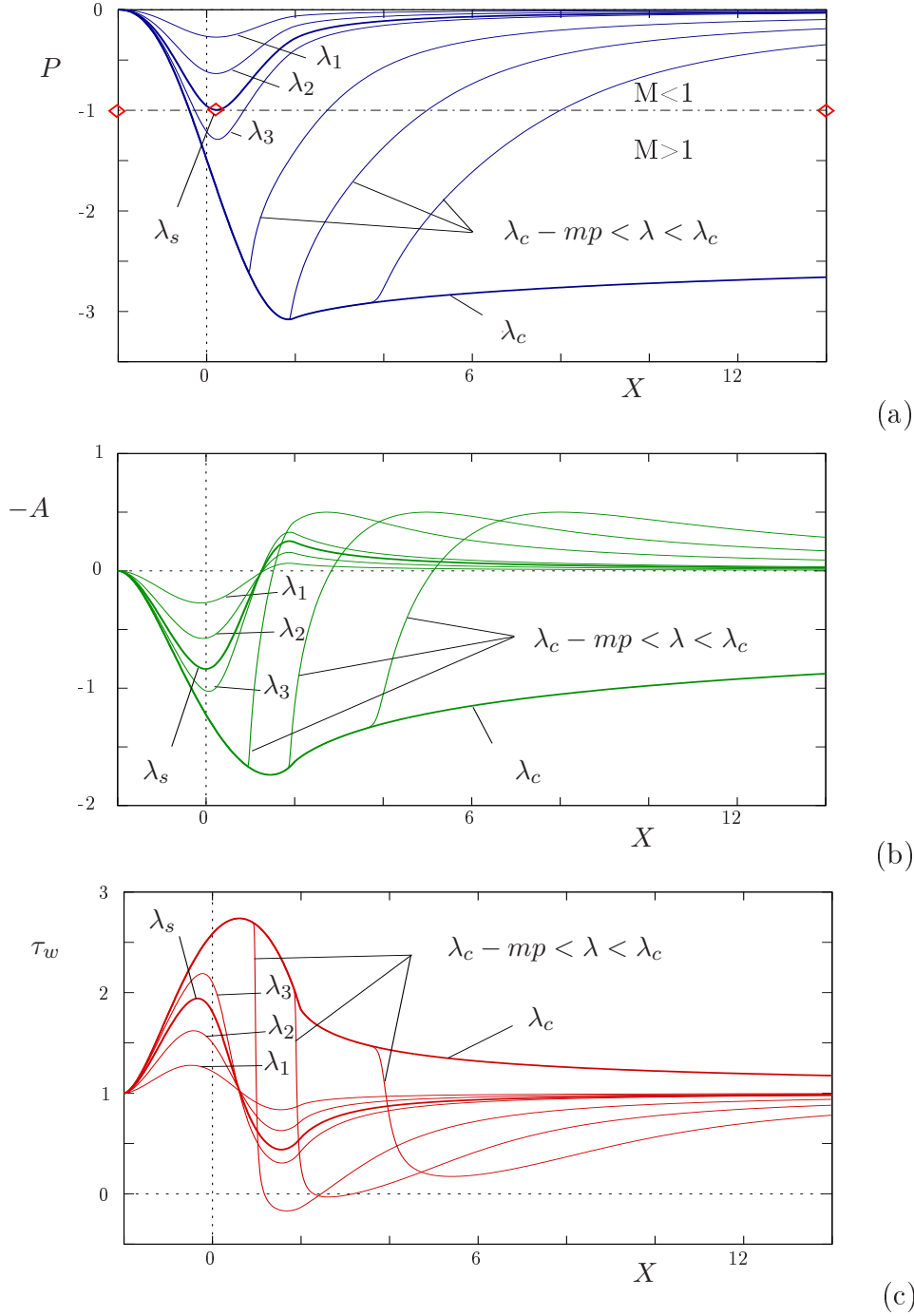
(a)

(b)

(c)

Figure 4.3: Plot of (a) P-, (b) $-A$- and (c) τ_w-distribution for various heights λ of the surface mounted hump . λ_1=0.5, λ_2=1.0, λ_3=1.5. A sonic state, indicated by $\Diamond$, is first encountered for $\lambda_s \approx 1.335$. Transition from sub- to supersonic flow for λ_c=1.60624..., for $\lambda \to \lambda_c-$ pseudo-shocks form leading to a smooth transition from super- to subsonic flow, mp denotes machine precision. For $\lambda > \lambda_c$ there exist no steady solutions. $Q = 1$.

only $-A = -A^\star - S$, see equation (2.206), and the wall shear stress τ_w are shown in figure 4.3. For small heights of the surface mounted hump, cf. the distribution of the pressure for λ_1 and λ_2 in figure 4.3(a), the upper deck flow remains subsonic in the whole interaction region very much alike as in the classical case of inviscid one-dimensional flow of a perfect gas like medium in a Laval nozzle with a minimum throat area larger than the critical minimum throat area, see e.g. [33]. Initially the oncoming upper deck flow is accelerated in the converging part of the nozzle. However, unlike to classical theory where the flow immediately decelerates downstream of the minimum throat area the interacting flow in the core region of the nozzle is accelerating still in the first part of the diverging part of the nozzle before finally decelerating back to the undisturbed subsonic flow state $P = A = \bar{U} = 0$. The reason, of course, is to find in the viscous inviscid interaction taking place between the inviscid flow in the upper deck and the viscous boundary layers at the walls. The interacting boundary layers are forming a "viscous" Laval nozzle meaning that the effective flow area felt by the upper deck flow does not consist of the "geometric" contribution S alone but also of a viscous part $-A$, cf. figure 4.3(b), resulting form the lower deck reaction to pressure variations in the upper deck. This is expressed by the relation $-A^\star = -A + S$, cf. (2.206), for the overall displacement thickness and also by the interaction law (2.214) for steady flow

$$G'_{[n]}(P; K, \Gamma, \Lambda, N)\frac{\mathrm{d}P}{\mathrm{d}X} = Q\frac{\mathrm{d}A^\star}{\mathrm{d}X} = Q\frac{\mathrm{d}}{\mathrm{d}X}(A - S). \qquad (4.13)$$

Figure 4.5(a) again shows the distribution of P for the case of λ_2, but now together with S, $-A$ and $-A^\star$. The flow in the lower deck is accelerated as long $\mathrm{d}P/\mathrm{d}X < 0$ and by continuity arguments this results in a thinning of the boundary layer, i.e. $-A < 0$, reducing the contribution of the surface mounted hump on the displacement effect and thus delaying the point of deceleration into the beginning of the diverging part of the geometric nozzle. The effective shape of the "viscous" nozzle is given by $-A^\star$. The location of the minimum of the effective throat area now corresponds with the minimum of the pressure distribution, as one would have guessed by application of
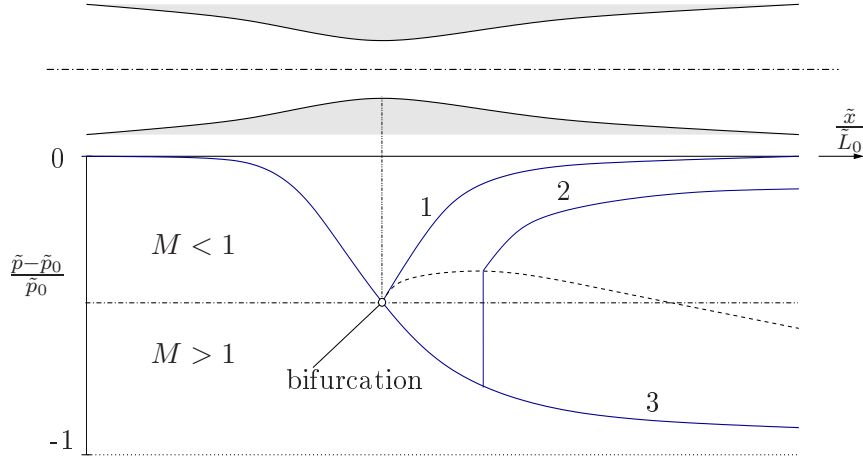
Figure 4.4: Sketch of the pressure distribution in an ideal Laval nozzle according to classical theory (inviscid noninteracting flow, one-dimensional, perfect gas).

classical Laval nozzle theory to this "viscous" Laval nozzle and which follows from (4.13) considering $G'_{[2]}(P_{min}) \neq 0$.

If the height of the surface mounted hump is successively increased to λ_s the minimum in the pressure distribution eventually approaches $P_s = -1$ meaning that at this point sonic flow conditions are obtained for the first time. In classical theory of Laval nozzles this is the limiting case of a Laval nozzle of critical minimum throat area and no steady solutions exist for a further reduction of the throat area, i.e. increase of the surface mounted hump. Moreover, in classical theory the sonic state present at the location of the minimum throat area would correspond to a bifurcation point in the pressure distribution from which two branches of continuous solutions evolve, one corresponding to a subsonic decelerating and the other corresponding to a supersonic accelerating flow, cf. branch 1 and branch 3 in 4.4 respectively. The numerical results for the pressure distribution in figure 4.3(a) clearly show that the bifurcation point for λ_s is eliminated by the presence of viscous inviscid interaction. From the former two branches only the one corresponding to the subsonic flow remains. Furthermore, the height of the surface mounted hump can be increased above λ_s, cf. case λ_3 in figure 4.3(a). The pressure distribution for λ_3 indicates that the upper deck flow is accelerated first to

supersonic flow, but afterwards *smoothly* decelerated to subsonic flow again. Such a solution has no counter part in classical Laval nozzle theory. Figure 4.5(c) reveals that the interacting boundary layers are forming a "viscous" nozzle consisting out of two throats and one anti-throat and that a *local* supersonic flow regime is confined in between the two "viscous" throats. The two sonic states are located at the minima of the two "viscous" throats and the minimum of P is located at the maximum of the "viscous" anti-throat. This immediately follows from equation (4.13), since in case of an extremum of $A^\star$, i.e $dA^\star/dX = 0$, P takes an extremum, i.e. $dP/dX = 0$, if the flow is not sonic, i.e. $G'_{[2]} \neq 0$, or otherwise dP/dX can be $\neq 0$ at a sonic state, i.e. $G'_{[2]} = 0$.

Furthermore, it is found that the height of the surface mounted hump cannot be increased above a certain critical value λ_c above which no steady solutions can be found. Very much alike the case of an ideal Laval nozzle in classical theory, cf. solution branch 3 in figure 4.4, the solution for λ_c is just the solution which leads to a transition from the subsonic to the supersonic regime, i.e. $P = -2$ for $X \to \infty$. To this end, the "viscous" nozzle, cf. $-A^\star$ in figure 4.5(d), is forming a nozzle consisting of one throat and one anti-throat leading to a shock free acceleration of the upper deck flow from sub- to supersonic flow conditions. Moreover, it is found that whilst approaching λ_c from below, the region around the location of the minimum in the pressure distribution is almost forming a cusp, cf. figure 4.3(a). From a numerical point of view the numerical solution is indistinguishable to the machine precision mp from the numerical solution for λ_c, i.e. $0 < \lambda_c - \lambda < mp$, as long as the flow in the nozzle is accelerating, i.e. $dP/dX < 0$. Then the solution seems to split form the solution for λ_c leading to a relatively rapid transition from super- to subsonic. Interestingly enough, there exists a classical counterpart to such a solution which is depicted in figure 4.4, cf. branch 2. A normal shock in the diverging part of the nozzle leads to the transition form super- to subsonic flow, the position of the shock depends on the outflow condition at the nozzle exit. However, due to the viscous inviscid interaction such a weak normal shock is smoothed out or regularized by the formation of a pseudo-shock, cf. chapter 3. By means of the numerical
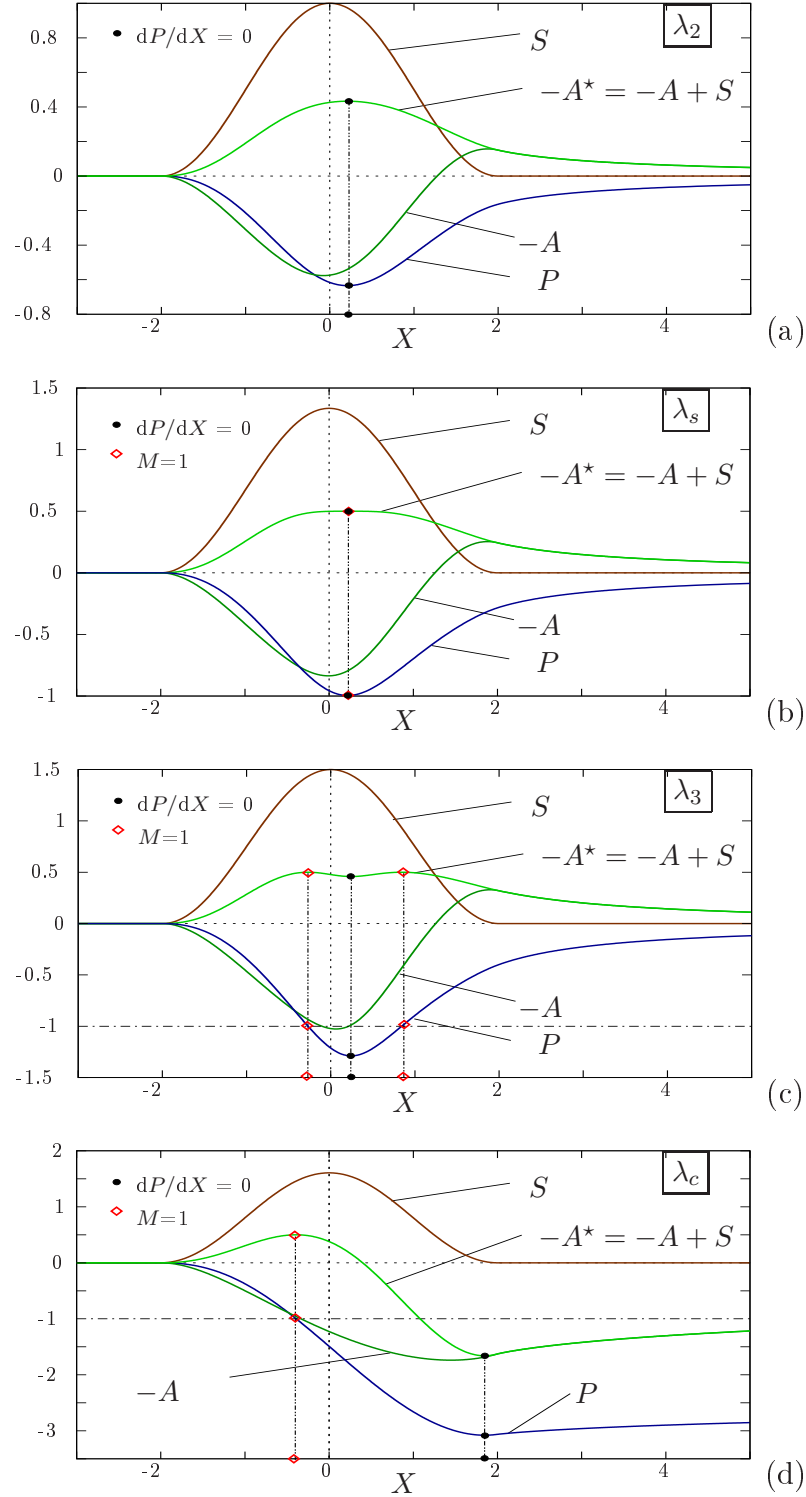
Figure 4.5: Plot of P-, $-A$-, S- and $-A^\star = -A + S$-distribution for various heights λ of the surface mounted hump. (a) $\lambda_2 = 1.0$, (b) $\lambda_s \approx 1.335$, (c) $\lambda_3 = 1.5$, (d) $\lambda_c = 1.60624...$. $Q = 1$.

homotopy continuation method adopted an infinite number of alike solutions can be found for $0 < \lambda_c - \lambda < mp$, cf. figure 4.3. The position of the pseudo-shock is moved successively further downstream until it eventually would leave the physical domain downstream resulting in the limiting case for $\lambda = \lambda_c$. The flow in such a regime, in analogy to classical Laval nozzle theory, can be considered to be nearly choked. The strength of such a pseudo-shock forming in the choked flow regime eventually is large enough to force the flow in the lower deck to separate, cf. figure 4.3(c). Such a phenomenon is commonly encountered in technical transonic diffusers, cf. e.g. [54], also in occurrence with self-sustained shock oscillations, see for instance [54], [93]. The unsteady reaction of such pseudo-shocks solutions will be discussed in section 4.3 to some extend.

4.2.1   Inverse Design of a Laval Nozzle

From the viewpoint of the technical design of slender nozzles the issue of the right shape of such a device in order to obtain a certain desired pressure distribution in the nozzle is more appropriate. The changes in the numerical scheme are small, instead of $S(X)$ now $P(X)$ is prescribed and $S(X)$ takes the role of the unknown. The numerical results for the pressure distribution given by

$$P(X) = P_\infty(\tanh(X) + 1)/2 \qquad (4.14)$$

are plotted in figure 4.6. It is evident that a nozzle causing the desired pressure distribution has to have a slowly diverging part reaching far downstream.

So far, only perfect gas like media has been considered. If, however, dense gases exhibiting mixed nonlinearity are to be considered as well, then an acceleration of the working media from subsonic to supersonic flow cannot be accomplished by means of a nozzle consisting of a single throat even in the classical case of one-dimensional noninteracting inviscid flow, cf. [35]. Rather a combination of throats and anti-throats has to be used. In such a case, the described inverse design of a Laval nozzle is most useful, since the procedure of successively increasing the height of a nozzle of otherwise given
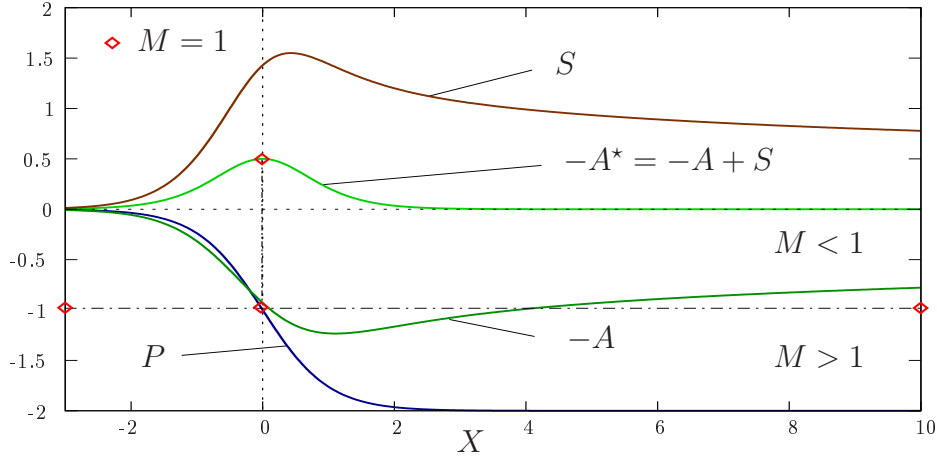
Figure 4.6: Inverse design of a nozzle for perfect gas like fluids ($n = 2$). $Q = 1$.

shape until a critical value of the nozzle height is reached will, in general, not result in a transition from sub- to supersonic flow conditions. Figure 4.7 shows numerical results for an example case of a dense gas.

For the numerical results presented in this section the number of grid points in ξ- and η-direction are $N_i = 1400$ and $N_j = 100$ respectively, $\xi_s^- = 300/N_i$, $\xi_s^+ = 1100/N_i$, $m^- = m^+ = 1.3$, $X_s^- = -6$, $X_s^+ = 6$, $Y_s = 0.2$, $\alpha_s = 0.98$, $Y_{max} \approx 9.9$.
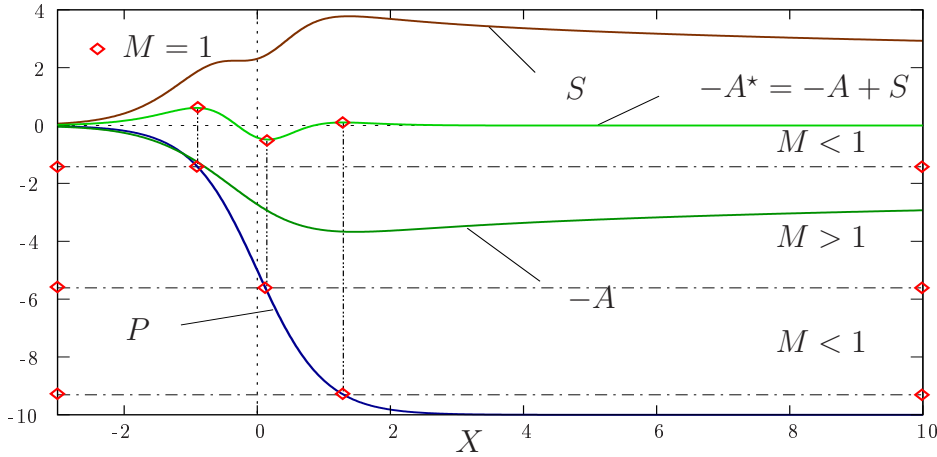

Figure 4.7: Inverse design of a Laval nozzle for dense gas ($n = 4$, $K > 0$, $\Gamma_{-\infty} > 0$, $\Lambda_{-\infty} = 0.44$, $N_{-\infty} = 0.08$); $Q = 1$.

4.3   Unsteady Flow in "Viscous" Laval Nozzles

4.3.1   Linearized Problem and Validation of the Numerical Algorithm

Before the numerical scheme for the unsteady interaction problem described in section 4.1.2 is applied to pseudo-shock solutions forming in the nearly choked flow regime in a slender Laval nozzle, cf. discussion in section 4.2, the unsteady triple deck problem shall be discussed under the assumption that the problem can be represented by the linearized version of the governing equations, i.e. in case of small perturbations introduced by a sufficiently small surface mounted hump. For the linearized equations of the interaction problem in definition 2.2.1 a solution can be given in closed form for appropriate surface functions $S(X, T)$ by means of Fourier transforms, cf. e.g. [51] or [21]. This is convenient in so far as the linearized problem poses a possibility to validate the numerical scheme developed for the fully nonlinear case. On the other hand, the obtained numerical solutions allow a first glimpse on the time-dependent behavior of the physical system.

The problem is solved for the expression

$$S(X, T) = \begin{cases} 0 & T \leq 0 \\ 0.01 \ \exp(-X^2) & T > 0 \end{cases} \tag{4.15}$$

describing the shape of the surface mounted hump and under the initial conditions

$$P \equiv \bar{U} \equiv 0 \qquad @T = 0. \tag{4.16}$$

The temporal evolution of the Fourier transform of the pressure distribution $P^\wedge$ for the linearized problem under the forcing of (4.15) is given by

$$\begin{aligned} P^\wedge(\omega; T) &= \frac{1}{\sqrt{2\pi}} \int_{-\infty}^{\infty} P(X, T) \ e^{-i\omega X} dX = \\ &= \frac{Q}{\sqrt{2}} \frac{i\omega}{\mathcal{P}(\omega)} e^{-\omega^2/4} \left(1 - e^{-\mathcal{P}(\omega)T}\right) \end{aligned} \tag{4.17}$$
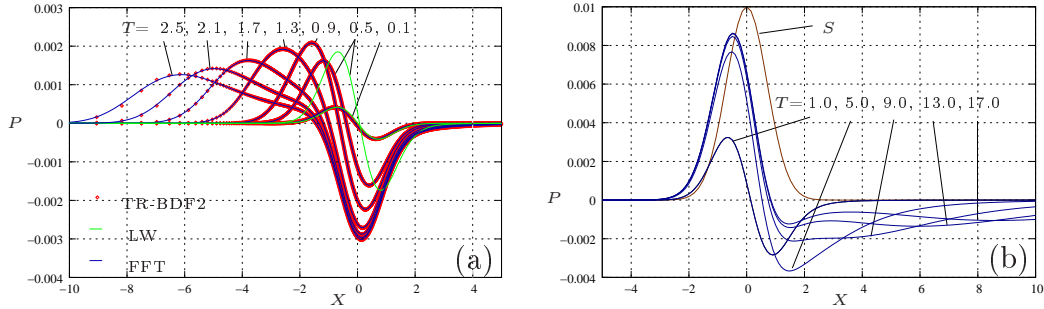
Figure 4.8: Evolution of the pressure distribution for the linearized problem. (a) Subsonic flow regime, i.e. $K > 0$, and comparison of solutions by different numerical schemes: TR-BDF2, Lax-Wendroff (LW), linearized problem and Fast-Fourier Transform (FFT). (b) Supersonic flow, i.e. $K < 0$. $Q = 0.5$, $\Gamma_{-\infty} = 1$.

with $\mathcal{P}(\omega) = \frac{Q}{3\mathrm{Ai}'(0)}(\mathrm{i}\omega)^{4/3} + \mathrm{i}\omega \, \mathrm{sign}\,(K/\Gamma_{-\infty})$. The relevant steps for the derivation of equation (4.17) can be found in [24]. The transformation from Fourier space (ω, T) back to the physical space (X, T) is achieved by means of Fast-Fourier Transforms, cf. e.g. [6], using the GSL library package. The results are shown in figure 4.8 for (a) subsonic and (b) supersonic flow. Moreover, also numerical results obtained by the application of the TR-BDF2 scheme developed for the fully nonlinear problem, cf. section 4.1.2, and an implicit Lax-Wendroff scheme, cf. section 4.1.2, are depicted in figure 4.8(a). The time step is chosen quite large, i.e. $\Delta T = 0.1$. Inspection of the numerical solutions reveals that the agreement between the solution of the linearized problem and the solution calculated by means of the TR-BDF2 scheme are excellent, whereas the disturbances calculated by the Lax-Wendroff scheme obviously move at different finite speeds. This phenomenon, which has also been observed for the case of an implicit upwind scheme plus a simple adding of the source term not shown here, has already been mentioned and discussed in section 4.1.2. Considering the temporal development of the pressure distribution itself, two different time scales can be distinguished. Both in the subsonic and in the supersonic case the presence of the surface mounted hump immediately is felt downstream of the hump, whereas there is also an immediate upstream influence in case of supersonic upper deck flow. On the other hand pressure disturbances are seen to travel at finite speeds in both

cases as well. These are moving upstream in case of subsonic flow, cf. figure
4.8(a), and downstream in the supersonic case, cf. 4.8(b). This is in agree-
ment with the reasoning performed for the choice of an appropriate time
scaling used in the derivation of the time-dependent upper deck problem, cf.
remark 2.2.2. There it has been argued that the time scaling shall preserve
the transient behavior of the system which is governed by the slowest time
scales in order to capture the longterm behavior of the system. The order of
magnitude of the slowest time scales can be estimated by the characteristic
speed $\lambda_\eta = M_0 u - c = c(M-1)$, cf. remark 2.2.2. Consequently, disturbances
are expected to be traveling upstream for $M < 1$ and downstream for $M > 1$.
Conversely the faster time scales are estimated by $\lambda_\zeta = c(M+1) > 0$. Sub-
jected to a time scaling based on the slower time scales this results in infinite
large positive characteristic speeds leading to the observed immediate up-
or downstream influence. The upstream influence exhibited by an obstacle
in supersonic upper deck region flow in slender nozzles is typical for triple
deck problems in supersonic flow in general, cf. compressive free interaction,
e.g. [52].

4.3.2   Nearly choked Flow without Flow Separation

A pseudo-shock forming in the diverging part of a slender nozzle of shape
given by relation (4.12) with sufficient strength to bring the boundary layer
flow at the verge of separation is perturbed by a small oscillating surface
mounted hump, S_{osc}, in the downstream part of the pseudo-shock, cf. figure
4.9. According to the insight gained into the behavior of the physical system
by studying the linearized case the small hump is likely to evoke an imme-
diate flow response since it perturbs the downstream region of influence of
the nozzle. If the location of the oscillating hump is moved sufficiently far
downstream then the immediate flow response can be expected to be weak.
On the other hand, perturbations will travel at finite speeds upstream of the
oscillating hump finally starting to interact with the sensitive pseudo-shock.
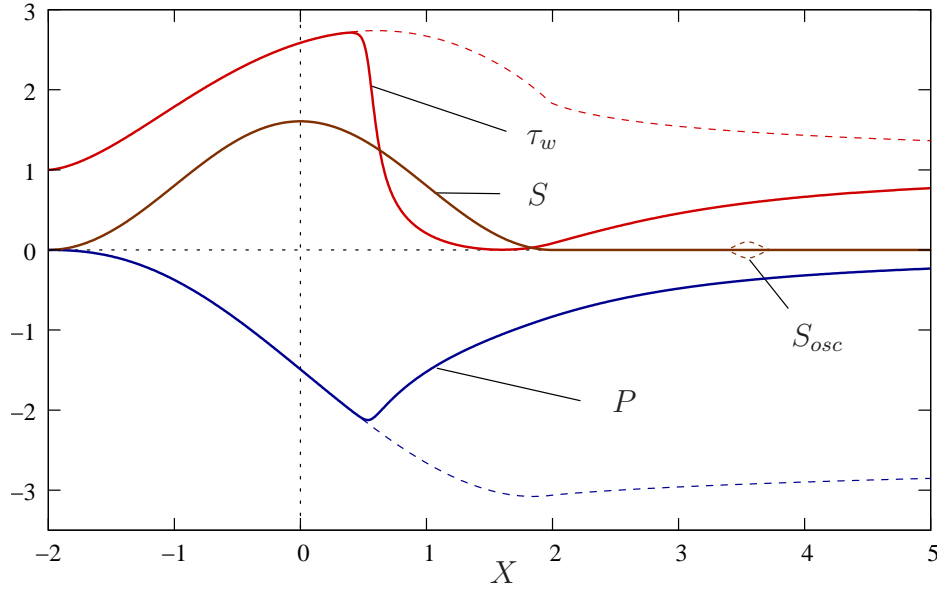
Figure 4.9: Initial conditions. The pseudo-shock in the diverging part of the nozzle given by S is perturbed by a small oscillating surface mounted hump, S_{osc}, downstream. The flow in the lower deck is close to flow separation. $Q = 1$, $K > 0$, $\Gamma_{-\infty} = 1$.

The oscillating hump is given by the expression

$$S_{osc}(X,T) = \begin{cases} 0 & |X - 3.55| > 0.2, \\ 0.005 \ \sin(2\pi Sr T) \ \left(1 + \cos(\pi \frac{X-3.55}{0.2})\right) & |X - 3.55| \leq 0.2, \end{cases}$$

(4.18)

it is located at $X = 3.55$, spans from $X = 3.35$ to $X = 3.75$ and oscillates at a dimensionless frequency Sr, its maximum height is 0.01. The reaction of the pseudo-shock of the initial flow configuration, cf. figure 4.9, to the presence of the oscillating hump given by (4.18) shall be calculated for $Sr = 1/T_p = 1.0$. T_p denotes the time period. The time step used in the computations is $\Delta T = 0.01$. The pseudo-shock in figure 4.9 by nature is not located at a certain position, however, considering the wall shear stress distribution in figure 4.9 the region of steepest descent spans from $X \approx 0.5$ to $X \approx 1.5$. It can be expected that it is this region which is most sensitive to perturbations of the flow field. The results for the pressure disturbance
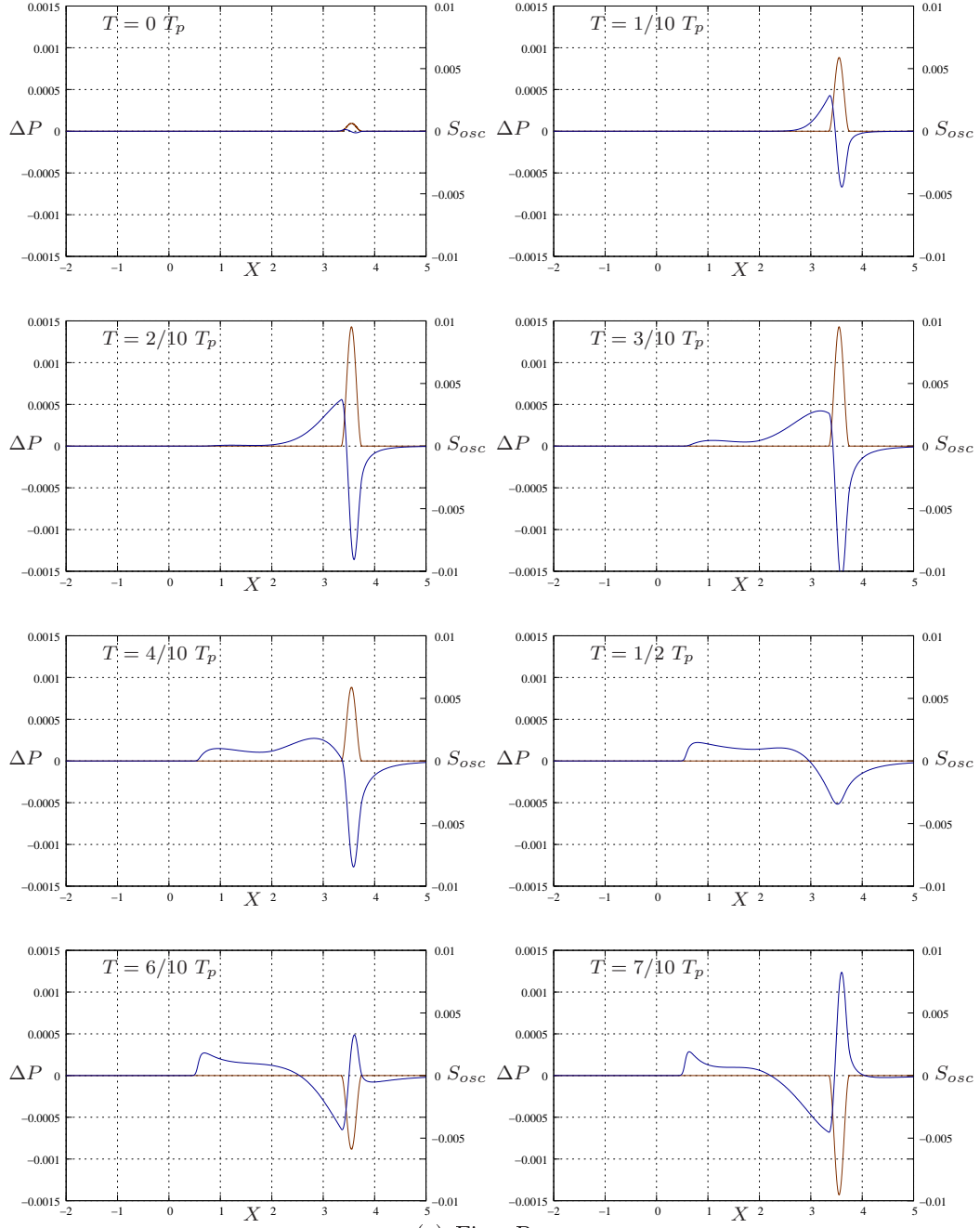
(a) First Part

Figure 4.10: Pressure disturbance $\Delta P = P(X,T) - P(X,0)$ evoked by an oscillating surface mounted hump S_{osc}. $Sr = 1$, $T_p = 1.0$; $\Delta T = 0.01$.
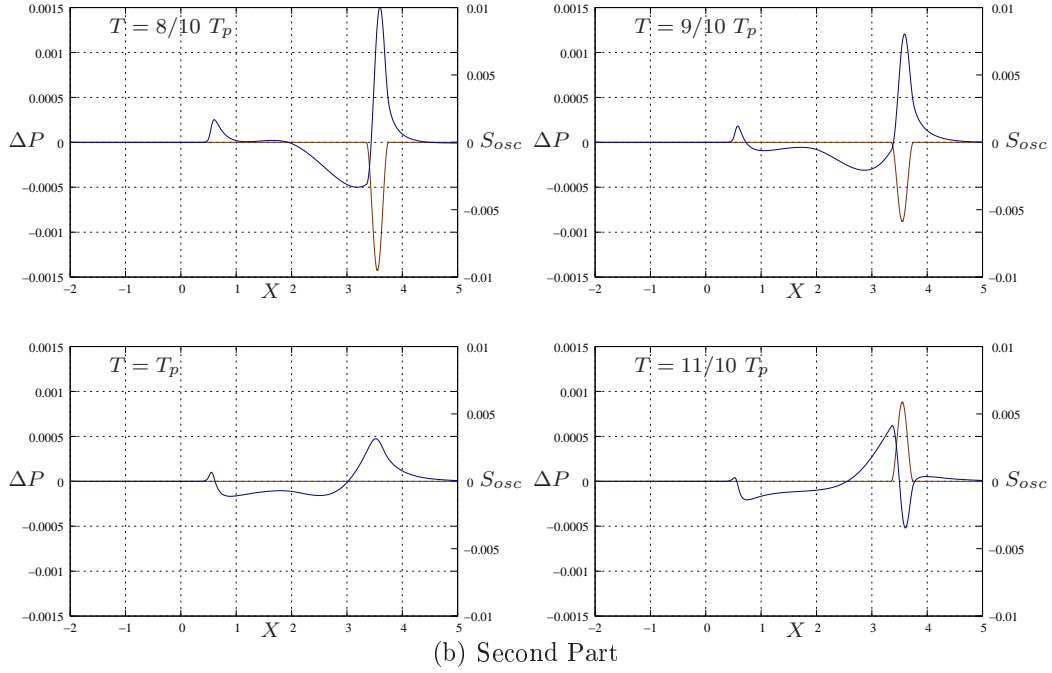
Figure 4.10: Pressure disturbance $\Delta P = P(X,T) - P(X,0)$ evoked by an oscillating hump S_{osc}. $Sr = 1.0$, $T_p = 1.0$; $\Delta T = 0.01$.

$\Delta P = P(X,T) - P(X,0)$ over the time span $T = 0$ to $T = T_p$ is shown in figure 4.10 together with S_{osc}. The disturbances introduced by the oscillating hump are traveling upstream very much alike the solutions to the linearized problem for subsonic flow shown in the previous section and no strong reaction of the pseudo-shock can be observed at first. However, after some time a flow response is building up which is strongest in the region of $X \approx 0.5$ to $X \approx 1.0$. This corresponds with the beginning of the pseudo-shock in the initial flow configuration, cf. figure 4.9, and therefore is a result of the interaction of the pseudo-shock and the forcing S_{osc}. Since disturbances in a supersonic upper deck flow regime are traveling downstream rather than upstream as in the subsonic regime, no perturbations are generated upstream of the pseudo-shock. The pseudo-shock oscillates at the same harmonic frequency of the forcing as can be seen by inspection of figure 4.11. Furthermore, it is found that the maximum amplitude of the pressure oscillations and consequently the maximum of the oscillation of the shock position as
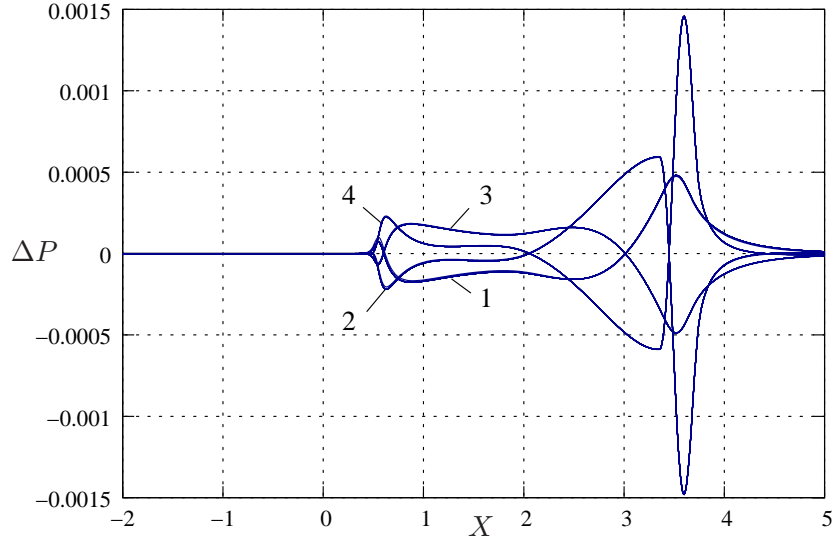
Figure 4.11: Solution curves no. 1: T $= T_p$, $2T_P$, ..., $20T_p$; solution curves no. 2: T $= 1\frac{1}{4}T_p$, $2\frac{1}{4}T_P$, ..., $19\frac{1}{4}T_p$; solution curves no. 3: T $= 1\frac{1}{2}T_p$, $2\frac{1}{2}T_P$, ..., $19\frac{1}{2}T_p$; solution curves no. 4: T $= 1\frac{3}{4}T_p$, $2\frac{3}{4}T_P$, ..., $19\frac{3}{4}T_p$. $\Delta P = P(X,T) - P(X,0)$. $Sr = 1.0$, $T_p = 1.0$; $\Delta T = 0.01$.
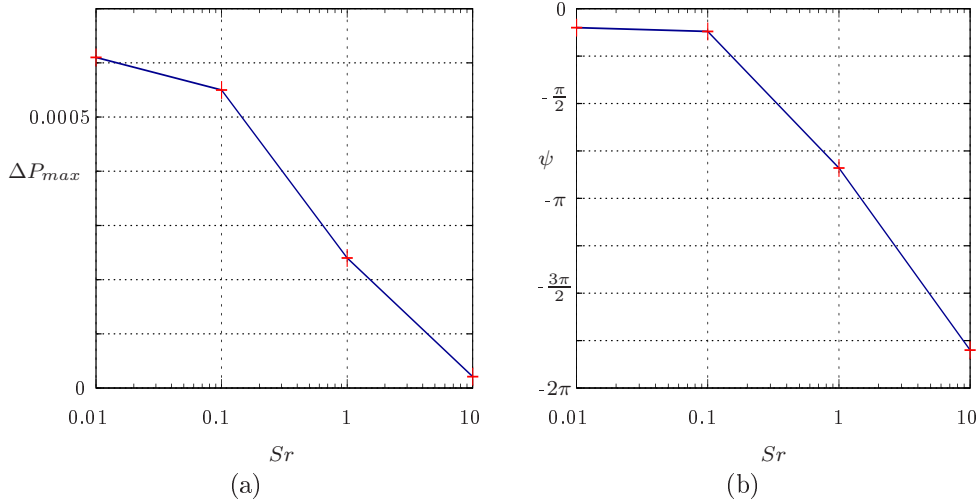

Figure 4.12: (a) Maximal pressure disturbance obtained by the oscillating pseudo-shock and (b) phase displacement between the pseudo-shock oscillation and the oscillating surface mounted hump for different values of Sr.

well is decreasing with increasing Sr, cf. figure 4.12(a). This coincides very well with the experimental findings reported in [7]. There, it had been found that the influence of the shock/boundary layer interaction on the shock oscillations generated by a harmonic flow disturbance downstream of the shock is negligible as long as there is no significant flow separation generated by the shock. The authors even used a purely inviscid model to explain the shock movements and the phenomenon of decreasing amplitude of the shock oscillations. The numerical results presented in this section suggest that the influence of the shock boundary layer interaction is weak indeed. The case of separated nearly chocked flow will be discussed in the following chapter.

4.3.3   Linear Stability of Steady States

Numerical calculations of the unsteady flow field under the influence of an oscillating hump, cf. previous section, results in convergence problems of the numerical scheme in presence of flow separation. Despite the effort of using a stiff time integration the numerical schemes fails after few time steps even for very small time steps. The results obtained in the early stages of the calculations indicate a strong tendency of the separation bubble towards self-sustained dynamics. In order to be able to better interpret the observed behavior a linear stability analysis is performed for various solutions of the steady Laval nozzle flow thus eliminating the need of a time-integration of the full nonlinear problem.

The Analysis

The fundamental canonical problem, cf. definition 2.2.1, is written as a dynamical system, cf. [3], [89], [46],

$$\mathbf{C}\frac{\partial}{\partial T}\left(\bar{U}, P\right)^T = \mathcal{F}_{TD}\left(\bar{U}, P; \lambda\right) \quad \text{in } \Omega \quad \& \quad \mathcal{B}(\bar{U}, P) = 0 \quad \text{on } \partial\Omega \quad (4.19)$$

with $\Omega = \mathbb{R} \times \mathbb{R}^{\geq 0}$. In the case considered here the singular "capacity" matrix $\mathbf{C}$ is defined as

$$\mathbf{C} = \begin{pmatrix} 0 & 0 \\ 0 & 1 \end{pmatrix} \tag{4.20}$$

and the operator $\mathcal{F}_{TD}$ is defined as

$$\mathcal{F}_{TD}\left(\bar{U}, P; \lambda\right) = \begin{pmatrix} \left(Y + \bar{U}\right)\bar{U}_X - \left(1 + \bar{U}_Y\right)\int_0^Y \bar{U}_X \mathrm{d}\bar{Y} + P_X - \bar{U}_{YY} \\ G'_{[2]}(P; K, \Gamma_{-\infty})P_X + Q\left(S_X(X, T; \lambda) - A_X\right) \end{pmatrix}. \tag{4.21}$$

The parameter λ again denotes the height of the surface mounted hump in equation (4.12). The "boundary" conditions $\mathcal{B}(\bar{U}, P) = 0$ are given by the equations (2.209) to (2.213), which are already linear equations. The governing equations are then linearized about a steady state $(\bar{U}_0(X, Y; \lambda), P_0(X; \lambda))^T$

$$(\bar{U}, P)^T = (\bar{U}_0(X, Y; \lambda), P_0(X; \lambda))^T + (\bar{U}_1(X, Y, T), P_1(X, T))^T \tag{4.22}$$

leading to

$$\mathbf{C}\frac{\partial}{\partial T}(\bar{U}_1, P_1)^T = \mathcal{L}\left(\bar{U}_0, P_0; \lambda\right)(\bar{U}_1, P_1)^T \quad \& \quad \mathcal{B}_L(\bar{U}_1, P_1) = 0. \tag{4.23}$$

Inserting the ansatz

$$(\bar{U}_1, P_1)^T = \mathrm{e}^{\mu T}\mathbf{y} \tag{4.24}$$

leads to a generalized eigenvalue problem

$$\left(\mathbf{C}\mu - \mathcal{L}\left(\bar{U}_0, P_0; \lambda\right)\right)\mathbf{y} = 0 \quad \& \quad \mathcal{B}_L(\mathbf{y}) = 0. \tag{4.25}$$

An explicit solution for the spectrum $\mu(\omega) \in \mathbb{C}$ with $\omega \in \mathbb{R}$ can be given for the trivial "state" $(\bar{U}_0, P_0)^T = \mathbf{0}$ only, which reads as

$$\mu(\omega) = \frac{Q}{3\mathrm{Ai}'(0)}\sin(\tfrac{\pi}{6})|\omega|^{4/3} + \mathrm{i}\omega\left(\mathrm{sign}(K) - \frac{Q}{3\mathrm{Ai}'(0)}\cos(\tfrac{\pi}{6})|\omega|^{1/3}\right). \tag{4.26}$$

A detailed derivation of relation (4.26) is given in appendix D. For the calculation of the eigenvalue spectrum for nontrivial "states" one has to rely on numerical solutions. To this end, system (4.19) is represented by

$$\mathbf{C}\frac{\mathrm{d}}{\mathrm{d}T}\mathbf{s} = \mathbf{F}(\mathbf{s};\lambda) \qquad \mathbf{s},\mathbf{F} \in \mathbb{R}^d. \tag{4.27}$$

$\mathbf{s}$ denotes the solution vector and $\mathbf{F}(\mathbf{s};\lambda) = 0$ denotes the system of algebraic equations resulting form the numerical discretization of the governing equations for the stationary problem and which has been described in section 4.1.1 and 4.1.3 in detail. Equation (4.27) can be seen as the first step in a method of lines leading to a system of ODEs. The singular capacity matrix $\mathbf{C}$ now is a large, sparse $d \times d$-matrix

$$\mathcal{M}(d,\mathbb{R}) \ni \mathbf{C} = \begin{pmatrix} 0 & \ldots & 0 & 0 & \ldots & 0 & \ldots & 0 & 0 \\ \vdots & \ddots & \vdots & \vdots & \ldots & \vdots & \ddots & \vdots & \vdots \\ 0 & \ldots & 0 & 0 & \ldots & 0 & \ldots & 0 & 0 \\ 0 & \ldots & 0 & 1 & \ldots & 0 & \ldots & 0 & 0 \\ \vdots & \vdots & \vdots & \vdots & \ddots & \vdots & \vdots & \vdots & \vdots \\ 0 & \ldots & 0 & 0 & \ldots & 0 & \ldots & 0 & 0 \\ \vdots & \ddots & \vdots & \vdots & \ldots & \vdots & \ddots & \vdots & \vdots \\ 0 & \ldots & 0 & 0 & \ldots & 0 & \ldots & 0 & 0 \\ 0 & \ldots & 0 & 0 & \ldots & 0 & \ldots & 0 & 1 \end{pmatrix}. \tag{4.28}$$

Performing the same steps as in case of the continuous infinite dimensional system leads to the finite dimensional equivalent of equation (4.23)

$$\mathbf{C}\frac{\mathrm{d}}{\mathrm{d}T}\mathbf{s}_1 = \mathbf{L}\,\mathbf{s}_1. \tag{4.29}$$

The $d \times d$-dimensional matrix $\mathbf{L} := D_\mathbf{s}\mathbf{F}(\mathbf{s}_0;\lambda)$ is the Jacobian of the numerical scheme $\mathbf{F}(\mathbf{s};\lambda)$ evaluated for $\mathbf{s_0}$. The generalized eigenvalue problem for the d discrete eigenvalues in the finite dimensional numerical case, cf. e.g. [29], finally reads

$$(\mathbf{C}\mu - \mathbf{L})\,\mathbf{y} = 0. \tag{4.30}$$

Most important of all, the singular sparse matrix $\mathbf{C}$ has only d nonzero entries in its diagonal. As a consequence the characteristic polynomial $\det(\mathbf{A} - \mu\mathbf{C})$ can be of order d as a polynomial in μ at the most and there exists a number of discrete finite generalized eigenvalues equal to the order of the characteristic polynomial, [29]. The generalized eigenvalue problem is solved using the `eigs` function of the MATLAB suite, which is an implementation of the iterative Arnoldi method, cf. e.g. [82].

The results for various values of the height λ of the surface mounted hump are shown in figure 4.13. A number of 1090 out of 1400 possible finite general eigenvalues which are nearest to the value 0 have been calculated. Figure 4.13(a) shows good agreement between the discrete eigenvalue spectrum obtained by the numerical method and the analytical eigenvalue spectrum given by the expression (4.26) which has been performed in order to validate the numerical procedure. The real values of the general eigenvalues $\Re\{\mu\} \leq 0$, thus the trivial state, as the numerical results for the unsteady problem have indicated so far, is linear stable. This statement remains valid for any initial flow field in the nozzle as long as no flow separation does occur, cf. figure 4.13(b), 4.13(c) and 4.13(f). However, taking a look at figure 4.13(d) and figure 4.13(e) where part of the eigenvalue spectrum has moved into the region of positive real values, i.e. $\Re\{\mu\} \geq 0$, it is evident that the occurrence of flow separation is linked with the linear instability of the steady flow. Moreover, the largest of the eigenvalues with positive real part are of quite large numerical values. Assuming that these may be essential for the temporal evolution of the flow field a numerical scheme would have to resolve to unfeasible small time steps. The author believes that these results obtained by the linear stability analysis give an explanation for the observed numerical problems mentioned at the beginning of this section. From a physical point of view, the eigenvalue spectra for various surface heights in figure 4.13 suggest that the occurrence of a region of separated flow caused by a pseudo-shock forming in the diffuser part of a nozzle leads to a loss of stability of the steady flow field. Moreover, preliminary numerical results, cf. section 4.3.4, indicate that the loss of stability is initiated by a conjugate-complex eigenvalue pair which crosses the imaginary axis, that is a Hopf-bifurcation or flutter insta-

(a)

(b)

(c)

Figure 4.13: Wall shear stress distribution (left) and corresponding eigenvalue spectrum (right) for various surface heights λ. Solid line in the eigenvalue spectra corresponds to the analytical solution for the trivial initial flow, i.e. $\lambda = 0$.

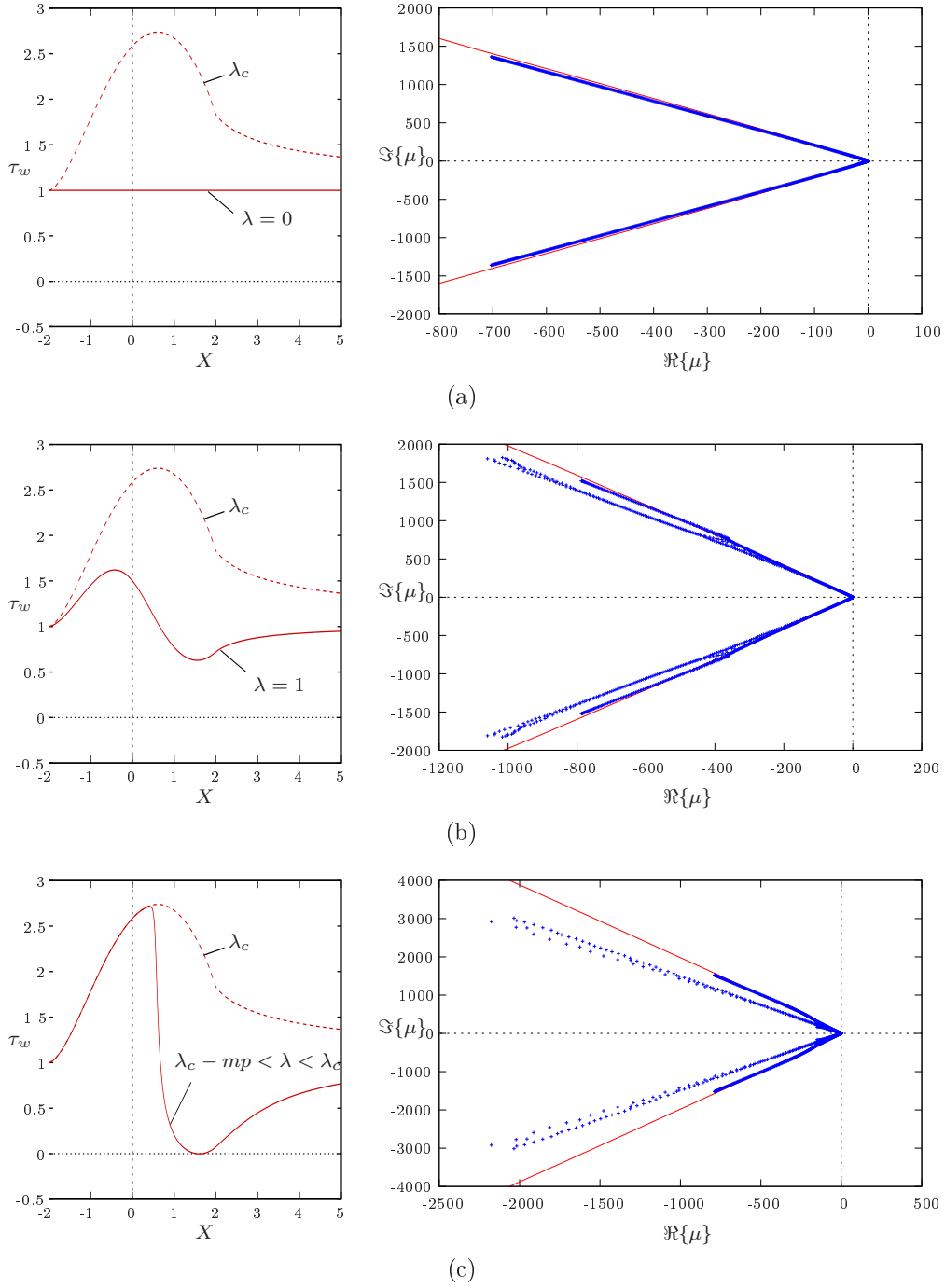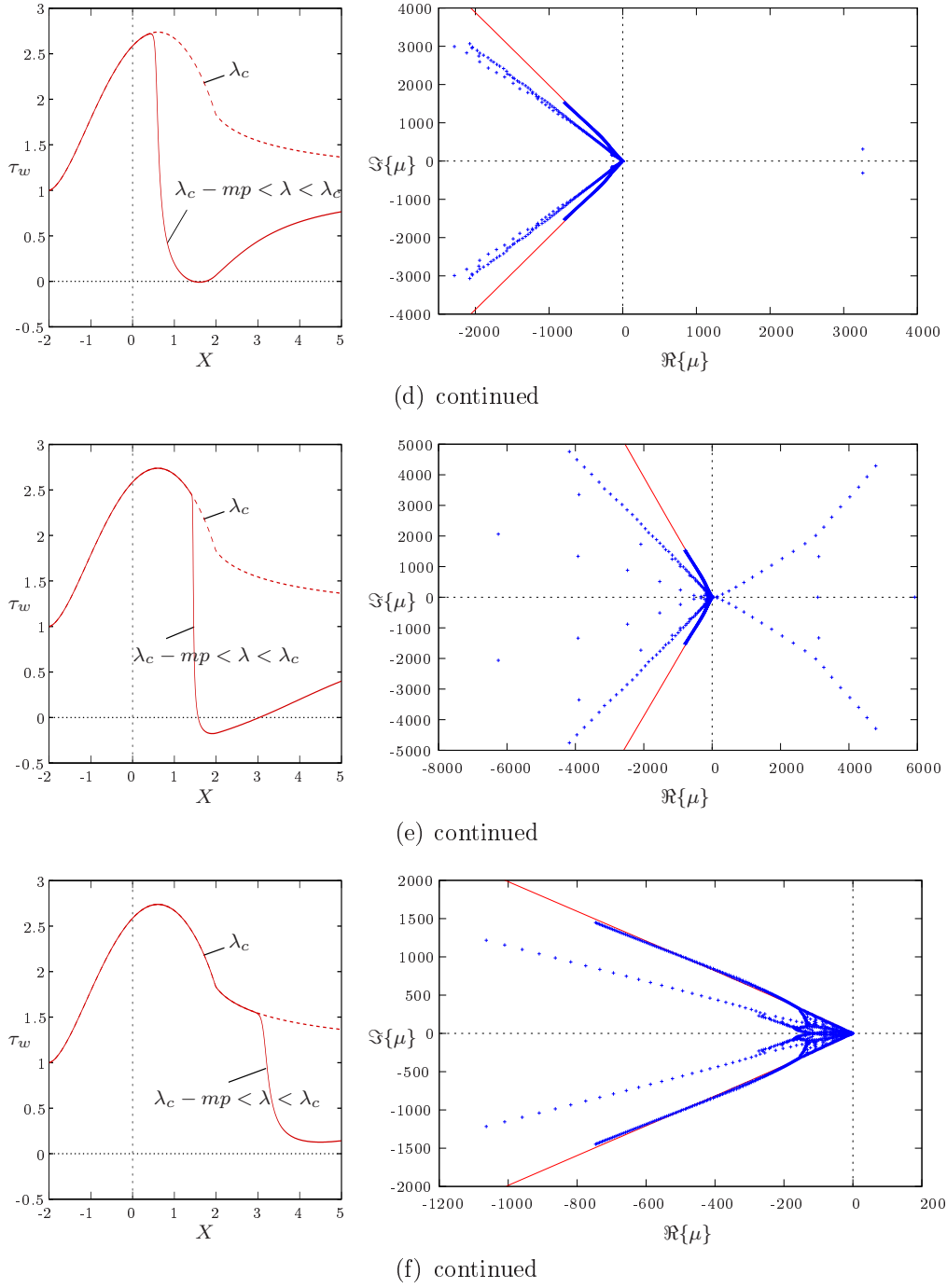(d) continued

(e) continued

(f) continued

Figure 4.13: Wall shear stress distribution (left) and corresponding eigenvalue spectrum (right) for various surface heights λ. Solid line in the eigenvalue spectra corresponds to the analytical solution for the trivial initial flow, i.e. $\lambda = 0$.

bility, cf. [89], [3]. The steady state remains the unique equilibrium state of the dynamical system, however, at the bifurcation point an exchange of stability from a stable to an unstable equilibrium occurs, [89]. Consequently, the unsteady flow field is likely to exhibit self-sustained dynamics and taking into account the eigenvalue spectrum for a relatively large separation region, figure 4.13(e), these self-sustained dynamics can be expected to exhibit high frequency tones which would be in line with experimental observations, [54]. However, it shall be pointed out that the statements concerning the possible nature of self-sustained oscillations given here so far are preliminary also in the light that the influence of nonlinear effects are not accounted for in the framework of a linear stability analysis. Therefore, suggestions for further work focusing on the distinguished case of the loss of stability, i.e. the situation, where the critical eigenvalue pair have zero real parts, is given in the following section.

4.3.4 Further Work

Preliminary numerical results (for $Q = 0.5$, $N_i = 1200$, $N_j = 100$, $\xi_s^- = 100/N_i$, $\xi_s^+ = 1100/N_i$, $m^- = m^+ = 1.3$, $X_s^- = -3$, $X_s^+ = 3$, $Y_s = 0.2$, $\alpha_s = 0.98$, $Y_{max} \approx 9.9$ and a slightly different surface mounted hump [1]) point in the direction that the loss of stability is caused by a conjugate-complex eigenvalue pair that crosses the imaginary axis suggesting a Hopf-bifurcation, cf. figure 4.14. The following aspects would be of interest for future work in this context:

- First, the physical relevance of the calculated eigenvalue pair has to be checked. To this end, the calculation of the pseudospectrum of the eigenvalue problem could give further insight, cf. e.g. [92]. However, the numerical procedure outlined in [92] mainly deals with the standard

----

[1]

$$S(X) = \begin{cases} 0 & X < -2.5 \\ \frac{\lambda}{2}(1 + \cos(\pi X/2)) & -2.5 \leq X < 0 \\ \lambda \exp(-2(X/2.5)^2) & 0 \geq X. \end{cases} \tag{4.31}$$
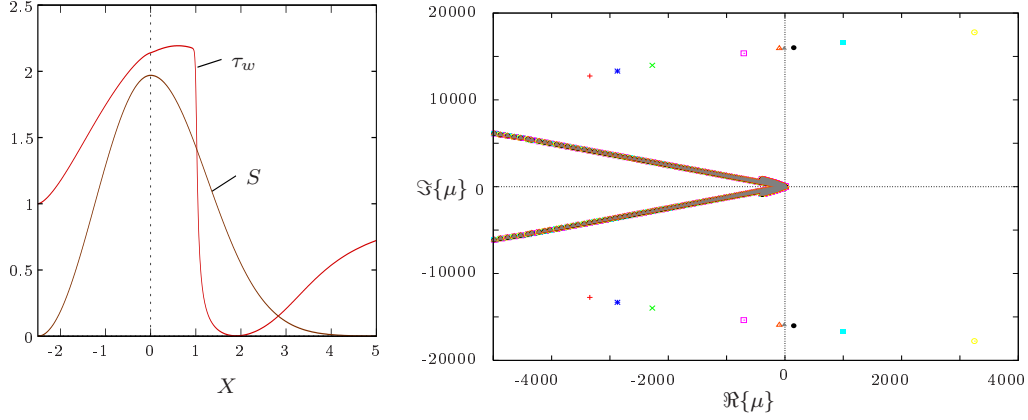
Figure 4.14: Preliminary results for the loss of stability scenario (for $Q = 0.5$, $N_i = 1200$, $N_j = 100$, $\xi_s^- = 100/N_i$, $\xi_s^+ = 1100/N_i$, $m^- = m^+ = 1.3$, $X_s^- = -3$, $X_s^+ = 3$, $Y_s = 0.2$, $\alpha_s = 0.98$, $Y_{max} \approx 9.9$ and a slightly different surface mounted hump). Different colors in the plot correspond to different solutions close to the solution of a pseudo-shock just strong enough that the wall shear stress becomes zero at one single point along the wall but no separation region forms yet.

eigenvalue problem, i.e. $(\mathbf{I}\mu - \mathbf{A})\mathbf{r} = 0$, say, and therefore would have to be extended to the general eigenvalue problem (4.30).

- If the critical eigenvalue pair proofs to be physically meaningful, then a dimension reduction of the dynamical system, cf. center manifold reduction theory, e.g. [89], [3], [83] amongst others, would be indicated in order to obtain a reduced problem of similar dynamical behavior as the original one which could then be analyzed analytically, i.e. non-linear stability analysis of the reduced system. A crucial point in this context will be to decide whether such a dimension reduction is applicable or not, especially whether the critical eigenvalue pair is sufficiently isolated from the rest of the eigenvalue spectrum. As the numerical results show part of the spectrum happens to cross the imaginary line in case of larger regions of flow separation, so the fulfillment of the last requirement may be questionable.

Another aspect of interest to the problem of shock oscillations could be to study the situation of a pseudo-shock in the diffuser part of the nozzle

in presence of a separation region which is *not* directly caused by the shock itself but rather caused by the adverse pressure-gradient in the subsonic flow region following the pseudo-shock, i.e. pressure-gradient-induced separated flow, cf. [54]. Thus the location of the shock and the separation region could be separated spatially and according to [54] the unsteadiness of such a flow situation is characterized by slower dynamics. It would be interesting to see whether the numerical scheme developed for the time-integration of the full nonlinear problem, cf. section 4.1.2, is capable to cope with the slower dynamics to be expected.

Chapter 5

Conclusions

It has been shown throughout this treatise that the problem of viscous in-
viscid interactions in internal, transonic, single phase and two-dimensional
high Reynolds numbers flows through channels that are so narrow that the
interacting core region flow becomes one-dimensional to leading order can be
consistently be described by a triple deck problem. The interacting core re-
gion hereby is represented by a single upper deck which is shared by the two
interacting boundary layers at the lower and upper channel walls. In partic-
ular previous work, Kluwick, [39], Kluwick & Gittler, [43], and Kluwick &
Braun & Gittler, [41], has been extended to include more general oncoming
flow types than the previously assumed flow through a channel of constant
cross section, real gas effects and unsteady effects focusing on the longterm
behavior of the system, i.e. on the slowest timescales governing the full
problem.

The resulting model equations then have been applied to study two fun-
damental flow problems.

In the first one the viscous inviscid interaction process is triggered by
the presence of a weak normal shock forming in a narrow channel of con-
stant cross section. It has been demonstrated that a shock discontinuity is
smoothed out by the interaction process ultimately leading to the forma-
tion of an internal shock profile. The mechanism of viscous inviscid shock
regularization has been identified. The viscosity dominated boundary layers

form a "viscous" nozzle adapting to and at the same time interacting with the inviscid channel core flow and thus allow a smooth transition of the core region flow through the interaction region. The mentioned properties of the interaction problem considered in this treatise have been used to study the internal shock profiles of various weak anomalous shocks forms possible in fluids of mixed nonlinearity (BZT fluids), i.e. rarefaction, sonic, double sonic and split shocks. It has been found that possible internal shock profiles are consistent with shock admissibility criteria formulated for the inviscid case. Moreover, the internal shock profiles due to viscous inviscid interactions share common features with those obtained by a classical thermo-viscous regularization, e.g. impending shock splitting, although the regularizing mechanism is governed by completely different underlying physics. As a numerical example the interacting flow of PP10 has been considered. The calculation of the characteristic length scales involved in the distinguished limit have shown that such flow phenomena as have been discussed here should occur in flows through slender channels in engineering practice for possible application of BZT fluids in the near future, e.g. organic Rankine cycle processes. Furthermore, the setup described here could proof to be an alternative to shock tubes currently in use to experimentally proof the existence of rarefaction shocks. The distinguishing advantages over a shock tube experiment would be that the shock position is stationary and that no other wave phenomena would have to be accounted for. A disadvantage, however, may be the need to guarantee laminar boundary layer flow up to very high Reynolds numbers. It shall be pointed out that the presented theory has been obtained by means of an asymptotic analysis and consequently the quality of such an asymptotic theory can only be validated by experiments or by CFD in the end.

In the second flow problem considered here the viscous inviscid interaction is triggered by a small Laval nozzle located in a channel of otherwise constant cross section. The discussion of the steady flow field through nozzles of different minimum cross sections but of otherwise similar shape has revealed that the occurrence of a single sonic point in the inviscid core region flow no longer corresponds to a bifurcation point as in classical inviscid one-dimensional Laval nozzle theory. The numerical results have shown that the

purely subsonic solution remains the only possible solution, that is no supersonic branch bifurcates at the sonic point. Moreover, the sonic point has been found to move slightly downstream of the location of the minimum throat area and the minimum throat area is larger still than the critical minimum cross section in contrast to classical Laval nozzle theory. The reason for this again is the possibility of the boundary layers to adapt to and interact with the core region flow in the interaction region. A quite similar behavior has been reported in CFD results for the simulation of transonic flow through micro nozzles, cf. [28], and for nozzle flow at moderately high Reynolds numbers where the viscous effects are important in the whole flow field, cf. [32], [65]. In the close vicinity of the minimal cross section that leads to a smooth transition form subsonic to supersonic conditions a pseudo-shock solution is forming in the diffuser part of the nozzle. The pseudo-shock part has been found to move successively downstream when the minimum cross section is approached. This flow regime has been denoted as nearly chocked flow in analogy to classical Laval nozzle theory. The reaction of such a pseudo-shock solution to small disturbances has been studied for two different situations. First the pseudo-shock has not been strong enough to cause the boundary layer flow to separate. There it has been found that the shock/boundary layer interaction plays only a minor role in accordance with experimental observations, [7]. In the second situation where the pseudo-shock has caused a distinct separation region the numerical scheme developed for the time-integration of the full nonlinear problem has turned out to be not capable to resolve the fast dynamics exhibited by the separation bubble. A linear stability analysis for steady solutions has shown that separation is linked to the loss of stability of the steady solution. Preliminary numerical results seem to indicate that the loss of stability is characterized by a Hopf-bifurcation, however, further investigations outlined in section 4.3.4 have to be performed to substantiate that statement.

Appendix A

List of Symbols

important operators

$\tilde{a}$	dimensional form of quantity a
∇	nabla operator
∇a	gradient of a
$\nabla \cdot \mathbf{a}$	divergence of $\mathbf{a}$
$\nabla \mathbf{a} = (\nabla \otimes \mathbf{a})^T$	
$(\nabla \cdot \mathbf{A})_i = \sum_{j=1}^{3} \partial_{x_j} A_{ij}$	
$\frac{Da}{Dt} = \frac{\partial a}{\partial t} + \mathbf{u} \cdot \nabla a$	substantial derivative
	(non-dimensional form)
$(\mathbf{a} \otimes \mathbf{b})_{ij} = a_i b_j$	tensor product
$(\mathbf{A} : \mathbf{B})_{ij} = \sum_{k=1}^{3} A_{ik} B_{kj}$	tensor contraction
$\frac{\partial a}{\partial b}\big|_c = \frac{\partial}{\partial c} a(b, c)$	partial derivative of thermodynamic quantity a
	w.r.t. b for fixed c
$(a)_n$	quantity a evaluated in
	region n in figure 2.1
$[a] = a^a - a^b$	jump connecting the two states a^a and a^b
$\Re\{a\}$	real part of a
$\Im\{a\}$	imaginary part of a
$a^\wedge$	Fourier transform of a

important variables

A	local throat area of a nozzle per unit depth (inviscid theory), negative perturbation of the displacement thickness (triple deck theory)
β	coefficient of thermal expansion
c	speed of sound
c_p	specific heat capacity at constant pressure
c_v	specific heat capacity at constant volume
$C = \left\lvert \frac{2\bar{\Gamma}}{K} \right\rvert$	coefficient used in affine transformation (2.201)
$\delta = \frac{\bar{R}_g}{\bar{c}_v}$	ratio of specific gas constant and specific heat, $\delta \ll 1$ for dense gases
δ_m	thickness of subregion $m = (3l,\ 3m)$ of boundary layer, see listing of subscripts
ϵ_1	perturbation parameter for one-dimensional inviscid nozzle flow
$\epsilon_2 = Re^{-\frac{1}{2}}$	perturbation parameter for noninteracting boundary layer flow
ϵ_3	perturbation parameter for interaction theory
e	specific inner energy
f	self similar part of stream function, solution of Blasius' equation (2.104)
γ	adiabatic exponent
Γ	fundamental derivative of gas dynamics
G	Grüneisen coefficient
$G_{[n]}$	leading order term of negative perturbation of upper deck mass flux density
$h,\ H$	specific enthalpy [1]
H_{3u}	thickness of upper deck
$\mathbf{I}$	identity matrix
$J_{[n]}$	leading order term of perturbation of mass flux density
k	thermal conductivity
K	transonic similarity parameter

K_θ	isothermal compressibility
K_s	isentropic compressibility
κ	exponential decay of eigensolutions of the triple deck problem for steady flow
Λ	first derivative of Γ with respect to ρ at constant s
$L_0,\ H_0$	characteristic length and height of the channel
λ	characteristic speed defined in theory of hyperbolic system of pdes or height of a surface mounted hump
μ	dynamic viscosity
μ_b	bulk viscosity
mp	machine precision
n	order of nonlinearity in $G_{[n]}$ or $J_{[n]}$
N	second derivative of Γ with respect to ρ at constant s
$\mathfrak{N}_{1D}$	number of orders of magnitude up to which the upper deck flow can be considered one-dimensional
$\mathbf{n_s}$	surface normal on the surface mounted hump
$p,\ P$	pressure [1]
Ψ	stream function
$\mathbf{q}$	vector of heat flux density
Q	coupling parameter in interaction law in canonical form (2.215)
$\rho,\ R$	density [1]
$\tilde{R}_g$	specific gas constant
s	thermodynamic entropy
$\mathbf{s},\ \mathbf{S}$	position vector describing the contour of surface mounted hump [1]
$s_2,\ S_2$	vertical component of $\mathbf{s}$ [1]
$t,\ T$	time [1]
$\theta,\ \Theta$	temperature [1]
$\boldsymbol{\tau}$	viscous stress tensor
T_p	periodic time
$U'_{20}(0)$	slope of the horizontal velocity profile at the wall in front of interaction region $\frac{\partial U_2^{(0)}(1,0)}{\partial Y_2}$

$\boldsymbol{u}, \mathbf{U}$	velocity vector [1]
$u,\ U$	component of velocity vector in horizontal, main stream direction [1]
$v,\ V$	component of velocity vector in vertical direction [1]
$\mathbf{x},\ \mathbf{X}$	position vector [1]
$x,\ X$	coordinate in horizontal, main stream direction [1]
$y,\ Y$	coordinate in vertical direction [1]

dimensionless groups

Re	Reynolds number
Ec	Eckert number
M_0	Mach number at reference state
Pr	Prandtl number
$\tilde{\beta}_0 \tilde{\theta}_0$	
G_0	Grüneisen coefficient at reference state
Sr	Strouhal number, dimensionless frequency

---

[1]Capital letters stand for boundary layer scaling, the exact region is indicated by the subscript which refers to the nomenclature of figure 2.1 and figure 2.5.

subscripts

0	reference state
1	quantity of inviscid noninteracting flow regime, see figure 2.1, in corresponding scaling
2	quantity of noninteracting boundary layer, see figure 2.1, in corresponding scaling
3	quantity of interaction region, see figure 2.1 or figure 2.5, in corresponding scaling eventually further specified by l,m,u
c	quantity at the critical thermodynamic point
i	solution of the (i)nviscid Euler equations
l	lower deck
m	main deck
u	upper deck
w	evaluated at the wall
$-\infty$	evaluated at the beginning of the interaction region $(X \to -\infty)$
$[n]$	order of nonlinearity in $G_{[n]}$ or $J_{[n]}$

superscripts

(k)	order of coefficient in asymptotic expansions
$*$	critical flow quantities at $M = 1$
a	undisturbed flow quantity immediately after weak normal shock
b	undisturbed flow quantity immediately before weak normal shock
$\star$	quantity of fundamental problem before Prandtl's transposition theorem is applied

Appendix B

Thermodynamic Relations

B.1   Some Thermodynamic Quantities

Speed of sound

$$\tilde{c}^2 = \frac{\partial \tilde{p}}{\partial \tilde{\rho}}\bigg|_{\tilde{s}} \tag{B.1}$$

$$c^2 = \frac{\tilde{c}^2}{\tilde{c}_0^2} = M_0^2 \frac{\partial p}{\partial \rho}\bigg|_{s} \tag{B.2}$$

Coefficient of thermal expansion

$$\tilde{\beta} = -\frac{1}{\tilde{\rho}} \frac{\partial \tilde{\rho}}{\partial \tilde{\theta}}\bigg|_{\tilde{p}} \tag{B.3}$$

Specific heat capacity at constant volume

$$\tilde{c}_v = \tilde{\theta} \frac{\partial \tilde{s}}{\partial \tilde{\theta}}\bigg|_{\tilde{\rho}} \tag{B.4}$$

Specific heat capacity at constant pressure

$$\tilde{c}_p = \tilde{\theta} \frac{\partial \tilde{s}}{\partial \tilde{\theta}}\bigg|_{\tilde{p}} \tag{B.5}$$

Adiabatic exponent

$$\gamma = \frac{\tilde{\rho}}{\tilde{p}} \frac{\partial \tilde{p}}{\partial \tilde{\rho}}\Big|_{\tilde{s}} \tag{B.6}$$

Isothermal compressibility

$$\tilde{K}_\theta = \frac{1}{\tilde{\rho}} \frac{\partial \tilde{\rho}}{\partial \tilde{p}}\Big|_{\tilde{\theta}} \tag{B.7}$$

Isentropic compressibility

$$\tilde{K}_s = \frac{1}{\tilde{\rho}} \frac{\partial \tilde{\rho}}{\partial \tilde{s}}\Big|_{\tilde{\theta}} \tag{B.8}$$

Grüneisen coefficient

$$G = \frac{\tilde{\rho}}{\tilde{\theta}} \frac{\partial \tilde{\theta}}{\partial \tilde{\rho}}\Big|_{\tilde{s}} \tag{B.9}$$

B.1.1   Magnitude of Grüneisen Coefficient

We write

$$G_0 = \frac{\tilde{\beta}_0 \tilde{c}_0^2}{\tilde{c}_{v,0}} \frac{\tilde{K}_{s,0}}{\tilde{K}_{\theta,0}} = \tilde{\beta}_0 \tilde{\theta}_0 \frac{\tilde{c}_0^2}{\tilde{R}_g \tilde{\theta}_0} \frac{\tilde{K}_{s,0}}{\tilde{K}_{\theta,0}} \frac{\tilde{R}_g}{\tilde{c}_{v,0}}, \tag{B.10}$$

cf. e.g. [56], for the Grüneisen coefficient defined in (B.9) and evaluated at reference state. For the order of magnitude estimate of G_0 in the dense gas regime the van der Waals equation of state, cf. e.g. [47], is applied which can be written as

$$\left(\pi + \frac{3}{\nu^2}\right)(3\nu - 1) = 8\tau \tag{B.11}$$

in the reduced variables

$$\pi = \frac{\tilde{p}}{\tilde{p}_c}, \quad \nu = \frac{\tilde{\rho}_c}{\tilde{\rho}}, \quad \tau = \frac{\tilde{\theta}}{\tilde{\theta}_c}.$$

Expressing $\tilde{\beta}$ by means of the van der Waals equation of states one finds

$$\tilde{\beta}_0 = \frac{1}{\tilde{\theta}_c}\frac{1}{\nu_0}\frac{\partial\nu}{\partial\tau}\bigg|_{\pi,0} = \frac{1}{\tilde{\theta}_c}\frac{3\nu_0 - 1}{3\tau_0\nu_0}\frac{1}{1 - \frac{1}{4}\frac{(3\nu_0-1)^2}{\tau_0\nu_0^3}} \tag{B.12}$$

using the expression

$$\frac{\partial\tau}{\partial\nu}\bigg|_{\pi,0} = \frac{3}{8}\left(\pi_0 + \frac{3}{\nu_0^2}\right)\left\{1 - \frac{2(3\nu_0 - 1)}{\nu_0^3(\pi_0 + 3/\nu_0^2)}\right\} = \frac{3\tau_0}{3\nu_0 - 1}\left(1 - \frac{1}{4}\frac{(3\nu_0 - 1)^2}{\nu_0^3\tau_0}\right). \tag{B.13}$$

The coefficient of thermal expansion is undefined at the critical point of thermodynamics, i.e. $\tau_0 = 1$, $\nu_0 = 1$, $\pi_0 = 1$, however, taking a look at the density vs. pressure diagram for a BZT fluid, PP10, say, cf. figure 1.1, the region of interest (region where Gamma changes sign) lies between $\nu_0 = 1.3$ and $\nu_0 = 2$, say. Evaluating the expression for β_0 for $\nu_0 = 1.3$ and τ_0 indicates that β_0 is finite and thus $\beta_0\theta_0 = \mathcal{O}(1)$ in the region of interest. Furthermore,

$$\frac{\tilde{K}_{s,0}}{\tilde{K}_{\theta,0}} = 1 - \frac{\tilde{\theta}_0\tilde{\beta}_0^2}{\tilde{\rho}_0\tilde{c}_{v,0}\tilde{K}_{\theta,0}}, \tag{B.14}$$

cf. [56], and

$$\tilde{K}_{\theta,0} = -\frac{1}{\tilde{p}_c}\frac{1}{\nu_0}\frac{\partial\nu}{\partial\pi}\bigg|_{\tau,0} = \frac{1}{\tilde{p}_c}\frac{1 - 3\nu_0}{3\left(1 + \frac{2-3\nu_0}{\nu_0^3\pi_0}\right)}. \tag{B.15}$$

As a consequence it is found

$$\frac{\tilde{K}_{s,0}}{\tilde{K}_{\theta,0}} = 1 + (\tilde{\beta}_0\tilde{\theta}_0)^2\frac{\tilde{p}_0}{\tilde{\rho}_0\tilde{\theta}_0\tilde{c}_{v,0}}\frac{3}{1 - 3\nu_0}\left(1 + \frac{2 - 3\nu_0}{\nu_0^3\pi_0}\right) = 1 + \mathcal{O}\left(\frac{\tilde{R}_g}{\tilde{c}_{v,0}}\right) = 1 + \mathcal{O}(\delta). \tag{B.16}$$

For the expression $\tilde{c}_0^2/(\tilde{R}_g\tilde{\theta}_0)$ one finds in the same manner

$$\frac{\tilde{c}_0^2}{\tilde{R}_g\tilde{\theta}_0} = 1 + \mathcal{O}(\delta). \tag{B.17}$$

Therefore, one concludes

$$G_0 = \mathcal{O}(\delta) \tag{B.18}$$

in the BZT region of a dense gas.

B.2   Utilized Relations

Expression $\frac{Dh}{Dt} = \frac{1}{Ec} \; c_p \frac{D\theta}{Dt} + \frac{1-\tilde{\beta}_0\tilde{\theta}_0\beta\theta}{\rho} \; \frac{Dp}{Dt}$.   Take $\tilde{h} = \tilde{h}(\tilde{\theta}, \tilde{p})$, then

$$\Delta\tilde{h} = \frac{\partial\tilde{h}}{\partial\tilde{\theta}}\Big|_{\tilde{p}} \Delta\tilde{\theta} + \frac{\partial\tilde{h}}{\partial\tilde{p}}\Big|_{\tilde{\theta}} \Delta\tilde{p}.$$

Definition (B.5) gives for the first coefficient

$$\tilde{c}_p = \frac{\partial\tilde{h}}{\partial\tilde{\theta}}\Big|_{\tilde{p}}.$$

For the second coefficient the free specific enthalpy $\tilde{g}$ is used

$$\tilde{g} = \tilde{h} - \tilde{\theta}\tilde{s}.$$

Then, using the following Maxwell relations

$$\frac{\partial\tilde{g}}{\partial\tilde{p}}\Big|_{\tilde{\theta}} = \frac{1}{\tilde{\rho}}, \quad \frac{\partial\tilde{s}}{\partial\tilde{p}}\Big|_{\tilde{\theta}} = -\frac{1}{\tilde{\rho}^2}\frac{\partial\tilde{\rho}}{\partial\tilde{\theta}}\Big|_{\tilde{p}}$$

and the definition of the coefficient of thermodynamic expansion (B.3)

$$\tilde{\beta} = -\frac{1}{\tilde{\rho}}\frac{\partial\tilde{\rho}}{\partial\tilde{\theta}}\Big|_{\tilde{p}} = -\tilde{\rho}\frac{\partial\tilde{s}}{\partial\tilde{p}}\Big|_{\tilde{\theta}}$$

finally leads to

$$\frac{\partial\tilde{h}}{\partial\tilde{p}}\Big|_{\tilde{\theta}} = \frac{1 - \tilde{\beta}\tilde{\theta}}{\tilde{\rho}}.$$

Introducing non-dimensional quantities yields the sought-after expression

$$\Delta h = \frac{1}{Ec}\, c_p \Delta\theta + \frac{1 - \tilde{\beta}_0 \tilde{\theta}_0 \beta\theta}{\rho}\, \Delta p. \tag{B.19}$$

Expression $\frac{\partial h}{\partial s}\big|_\rho = (1+G)\frac{\theta}{Ec}.$ Take $\tilde{h} = \tilde{h}(\tilde{s}, \tilde{p})$, then

$$\Delta\tilde{h} = \tilde{\theta}\Delta\tilde{s} + \frac{1}{\tilde{\rho}}\Delta\tilde{p}.$$

Then it follows

$$\frac{1}{Ec}\frac{\partial h}{\partial s}\bigg|_\rho = \frac{\partial \tilde{h}}{\partial \tilde{s}}\bigg|_{\tilde{\rho}} = \tilde{\theta} + \frac{1}{\tilde{\rho}}\frac{\partial \tilde{p}}{\partial \tilde{s}}\bigg|_{\tilde{\rho}}.$$

Making use of the Maxwell relation

$$\frac{\partial p}{\partial s}\bigg|_{\tilde{s}} = \tilde{\rho}^2 \frac{\partial \theta}{\partial \rho}\bigg|_{\partial s} = \tilde{\rho}\tilde{\theta}G,$$

considering the definition of the Grüneisen coefficient (B.9) in the last step, finally yields the sought-after relation

$$\frac{\partial h}{\partial s}\bigg|_\rho = (1+G)\frac{\theta}{Ec}. \tag{B.20}$$

Terms in the Taylor expansion of $h(1+\Delta\rho, s_0)$**.** Take $\tilde{h} = \tilde{h}(\tilde{s}, \tilde{p})$, then

$$\Delta\tilde{h} = \tilde{\theta}\Delta\tilde{s} + \frac{1}{\tilde{\rho}}\Delta\tilde{p}.$$

Take the definition of the fundamental derivative (1.1)

$$\Gamma = \frac{1}{\tilde{c}}\frac{\partial(\tilde{\rho}\tilde{c})}{\partial\tilde{\rho}}\bigg|_{\tilde{s}} = \frac{\tilde{\rho}}{\tilde{c}}\left(\frac{\tilde{c}}{\tilde{\rho}} + \frac{\partial\tilde{c}}{\partial\rho}\bigg|_{\tilde{s}}\right).$$

From that follows for the first term of the expansion

$$\frac{\partial\tilde{h}}{\partial\tilde{\rho}}\bigg|_{\tilde{s},0} = \frac{1}{\tilde{\rho}}\frac{\partial\tilde{p}}{\partial\rho}\bigg|_{\tilde{s},0} = \frac{\tilde{c}_0^2}{\tilde{\rho}_0},$$

using the definition of the speed of sound in the last step. The next term of
the Taylor expansion follows from

$$\left.\frac{\partial^2 \tilde{h}}{\partial \tilde{\rho}^2}\right|_{\tilde{s},0} = \left.\frac{\partial}{\partial \rho}\left(\frac{\tilde{c}^2}{\tilde{\rho}}\right)\right|_{\tilde{s},0} = -\frac{\tilde{c}_0^2}{\tilde{\rho}_0^2} + \left.2\frac{\tilde{c}_0}{\tilde{\rho}_0}\frac{\partial \tilde{c}}{\partial \tilde{\rho}}\right|_{\tilde{s},0} = \frac{\tilde{c}_0^2}{\tilde{\rho}_0^2}\left(2\Gamma_0 - 3\right).$$

The other expressions then follow in a likewise manner by differentiating the
expression of the previous term in the Taylor expansion and recursively using
the definition of the fundamental derivative of gas dynamics Γ and its first
and second derivative, Λ, N. As an illustration the next higher derivative of
$\tilde{h}$ is given below.

$$\begin{aligned}
\left.\frac{\partial^3 \tilde{h}}{\partial \tilde{\rho}^3}\right|_{\tilde{s},0} &= \left.\frac{\partial}{\partial \tilde{\rho}}\left(\frac{\tilde{c}^2}{\tilde{\rho}^2}\left(2\Gamma - 3\right)\right)\right|_{\tilde{s},0} = \\
&= -2\frac{\tilde{c}_0^2}{\tilde{\rho}_0^3}(2\Gamma_0 - 3) + \left.2(2\Gamma_0 - 3)\frac{\tilde{c}_0}{\tilde{\rho}_0^2}\frac{\partial \tilde{c}}{\partial \tilde{\rho}}\right|_{\tilde{s},0} + \left.2\frac{\tilde{c}^2}{\tilde{\rho}^2}\frac{\partial \Gamma}{\partial \tilde{\rho}}\right|_{\tilde{s},0} = \\
&= \frac{\tilde{c}_0^2}{\tilde{\rho}_0^2}\left(4\Gamma_0^2 - 14\Gamma_0 + 12 + 2\Lambda_0\right).
\end{aligned}$$

Appendix C

Asymptotic Properties of the Airy Function

The asymptotic representation of the Airy function $\mathrm{Ai}(z)$ with $z \in \mathbb{C}$ for $|z| \gg 1$ has been given in [1] by

$$\mathrm{Ai}(z) \sim \tfrac{1}{2}\pi^{-1/2}z^{-1/4}e^{-\zeta}\sum_0^{\infty}(-1)^k c_k \zeta^{-k} \qquad |\arg(z)| < \pi$$

with $\zeta = \frac{2}{3}z^{3/2}$. The coefficients c_k are defined as

$$c_0 = 1, \quad c_k = \frac{(2k+1)(2k+3)\dots(6k-1)}{216^k k!}.$$

Introducing

$$z = Re^{\mathrm{i}\phi}, \qquad \zeta = \tfrac{2}{3}R^{3/2}e^{\mathrm{i}\frac{3}{2}\phi}, \qquad R > 0$$

the asymptotic formula can be written as

$$\mathrm{Ai}(R,\phi) \sim \tfrac{1}{2}\pi^{-1/2}R^{-1/4}e^{-\mathrm{i}\phi/4}e^{-\frac{2}{3}R^{3/2}(\cos(\frac{3}{2}\phi)+\mathrm{i}\sin(\frac{3}{2}\phi))}.$$

$$\cdot \sum_0^{\infty}(-1)^k c_k (\tfrac{2}{3}R)^{-\frac{3}{2}k}e^{-\mathrm{i}\frac{3}{2}k\phi} \qquad |\phi| < \pi.$$

The sum is converging absolutely according to the comparison test for series, cf. e.g. [20],

$$\left| (-1)^k c_k (\tfrac{2}{3} R)^{-\frac{3}{2}k} e^{-i\frac{3}{2}k\phi} \right| \leq |c_k| R^{-\frac{3}{2}k} \left| e^{-i\frac{3}{2}k\phi} \right| < |c_k| R^{-k} \qquad R \geq 1$$

with $|c_k| R^{-k} < |c_0| R^{-k} = R^{-k}$. The dominated convergence follows from the convergence of the geometric series, cf. [20],

$$\sum_0^\infty \left(\frac{1}{R} \right)^k = \frac{1}{1 - \frac{1}{R}}$$

for $R \geq 1$. From that follows

$$|\mathrm{Ai}(z)| \sim R^{-1/4} \left| e^{-i\phi/4} e^{-\frac{2}{3} R^{3/2} (\cos(\frac{3}{2}\phi) + i\sin(\frac{3}{2}\phi))} \right| \sim$$

$$\sim R^{-1/4} \left| e^{-\frac{2}{3} R^{3/2} \cos(\frac{3}{2}\phi)} \right|.$$

Hence, the Airy function is unbounded for $|z| \to \infty$ if $\cos(\frac{3}{2}\phi) < 0$ and $\mathrm{Ai}(z) \to 0$ if $\cos(\frac{3}{2}\phi) > 0$, i.e. $\arg(z) \in [-\pi/3, \pi/3]$.

Appendix D

Calculation of the Eigenvalue Spectrum for the Trivial State

The generalized eigenvalue problem, cf. equation (4.25), for the trivial steady state $(\bar{U}_0, P_0)^T = \mathbf{0}$ is given by

$$\mu P_{10} = \text{sign}(K)\frac{\partial P_{10}}{\partial X} - Q \lim_{Y \to \infty} \frac{\partial \bar{U}_{10}}{\partial X}, \tag{D.1}$$

$$0 = \frac{\mathrm{d}P_{10}}{\mathrm{d}X} + Y\frac{\partial \bar{U}_{10}}{\partial X} - \int_0^Y \frac{\partial \bar{U}_{10}}{\partial X}\mathrm{d}\bar{Y} - \frac{\partial^2 \bar{U}_{10}}{\partial Y^2} \tag{D.2}$$

using $\mathbf{y} = (\bar{U}_{10}, P_{10})^T$ in ansatz (4.24). The linearized boundary conditions are

$$\lim_{X \to \pm\infty} P_{10} = 0, \qquad \lim_{X \to \pm\infty} \bar{U}_{10} = 0, \tag{D.3}$$

$$\bar{U}_{10}(X, Y = 0) = \frac{\partial \bar{U}_{10}}{\partial X}(X, Y = 0) = 0. \tag{D.4}$$

Introducing the Fourier Transform, cf. e.g. [51] or [21], of $P_{10}(X)$ and $\bar{U}_{10}(X, Y)$

$$P_{10}^{\wedge}(\omega) = \frac{1}{2\pi} \int_{-\infty}^{\infty} P_{10}(X)\mathrm{e}^{-\mathrm{i}\omega X}\mathrm{d}X, \tag{D.5}$$

$$\bar{U}_{10}^{\wedge}(\omega, Y) = \frac{1}{2\pi} \int_{-\infty}^{\infty} \bar{U}_{10}(X, Y)\mathrm{e}^{-\mathrm{i}\omega X}\mathrm{d}X \tag{D.6}$$

equations (D.1) and (D.2) are transformed to Fourier space

$$\mu P_{10}^{\wedge} = i\omega \text{sign}(K) P_{10}^{\wedge} - i\omega Q \lim_{Y \to \infty} \bar{U}_{10}^{\wedge}, \tag{D.7}$$

$$0 = i\omega P_{10}^{\wedge} + i\omega Y \bar{U}_{10}^{\wedge} - i\omega \int_0^Y \bar{U}_{10}^{\wedge} d\bar{Y} - \frac{\partial^2 \bar{U}_{10}^{\wedge}}{\partial Y^2}. \tag{D.8}$$

The pressure in equation (D.8) can be eliminated by differentiating the equation with respect to Y leading to

$$i\omega Y \frac{\partial \bar{U}_{10}^{\wedge}}{\partial Y} = \frac{\partial^3 \bar{U}_{10}^{\wedge}}{\partial Y^3} \tag{D.9}$$

which can be transformed into Airy's differential equation, cf. [1],

$$Z \, g(Z, \omega) = \frac{\partial^2}{\partial Z^2} g(Z, \omega) \tag{D.10}$$

using the transformations

$$Z = (i\omega)^{1/3} Y, \qquad g(Z, \omega) = \frac{\partial}{\partial Y} \bar{U}_{10}^{\wedge}(Y, \omega). \tag{D.11}$$

The solution to (D.10) is

$$g(Z, \omega) = \frac{\partial}{\partial Y} \bar{U}_{10}^{\wedge}(Y, \omega) = a(\omega) \text{Ai}\left((i\omega)^{1/3} Y\right) \tag{D.12}$$

where $a(\omega)$ is a yet undefined integration "constant" depending on ω since ω is entering equation (D.10) as a parameter only. Ai is the first Airy function, cf. [1], the other linear independent solution of Airy's differential equation, i.e. the second Airy function Bi, cf. [1], is unbounded for $Y \to \infty$. Furthermore, $(i\omega)^{1/3} Y \in \{Z \in \mathbb{C} : |\text{Arg}(Z)| \leq \pi/3\}$, cf. appendix C. From that follows

$$\lim_{Y \to \infty} \bar{U}_{10}^{\wedge} = \lim_{Y \to \infty} \int_0^Y a(\omega) \text{Ai}\left((i\omega)^{1/3} \bar{Y}\right) d\bar{Y} =$$
$$= \frac{a(\omega)}{(i\omega)^{1/3}} \lim_{Y \to \infty} \int_0^{(i\omega)^{1/3} Y} \text{Ai}(Z) dZ = \frac{1}{3} \frac{a(\omega)}{(i\omega)^{1/3}} \tag{D.13}$$

exploiting the properties of the Airy function in the evaluation of the integral, cf. [1]. Evaluating equation (D.8) for $Y = 0$ gives a relation for $P_{10}^{\wedge}(\omega)$, i.e.

$$P_{10}^{\wedge} = a(\omega)(\mathrm{i}\omega)^{-2/3}\mathrm{Ai}'(0). \tag{D.14}$$

Note $\mathrm{Ai}'(0) < 0$, cf. [1]. Inserting (D.13) and (D.14) into (D.7) finally gives the relation for the spectrum of eigenvalues $\mu(\omega)$

$$\mu(\omega) = \frac{Q}{3\mathrm{Ai}'(0)} \sin(\tfrac{\pi}{6})|\omega|^{4/3} + \mathrm{i}\omega \left(\mathrm{sign}(K) - \frac{Q}{3\mathrm{Ai}'(0)} \cos(\tfrac{\pi}{6})|\omega|^{1/3} \right). \tag{D.15}$$

In the calculations

$$(\mathrm{i}\omega)^{1/3} = \begin{cases} |\omega|^{1/3}\mathrm{e}^{\mathrm{i}\frac{\pi}{6}} & \omega > 0 \\ |\omega|^{1/3}\mathrm{e}^{-\mathrm{i}\frac{\pi}{6}} & \omega < 0 \end{cases} \tag{D.16}$$

has been used which follows form the requirement $(\mathrm{i}\omega)^{1/3}Y \in \{Z \in \mathbb{C} : |\mathrm{Arg}(Z)| \leq \pi/3\}$.

Bibliography

[1] M. Abramowitz and I.E. Stegun, editors. *Handbook of mathematical functions: with formulas, graphs, and mathematical tables*. Dover Publ., 1970.

[2] D. A . Anderson, J. C. Tannehill, and R. H. Pletcher. *Computational fluid mechanics and heat transfer*. Series in computational and physical processes in mechanics and thermal sciences. Taylor & Francis, 2 edition, 1997.

[3] V. Balakotaiah, S. Dommeti, and G. Nikunj. Bifurcation analysis of chemical reactors and reacting flows. *Chaos*, 9(1):13–35, 1999.

[4] H.A. Bethe. The theory of shock waves for an arbitrary equation of state. *Office Sci. Res. & Dev. Rep.*, 545(545), 1942.

[5] A. A. Borisov, Al. A. Borisov, S. S. Kutateladze, and V. E. Nakoryakov. Rarefaction shock wave near the critical liquid-vapour point. *J. Fluid Mech.*, 126:59–73, 1983.

[6] E.O. Brigham. *FFT, Schnelle Fourier-Transformation*. R. Oldenbourg, 1987.

[7] P. J. K. Bruce and H. Babinsky. Unsteady shock wave dynamics. *J. Fluid Mech.*, 603:463–473, 2008.

[8] D. Chandrasekar and P. Prasad. Transonic flow of a fluid with positive and negative nonlinearity through a nozzle. *Phys. Fluids A*, 3((3)):427–438, 1991.

[9] T. Chung, M. Ajlan, L.L. Lee, and K.E. Starling. Generalized multi-parameter correlation for nonpolar and polar fluid transport properties. *Ind. Eng. Chem. Res.*, 27:671–678, 1988.

[10] P. Cinnella and P. M. Congedo. Inviscid and viscous aerodynamics of dense gases. *J. Fluid Mech.*, 580:179–217, 2007.

[11] P. Colonna and A. Guardone. Molecular intepretation of nonclassical gas dynamics of dense vapors under the van der Waals model. *Phys. Fluids*, 18(056101), 2006.

[12] P. Colonna, A. Guardone, and N.R. Nannan. Siloxanes: A new class of candidate Bethe-Zel'dovich-Thompson fluids. *Phys. Fluids*, 19(086102), 2007.

[13] P. Colonna and P. Silva. Dense gas thermodynamic properties of single and multicomponent fluids for fluid dynamics simulations. *J. Fluids Eng.*, 125:414–427, 2003.

[14] M. Cramer and A. Kluwick. On the propagation of waves exhibiting both positive and negative nonlinearity. *J. Fluid Mech.*, 142:9–37, 1984.

[15] M. S. Cramer and R. Sen. Exact solutions for sonic shocks in van der waals gases. *Phys. Fluids*, 30(2):377–385, 1986.

[16] M.S. Cramer. Negative nonlinearity in selected fluorocarbons. *Phys. Fluids A*, 1(11):1894–1897, 1989.

[17] M.S. Cramer. Nonclassical dynamics of classical gases. In A. Kluwick, editor, *Nonlinear Waves in Real Fluids*, CISM Courses and Lectures No. 315, pages 91–145. Springer, New York, 1991.

[18] M.S. Cramer and A.B. Crickenberger. The dissipative structure of shock waves in dense gases. *J. Fluid Mech.*, 223:325–355, 1991.

[19] S.H. Fergason, T.L. Ho, B.M. Argrow, and G. Emanuel. Theory for producing a single-phase shock wave. *J. Fluid Mech.*, 445:37–54, 2001.

[20] H. Fischer and H. Kaul. *Mathematik für Physiker 1*. Teubner Studien-bücher, 1997.

[21] H. Fischer and H. Kaul. *Mathematik für Physiker 2*. Teubner Studien-bücher, 1998.

[22] A.C. Fowler. *Mathematical Models in the Applied Sciences*. Cambridge University Press, 1997.

[23] Ph. Gittler. On similarity solutions occurring in the theory of interactive laminar boundary layers. *J. Fluid Mech.*, 244:131–147, 1992.

[24] C. Grinschgl. *Einschichtenströmung über ein Hindernis*. PhD thesis, TU Vienna, 2005.

[25] A. Guardone and B.M. Argrow. Nonclassical gasdynamic region of selected fluorocarbons. *Phys. Fluids*, 17(116102):1–17, 2005.

[26] E. Guyon, J. Hulin, and L. Petit. *Hydrodynamik*. Vieweg, 1997.

[27] T. Handa and M. Masuda. Mechanism of shock wave oscillation in transonic diffusers. *AAIA Journal*, 41(1):64–70, 2003.

[28] P.-F. Hao, Y.-T. Ding, Z.-H. Yao, and H. Feng. Size effect on gas flow in micro nozzles. *J. Micromech. Microeng.*, 15:2069–2073, 2005.

[29] L. Hogben, editor. *Handbook of linear algebra*, volume 39 of *Discrete Mathematics and Its Applications*. Chapmann & Hall/CRC, 2006.

[30] M.H. Holmes. *Introduction to Perturbation Methods*. Springer, 1998.

[31] M. E. Hosea and L. F. Shampine. Analysis and implementation of TR-BDF2. *Applied Numerical Mathematics*, 20:21–37, 1996.

[32] J. C. Williams III. Viscous compressible and incompressible flow in slender channels. *AAIA Journal*, 1(1):186–195, 1963.

[33] H. Oertel jr., editor. *Prandtl - Führer durch die Strömungslehre: Grundlagen und Phänomene*. Vieweg+Teubner, 11. edition, 2002.

[34] A. Kluwick. Small-amplitude finite-rate waves in fluids having both positve and negative nonlinearity. In A. Kluwick, editor, *Recent advances in boundary layer theory. CISM Courses and Lectures No. 315.* SpringerWienNewYork, 1991.

[35] A. Kluwick. Transonic nozzle flow of dense gases. *J. Fluid Mech.*, 247:661–688, 1993.

[36] A. Kluwick. Interacting laminar boundary layers of dense gases. *Acta Mechanica*, [Suppl] 4:335–349, 1994.

[37] A. Kluwick. Interacting laminar and turbulent boundary layers. In A. Kluwick, editor, *Recent advances in boundary layer theory. CISM Courses and Lectures No. 390.* SpringerWienNewYork, 1998.

[38] A. Kluwick. Marginally separated flows in dilute and dense gases. *Phil. Trans. R. Soc. London. A*, 358:3169–3192, 2000.

[39] A. Kluwick. Internal flows of dense gases. *Acta Mechanica*, 196:123–143, 2004.

[40] A. Kluwick and R. J. Bodonyi. Freely interacting boundary layers in channels. In *Proceedings of the annual GAMM meeting, ZAMM*, volume 58, pages T283–T284, 1979.

[41] A. Kluwick, S. Braun, and P. Gittler. Transonic, laminar high Reynolds number flow in slender channels. In H. Sobiezky, editor, *IUTAM Symposium Transonicum IV: proceedings of the IUTAM symposium held in Göttingen, Germany, 2-6 September*, 2002.

[42] A. Kluwick, A. Exner, and E. A. Cox. On the interal structure of weakly nonlinear bores in laminar high Reynolds number flow. *Acta Mechanica*, 2008 (submitted).

[43] A. Kluwick and P. Gittler. Transonic laminar interacting boundary layers in slender channels. In *Proceedings of the annual GAMM meeting, ZAMM*, volume 81, pages S473–S474, 2001.

[44] A. Kluwick and S. Scheichl. Unsteady transonic nozzle flow of dense gases. *J. Fluid Mech.*, 310:113–137, 1996.

[45] A. Kluwick, S. Scheichl, and E. A. Cox. Near-critical hydraulic flows in two-layer fluids. *J. Fluid Mech.*, 575:187–219, 2007.

[46] L. D. Landau and E. M. Lifshitz. *Fluid Mechanics*, volume 6 of *Course of Theoretical Physics*. Butterworth-Heinemann, 2 edition, 2002.

[47] W. Langbein. *Thermodynamik: Grundlagen und Anwendungen.* Verlag Harri Deutsch, 1999.

[48] R. J. LeVeque. A study of numerical methods for hyperbolic conservation laws with stiff source terms. *J. Comput. Phys.*, 86:187–210, 1988.

[49] R.J. LeVeque. *Numerical methods for conservation laws.* Birkhäuser, 1999.

[50] R.J. LeVeque. *Finite volume methods for hyperbolic problems.* Cambridge University Press, 2002.

[51] M. J. Lighthill. *An introduction to Fourier analysis and generalised functions.* Cambridge University Press, 2003.

[52] M.J. Lighthill. On boundary layers and upstream influence II. Supersonic flows without separation. *Proc. Roy. Soc. A*, 217:478 – 504, 1953.

[53] J.J. Martin and Y. Hou. Development of an equation of state for gases. *A.I.Ch.E. Journal*, 1(2):142–151, 1955.

[54] K. Matsuo, Y. Miyazato, and H. Kim. Shock train and pseudo-shock phenomena in internal gas flows. *Progress in Aerospace Sciences*, 35(1):33–100, 1999.

[55] G. E. A. Meier. Shock induced flow oscillations in a Laval nozzle. In K. Oswatitsch, editor, *Symposium Transonicum II*, pages 252–261. Springer Verlag, 1976.

[56] M. Menikoff and B.J. Plohr. The riemann problem for fluid flow of real materials. *Reviews of Modern Physics*, 61(1):75–130, 1989.

[57] A. F. Messiter. Boundary layer flow near the trailing edge of a flat plate. *SIAM J. Appl. Math.*, 18:241–257, 1970.

[58] J. F. Monaco, M. S. Cramer, and L. T. Watson. Supersonic flows of dense gases in cascade configuration. *J. Fluid Mech.*, 330:31–59, 1997.

[59] V. Ya. Neiland. Towards a theory of separation of the laminar boundary layer in a supersonic stream. *Izv. Akad. Nauk SSSR, Mekh. Zhidk. Gaza*, 4:53–57, 1969.

[60] F. Obermeier. An analytical description of unsteady transonic Laval-nozzle flow. *Z. Flugwiss. Weltraumforsch.*, 12:253–257, 1988.

[61] O. A. Oleinik. Discontinuous solutions of non-linear differential equations. *Am. Math. Soc. Translations*, 26:95–172, 1957.

[62] K. Oswatitsch. *Gasdynamik*. Wien: Springer, 1952.

[63] M. Powell. *Numerical methods for nonlinear algebraic equations*, chapter 7. London [u.a.]: Gordon and Breach, 1970.

[64] L. Prandtl. Zur Berechnung der Grenzschichten. *Z. angew. Math. Mech.*, 18:77–82, 1938.

[65] W. J. Rae. Some numerical results on viscous low-density nozzle flows in the slender-channel approximation. *AAIA Journal*, 9(5):811–820, 1971.

[66] M. Rein, G. Grabitz, and G. E. A. Meier. Strömungsschwingungen in Lavaldüsen. *Z. Flugwiss. Weltraumforsch.*, 10(1):1–5, 1986.

[67] T.A. Reyhner and I. Flügge-Lotz. Interaction of a shock wave with a laminar boundary layer. *Int. J. Nonlinear Mech.*, 3:173–199, 1968.

[68] O. Schenk and K. Gärtner. Solving unsymmertic sparse sytems of linear equations with PARDISO. *J. of Future Generation Computer Sytems*, 20(3):475–487, 2004.

[69] O. Schenk and K. Gärtner. On fast factorization pivoting methods for symmertic indefinite sytems. *Elec. Trans. Numer. Anal.*, 23:158–179, 2006.

[70] O. Schenk, K. Gärtner, and W. Fichtner. Efficient sparse LU factorisation with left-right looking strategy on shared multiprocessors. *BIT*, 40(1):158–176, 2000.

[71] W. E. Schiesser. *The numerical method of lines.* Academic Press, 1991.

[72] H. Schlichting and K. Gersten. *Grenzschicht-Theorie.* Springer, 1997.

[73] W. Schneider. Upstream propagation of unsteady disturbances in supersonic boundary layers. *J. Fluid Mech.*, 63(3):205–234, 1974.

[74] W. Schneider. *Mathematische Methoden in der Strömungslehre.* Vieweg, 1978.

[75] W. Schneider and S. Haas. *Repititorium Thermodynamik.* Oldenbourg, 2004.

[76] R. Seydel and V. Hlavacek. Role of continuation in engineering analysis. *Chemical Engineering Science*, 42(6):1281–1295, 1987.

[77] F. T. Smith. Pipeflows distorted by non-symmetric indentation or branching. *Mathematika*, 23:62–83, 1976.

[78] K. Stewartson. *The Theory of Laminar Boundary Layers in Compressible Fluids.* Oxford University Press, 1964.

[79] K. Stewartson. On the flow near the trailing edge of a flat plate ii. *Mathematika*, 16:106–121, 1969.

[80] K. Stewartson. Multistructured boundary layers on flat plates and related bodies. *Adv. Appl. Mech.*, 14:145–239, 1974.

[81] K. Stewartson and P. G. Williams. Self-induced separation. *Proc. Roy. Soc. A*, 312:181–206, 1969.

[82] J. Stoer and R. Bulirsch. *Numerische Mathematik 2.* Berlin [u.a.]: Springer, 5 edition, 2005.

[83] S. Subramanian and V. Balakotaiah. Mode interactions in reactor-driven convection in a porous medium. *Chemical Engineering Science*, 12:1851–1866, 1995.

[84] R. Szeywerth and A. Kluwick. On a new numerical algorith for the solution of triple deck problems. In *PAMM Proc. Appl. Meath. Mech.*, volume 7, 2007.

[85] P. A. Thompson. A fundamental derivative in gasdynamics. *Phys. Fluids*, 14:1843–1849, 1971.

[86] P. A. Thompson. *Compressible-fluid dynamics.* New York: McGraw-Hill, 1972.

[87] P. A. Thompson, H. Chaves, G. E. A. Meier, Y. Kim, and H.-D. Speckmann. Wave splitting in a fluid of large heat capacity. *J. Fluid Mech.*, 185:385–414, 1987.

[88] P. A. Thompson and K. C. Lambrakis. Negative shock waves. *J. Fluid Mech.*, 60(1):187–208, 1973.

[89] H. Troger and A. Steindl. *Nonlinear stability and bifurcation theory.* Wien New York: Springer, 1991.

[90] E. Truckenbrodt. *Fluidmechanik 2.* Berlin [u.a.]: Springer, 1998.

[91] M. VanDyke. *Perturbation Methods in Fluid Mechanics.* Parabolic Press, 1975.

[92] T. G. Wright and L. N. Trefethen. Large-scale computation of pseudospectra using ARPACK and eigs. *SIAM J. Sci. Comput.*, 23(2):591–605, 2001.

[93] Q. Xiao and H. M. Tsai. Numerical investigation of supersonic nozzle flow separation. *AAIA Journal*, 45(3):532–541, 2007.

[94] J. Xu and C. Zhao. Two-dimensional numerical simulations of shock waves in micro convergent-divergent nozzles. *Int. J. Heat and Mass Trans.*, 50:2434–2438, 2007.

[95] C. Zamfirescu, A. Guardone, and P. Colonna. Admissibility region for rarefaction shock waves in dense gases. *J. Fluid Mech.*, 599:363–381, 2008.

[96] Y. B. Zel'dovich. On the possibility of rarefaction shock waves. *Zh. Eksp. Teor. Fiz.*, 4:363–364, 1946.

[97] F. Zieher. Laminare Grenzschichten in schweren Gasen. Master's thesis, Institute of Fluid Mechanics and Heat Transfer, Vienna University of Technology, 1993.

Curriculum Vitae

Dipl.–Ing. Georg Meyer
Lacknergasse 106/05, A–1180, Vienna
07–23–1978, born in Vienna
Austrian citizenship
Henriette & Franz, parents, Vera, sister

Studies and Education

2005–2009	Ph.D-studies at *Vienna University of Technology* advisor: Prof. A. Kluwick, co-advisor (WK): Prof. Ch. Schmeiser
05/2005	master's degree (Dipl.-Ing.); thesis: 'Simulation der Strömung in einem Kolbenverdichter', advisor: Prof. H. Steinrück funded by the *European Forum for Reciprocating Compressors*
2004–2005	civilian service at the *Grünes Kreuz*, Vienna
1996–2005	studies of Chemical Engineering at the *Vienna Univ. of Techn.*
1988–1996	grammar school at the BG XVIII, Klostergasse 25, Vienna
1984–1988	elementary school at the *Albertus Magnus-Schule*, Vienna XVIII

Employments and Internships

2005–2008	research assistent (FWF) at the *Institute of Fluid Mechanics and Heat Transfer, Vienna Univ. of Techn.* & student-member at the doctoral college *WK Differential Equations*, speaker: Prof. Ch. Schmeiser
2003	internship (2 months) at the *arsenal research*, business area *Verkehrstechnologie*, CFD simulation
2002	internship (1 1/2 months) at the *arsenal research*, business area *Verkehrstechnologie*, CFD simulation

List of Publications

G. Meyer and A. Kluwick. Shockregularisation in dense gases by viscous invsicid regularisation. talk at *XXII International Congress of Theoretical and Applied Mechanics (ICTAM 2008)*, Adelaide, SA, Australia, 08-24-2008 - 08-29-2008. in *XXII International Congress of Theoretical and Applied Mechanics - CD-ROM Proceedings*, Jim Denier, M. Finn, T. Mattner (ed.), (2008), ISBN: 978-0-9805142-1-6.

A. Kluwick and G. Meyer. Transonic Viscous Inviscid Interactions of Dense Gases in Narrow Channels. talk at *8th World Congress on Computational Mechanics (WCCM8) and 5th European Congress on Computational Methods in Applied Sciences and Engineering (ECCOMAS 2008)*, Venice, Italy, 06-30-2008 - 07-04-2008. in *WCCM8 ECCOMAS 2008 - CD-ROM Proceedings*, B. Schrefler, U. Perego (ed.), CIMNE, (2008).

G. Meyer and A. Kluwick. Transonic Viscous Inviscid Interactions in Narrow Channels. talk at *GAMM Annual Meeting 2007 / 6th International Congress on Industrial and Applied Mathematics*, Zürich, Switzerland, 07-16-2007 - 07-20-2007. in *Proceedings in Applied Mathematics and Mechanics PAMM 2007*, (2007).

R. Aigner, G. Meyer and H. Steinrück. Valve Dynamics and Internal Waves in a Reciprocating Compressor. talk at *EFRC Conference*, Antwerp, Belgium, 06-09-2005 - 06-10-2005. in *4th EFRC Conference*, (2005), 169 - 178.